

Self-organized growth of ordered functional nanostructures on templates

THÈSE No 3428 (2005)

présentée à la Faculté Sciences de Base

Institut de Physique des Nanostructures

Section de Physique

ÉCOLE POLYTECHNIQUE FÉDÉRALE DE LAUSANNE

pour l'obtention du grade de Docteur ès sciences

par

THOMAS R. CLASSEN

Diplom-Physiker, Universität Stuttgart, Allemagne

et de nationalité allemande

acceptée sur proposition du jury:

Prof. K. Kern, directeur de thèse

Dr. R. Fasel, rapporteur

Prof. K. Morgenstern, rapporteur

Prof. D. Pavuna, rapporteur

Lausanne, EPFL

2005

Abstract

In this thesis, the use of nanotemplates for steering the molecular self-organization at metallic surfaces is investigated. Nanotemplates are surfaces that exhibit a periodic variation of the adhesion energy on the nanometer scale. Preferential adsorption on low energy sites is utilized to effectively transfer the template structure to the overlayer of the deposited adsorbates.

Surfaces with an anisotropic lattice geometry and self-organized alternating oxide and metallic stripes are exemplarily investigated as model for one-dimensional nanotemplates of different periodicities. Their effects on the adsorption of deposited organic molecules and on the formation of extended supramolecular architectures are studied by scanning tunneling microscopy (STM) and complementary experimental and theoretical techniques.

The first part of the thesis deals with the growth of metal-organic coordination networks (MOCNs), a concept which has recently been transferred from 3D supramolecular chemistry to 2D surface grids. It is shown here for the first time, that it is possible to create surface supported 1D metal-organic coordination chains (MOCCs) using the Cu(110) surface as a nanotemplate, along with the same methods which are used to create 2D MOCNs. 1,3,5-benzenetricarboxylic acid (trimesic acid, TMA) is employed as organic linker molecule forming monodisperse and highly regular chains with Cu adatoms. The atomistic structure of the MOCCs is investigated in a combined experimental and theoretical approach, using STM, low energy electron diffraction (LEED), reflection-absorption infrared spectroscopy (RAIRS) and density functional theory (DFT). A detailed understanding of the MOCCs is reached and the possibility to generalize these results to other metal-carboxylate systems is explored by studying a different linker molecule, 1,4-benzenedicarboxylic acid (terephthalic acid, TPA).

MOCCs are potentially relevant for catalytic or magnetic applications as they offer lowly coordinated but thermodynamically stable 1D arrangements of metallic centers.

Functional MOCCs are created on Cu(110) by co-deposition of TMA molecules and Fe atoms. These structures are thoroughly analyzed by STM and rationalized by means of DFT calculations. A net spin-moment is predicted for the Fe centers inside the chain which is comparable to that of free Fe adatoms on the surface.

The adhesion of a dipeptide, Phe-Phe, on Cu(110) is investigated in order to further analyze the templating role of this substrate for the structure formation of larger organic molecules. Phe-Phe forms homochiral chains showing that the molecular chirality is effectively transferred to the supramolecular level. The comparison with the Phe-Phe-chains obtained on the chemically similar but structurally different Cu(100) substrate, demonstrates that commensurability to the surface lattice is one of the most important parameters governing the supramolecular growth modes.

Furthermore, the possibilities to create mixed two-dimensional surface crystals using two different molecular adsorbates is investigated. The metal-organic chain structures based on TMA are combined with the chiral Phe-Phe molecules. A single mixed-phase with a hierarchical substructure is obtained, which unites the properties of the individual structures, namely metal-organic coordination and enantiopure chirality. This result represents a further step towards transferring the supramolecular design concepts known in 3D supramolecular chemistry to surfaces.

Finally, the Cu(110)-(2×1)O-striped phase is used as a tunable, self-organized template for the molecular structures reported above. MOCCs are created in the bare Cu surface areas that define the length and position of the chains. The ordering is limited, though, by interactions of the MOCCs with the Cu-O stripes which are traced back to a competition for Cu adatoms necessary for the formation of both structures. No such concurrence exists for Phe-Phe which is correspondingly found to be efficiently contained to the bare Cu areas and well ordered by the Cu-O-stripes even for the second layer of Phe-Phe. These results are discussed in comparison to literature data and with respect to a wider use of this nanotemplate for the adsorption of larger organic molecules.

Zusammenfassung

Im Rahmen dieser Doktorarbeit wird die Verwendung von Nanotemplaten zur Steuerung der molekularen Selbstorganisation auf metallischen Oberflächen untersucht. Nanotemplate sind Oberflächen, die auf der Nanometerskala eine periodische Variation der Adhäsionsenergie aufweisen. Durch die bevorzugte Adsorption auf Positionen niedriger Energie wird die Templatstruktur auf die Überstruktur deponierter Adsorbate übertragen.

Oberflächen mit einer anisotropen Gittergeometrie und mit selbstorganisierten, sich abwechselnden Metall- und Oxidstreifen werden als Modelle für eindimensionale Nanotemplate unterschiedlicher Periodizität verwendet. Ihr Einfluss auf die Adsorption deponierter organischer Moleküle und auf die Bildung ausgedehnter supramolekularer Architekturen wird mittels Rastertunnelmikroskopie (STM) und komplementären experimentellen und theoretischen Techniken untersucht.

Der erste Teil der Arbeit beschäftigt sich mit dem Wachstum metall-organischer Koordinationsnetzwerke (MOCNs), einem Konzept, das vor kurzem aus der dreidimensionalen supramolekularen Chemie auf zweidimensionale Oberflächen übertragen wurde. Es wird hier erstmals gezeigt, dass es möglich ist, oberflächenbasierte eindimensionale metall-organische Koordinationsketten (MOCCs) unter Verwendung der Cu(110) Oberfläche als Nanotemplat herzustellen kombiniert mit denselben Methoden, die benutzt werden, um zweidimensionale MOCNs zu erzeugen. 1,3,5-Benzentricarboxylsäure (Trimésinsäure, TMA) dient als organisches Bindemolekül, das monodisperse und sehr gleichmässige Ketten mit Cu Adatomen erzeugt. Die atomistische Struktur der MOCCs wird in einem kombinierten Ansatz aus experimentellen und theoretischen Methoden untersucht: mittels STM, der Beugung niederenergetischer Elektronen (LEED), Reflektions-Absorptions-Infrarot-Spektroskopie (RAIRS) und Dichtefunktionaltheorie (DFT). Hierdurch wird ein detailliertes Verständnis der MOCCs erzielt. Die Möglichkeit, diese Ergebnisse auf andere metall-organische Systeme zu verallgemeinern, wird am Beispiel eines anderen Bindemoleküls, 1,4-Benzendicarboxylsäure (Terephthalsäure, TPA) erforscht.

MOCCs können zukünftig für katalytische oder magnetische Anwendungen relevant sein, da sie niedrig koordinierte, aber thermodynamisch stabile eindimensionale Anordnungen von metallischen Zentren darstellen. Funktionelle MOCCs werden auf Cu(110) mittels einer Kodeposition von TMA Molekülen und Fe Atomen erzeugt. Ihre Struktur wird eingehend mittels STM analysiert und durch DFT Rechnungen nachvollzogen. Für die Fe Zentren innerhalb der Ketten wird ein effektives Spin-Moment vorhergesagt, das vergleichbar zu dem eines freien Eisenatoms auf der Oberfläche ist.

Die Adhäsion eines Dipeptids, Phe-Phe, auf Cu(110) wird untersucht, um die Templat-Funktion dieses Substrats für die Strukturbildung größerer organischer Moleküle zu analysieren. Phe-Phe bildet homochirale Ketten, die zeigen, dass die Chiralität des Moleküls effektiv auf das supramolekulare Niveau übertragen wird. Der Vergleich mit Phe-Phe-Ketten, die auf dem chemisch ähnlichen aber strukturell verschiedenen Cu(100) Substrat nachgewiesen wurden, zeigt, dass Kommensurabilität zum Oberflächengitter einer der wichtigsten Parameter für das supramolekulare Wachstum ist.

Es wird ferner untersucht, ob es möglich ist, gemischte zweidimensionale Oberflächenkristalle unter Verwendung zweier verschiedener molekularer Adsorbate zu erzeugen. Die auf TMA basierenden metall-organischen Kettenstrukturen werden mit den chiralen Phe-Phe Molekülen kombiniert. Es ergibt sich eine einzelne gemischte Phase mit einer hierarchischen Substruktur, die die Eigenschaften der individuellen Strukturen, insbesondere metall-organische Koordination und die Existenz nur eines Enantiomers verbindet. Dieses Ergebnis stellt einen weiteren Schritt dar auf dem Weg, die aus der dreidimensionalen supramolekularen Chemie bekannten Designkonzepte auf Oberflächen zu übertragen.

Schließlich wird die Cu(110)-(2×1)O-Streifenphase als variables selbstorganisiertes Templat für die oben genannten Strukturen verwendet. MOCCs werden auf den freien Kupfer-Bereichen der Oberfläche erzeugt, wodurch die Länge und Position der Ketten vorgegeben wird. Das Ordnungsverhalten wird jedoch durch Wechselwirkungen der MOCCs mit den Cu-O-Streifen begrenzt, was auf eine Konkurrenz um die Cu-Adatome, die zur Bildung beider Strukturen notwendig sind, zurückgeführt werden kann. Für Phe-Phe existiert keine solche Konkurrenzsituation, es zeigt sich dementsprechend, dass das Wachstum von Phe-Phe durch die Cu-O-Streifen bestimmt und auf die freien Kupferbereiche begrenzt wird, bis hin zur zweiten Lage von Phe-Phe. Die Resultate werden diskutiert und mit Literaturergebnissen verglichen, insbesondere im Hinblick auf eine breitere Verwendung dieses Nanotemplats für die Adsorption größerer organischer Moleküle.

Für meine Eltern und für Mirjam

Contents

Abstract	i
Zusammenfassung	iii
1 Introduction	1
2 Analysis of organic molecules on surfaces	5
2.1 STM	5
2.1.1 The theory of STM	5
2.1.2 Scanning tunneling spectroscopy	9
2.2 Complementary techniques	10
2.2.1 RAIRS	11
2.2.2 LEED	12
2.2.3 DFT	13
2.3 Organic molecules	15
2.3.1 Evaporation	15
2.3.2 Bonding types	15
2.3.3 Chirality	16
2.4 Experimental setup	16
2.4.1 The STM system	16
2.4.2 STS	19
2.4.3 Sample preparation	21
3 Design of an integrated e-beam sample holder	23
3.1 The technical problem	23
3.2 Design of a new sample holder	25
3.3 Performance	27

4	Intrinsic metal-organic structures	29
4.1	Introduction: Metal-organic coordination networks	29
4.1.1	MOCN in 3D	29
4.1.2	Surface based MOCNs	31
4.1.3	Carboxylate formation on surfaces	32
4.2	Templated growth of MOC chains	33
4.2.1	TMA deposition at 130 K	36
4.2.2	IR measurements at low temperatures	37
4.2.3	TMA deposition at 240 K	40
4.2.4	Chain formation at room temperature and above	43
4.2.5	Chain length	47
4.3	MOCC-S: Analysis of the Cu-TMA-Cu-chains	51
4.3.1	STM and LEED analysis	51
4.3.2	Theory	57
4.3.3	Analysis of the electronic structure	60
4.3.4	Final discussion and summary of the MOCC-S structure	64
4.4	MOCC-D: Cu-TMA-Double chains	65
4.4.1	The structure of MOCC-D	65
4.4.2	The transition regime	67
4.4.3	IR measurements	68
4.4.4	About packing and energetics	70
4.5	TPA on Cu(110)	72
4.6	Comparison and Discussion	75
5	Extrinsic metal-organic structures	77
5.1	Introduction	77
5.2	Fe-TMA-chains	78
5.2.1	Chain growth and structure	78
5.2.2	DFT-results	81
5.2.3	Magnetic properties	83
5.3	Comparison and Discussion	84
6	Chiral structuring	87
6.1	Chiral chains of Phe-Phe	87

6.1.1	Introduction	87
6.1.2	L-Phe-L-Phe and D-Phe-D-Phe on Cu(110)	89
6.1.3	L-Phe-L-Phe and D-Phe-D-Phe on Cu(100)	91
6.1.4	Chain length	92
6.1.5	Comparison and Discussion	93
6.2	Chiral supramolecular MOCNs	97
6.2.1	The concept	97
6.2.2	Structure creation and characterization	98
7	The Cu-O stripes: a self-organized nanotemplate	103
7.1	Structure of the Cu-Oxygen stripes	103
7.1.1	Introduction	103
7.1.2	The striped phase	104
7.2	The Cu-O stripes as nanotemplate	108
7.2.1	TMA on the Cu-O striped phase	108
7.2.2	Phe-Phe on the Cu-O striped phase	111
7.2.3	Discussion of the templation efficiency	113
8	Conclusions and Perspectives	115
	Abbreviations and Common Symbols	121
	List of Figures	123
	List of Tables	124
	Literature	125
	Publications	137
	Acknowledgements	139
	Curriculum vitae	141

Chapter 1

Introduction

The creation of continuously smaller structures is a well-known trend in microelectronics and data storage techniques today [1,2]. However, this race for further miniaturization has so far been run on the safe ground of a classical – if not to say a macroscopic – world. The major part of the steady reduction of feature sizes, though technically extremely demanding, is still a projection of macroscopic concepts onto smaller length scales. This “top-down” strategy has so far successfully disregarded what Uzi Landman has very effectively condensed into the slogan “small is different” [3]. The quantum-mechanical and quantum-chemical nature of matter is still often viewed in the classical limit of averaged material properties and continuum mechanics [1]. The onset of quantum effects at small length scales is thus frequently described in a quite pessimistic way as a set of obstacles to the established production techniques [4].

On the contrary, the central goal of nanotechnology is precisely the exploitation of these particular properties of matter that emerge on the nanometer length scale. Analyzing and understanding the processes happening at this length scale is the first step to create new structures. Ultimately, this knowledge might be helpful also for a further miniaturization of existing devices. Nevertheless, the greater expectation concerns the creation of completely new concepts which actively use the specific properties of nanometer sized objects to produce novel types of applications [5].

Top-down strategies can in principle still be used also on a nanometer scale. Electron beams are able to create structures of feature sizes of tens of nanometers [6] and individual atoms or molecules can be actively positioned using scanning probe techniques [7]. On the other hand, both methods are serial processes and thus intrinsically slow in creating extended structures. Parallel lithography techniques might become available in the

future [8] but can be expected to be very cost intensive [9].

The so-called “bottom-up” approach addresses the question from the opposite direction. Structures are created on a surface through self-organization intrinsically using the specific interaction of individual building blocks such as atoms or molecules with each other and with the surface [9, 10]. Self-organized growth is an efficient parallel technique as it happens individually at the same time on countless equivalent positions of a given substrate. The resulting overall structure depends on the interaction of the individual building blocks, and a careful design of those building blocks opens a rich field of achievable structures. Especially, when using molecules as elementary units, the bonding preferences as well as the interaction with the substrate can be tuned using the full variety of techniques available from state of the art synthetic chemistry. Moreover, non-covalent bonding can be employed as intermolecular interaction thus allowing the growth of structures close to thermodynamic equilibrium where efficient self-correction mechanisms occur [9, 11]. Using different bonding mechanisms a hierarchical structuring can be achieved, too [12].

With bottom up approaches, molecular nanostructures can be grown that are fundamentally different from what can be achieved by top-down methods. One recent example are metal-organic coordination networks (MOCNs) which originate in crystal engineering of 3D supramolecular structures by means of self-organization [13, 14]. Lately, this concept has been successfully transferred to surfaces where 2D MOCNs have been fabricated which constitute grids of metallic centers regularly spaced by organic linker molecules using coordination bonding [15]. When using magnetic atoms as metal centers such structures might have a strong potential for data storage as so called magnetic printboards [2, 16–18].

In molecular self-organization, the systematic adjustment of the resulting structure is not as direct as in top-down approaches as structure is only implicitly incorporated and not actively imposed [9]. The molecular design offers tuning parameters to change and optimize structures by adjusting the relative strength and the type of intermolecular interactions [19]. Nevertheless, the obtained patterns are often hard to foresee and structures are usually explained a-posteri upon the basis of the observed results rather than designed a-priori. This is mainly due to the delicate interplay of competing interactions, particularly between intermolecular interactions and the coupling of the molecules to the substrate. In order to be able to steer the self-organized growth, additional “tuning knobs” are necessary. Furthermore, even if the intermolecular interactions are ideally

adjusted, the stochastic nature of the growth process can induce randomness or local disorder to the final structure. Finally, it would be advantageous to structurally organize the molecules by other means than tuning intermolecular interactions as this would leave more freedom to adjust their functional groups for special optic, catalytic or even biologic functionality.

One possibility to direct the self-organized growth at surfaces is the use of nanotemplates. These are substrates which exhibit a periodical variation of the adhesion energy for an adsorbing species. Nanotemplates of periodicities of some tens of nanometers or higher can be created using top-down methods such e-beam writing [6, 20, 21]. On a true atomic scale other types of nanotemplates have to be used. In this thesis we will focus on nanotemplates for which the patterning arises either from self-organization of an adsorbate on a surface or from the intrinsic atomistic structure of the substrate itself. Such templates can in principle be combined with top-down templation methods, e. g. in order to create self-organized molecular structures inside of electronic circuits of a larger length-scale.

One example for a templating substrate are surfaces with an intrinsically anisotropic surface lattice, such as the (110) surface of fcc metals which can be used to create 1D structures of atoms [22–26] or molecules [27–29]. A surface reconstruction can lead to a surface pattern of increased periodicity [30–34] where the reconstruction can either be present before or can occur upon overlayer adsorption. A particularly well-known example of a reconstructed surface is the Au(111) surface showing the so-called herringbone reconstruction [35] which has been used also as a template in several cases [36–39]. Next, the use of vicinal surfaces has allowed to create 1D atomic structures due to the preferential attachment at step edges [40–44]. The combination of the two latter approaches in form of the Au(788) surface created a 2D template of 0D adhesion positions [45–47]. Another class of nanotemplates are 2D (bi-)metallic layers which due to lattice mismatch with the substrate create island patterns of finite size [48–50]. Finally, also non-metallic adsorbates can act as templates [51]. Particularly, the adsorption of oxygen on Cu(110) and of nitrogen on Cu(100) leads to the formation of long range ordered 1D and 2D patterns [52–56]. For the case of oxygen on Cu(110), the periodicity of the 1D Cu-O structure can be tuned over a wide range by varying the oxygen coverage [52].

In this work we investigate the possibility to structure the adsorption of molecular nanostructures on metallic surfaces using self-organized and atomistic nanotemplates.

We furthermore analyze the interaction of the molecular building blocks with each other and with the nanotemplate. Scanning tunneling microscopy (STM) in ultra-high vacuum is used as the main technique throughout the study, but complementary techniques are employed as well to achieve a more comprehensive picture.

The thesis is organized as follows: First, a short introduction to the employed techniques, the underlying theory, and the experimental setup is given in chapter 2 and the construction of new special sample holder for the STM setup is discussed in chapter 3.

In chapter 4, Cu(110) is used as an anisotropic surface to template the growth of metal-organic coordination networks. We show that it is possible to grow 1D metal-organic coordination chains with Cu centers by this method. These chains are investigated exemplarily in great detail using complementary experimental and theoretical techniques to understand the interaction mechanism that allows the effective templation. In chapter 5 we extend this method to create also extrinsic metal-organic chains, i. e. chains in which the intrinsically available Cu centers are exchanged for Fe. Possible implications of this structure for the study of low dimensional magnetic effects are discussed.

In order to investigate the behavior of larger organic molecules at surfaces, we analyze the chain growth of Phe-Phe, a dipeptide, on the Cu(110) surface in chapter 6. The results are compared to others obtained on the higher symmetric Cu(100) surface to understand the effects of an anisotropic surface on the molecular chain formation. Furthermore, we analyze the potential to create 2D surface crystals of higher complexity by combining the properties of a metal-organic coordination network with a chiral peptide system.

Finally, in chapter 7 we focus on the Cu-O system. The possibilities to use this surface as a nanotemplate of tunable periodicity are discussed. Exemplarily, the adhesion of a molecular (Phe-Phe) and a metal-organic coordination system on this nanotemplate are investigated. For the metal-organic system chains of finite length are obtained. Nevertheless the templation is limited by an interaction of the Cu-O stripes with the chains. For Phe-Phe on the other hand a very efficient templation is reached even up to the second layer of Phe-Phe.

Chapter 2

Analysis of organic molecules on surfaces

Most results within this work have been obtained using scanning tunneling microscopy (STM). We will present here a short introduction to the theory of STM. The further complementary techniques that have been used in this thesis will also be briefly described here. We will then focus on specific properties of organic molecules which are relevant for structure formation at surfaces. Finally, we give an overview of the employed STM setup.

2.1 STM

2.1.1 The theory of STM

The working principle of the STM [57] is to bring a sharp metallic tip into close vicinity of a flat conducting sample surface (between 5 Å and 10 Å). This distance is small enough to allow quantum mechanical tunneling upon applying a bias voltage between the tip and the sample. For a generic particle of energy E and a mass m the tunneling probability P through a potential barrier of height V_B and width z is given by

$$P(z) \propto e^{-2\kappa z}, \text{ with} \quad (2.1)$$

$$\kappa^2 = 2m(V_B - E)/\hbar^2. \quad (2.2)$$

Equation (2.1) shows that the tunneling probability depends exponentially on the distance z . In the STM, tunneling thus occurs mainly from the apex of the tip, which in

the ideal case is atomically sharp, to the surface area directly below the tip apex. This gives rise to a very high vertical and lateral resolution. As the tunneling electrons carry a charge e , the overall tunneling current I in first rough approximation is proportional to P and it is thus possible to replace P by I in (2.1) [58]. A typical operation mode when moving the tip across the surface is to keep the tunneling current I constant (constant current mode). When encountering a protrusion or a depression, the tip has to be moved from or to the surface. This is typically achieved by piezos having an almost linear voltage extension characteristic. The deviation of I from a setpoint value is used to regulate the extension of the piezos in a feedback loop and the recorded voltages applied to the z -piezo are normally used as a representation of the surface topography (constant-current image). Nevertheless, already the most fundamental theoretical description of STM tunneling, the theory of Tersoff and Hamann [59], shows that the tunneling current not only depends on the tip-sample distance and that constant-current images are thus only an approximation to the real surface topography.

According to Tersoff and Hamann, the elastic tunneling current can be written in first order perturbation theory using Fermi's Golden Rule [58, 59]:

$$I(V) = \frac{2\pi e}{\hbar} \sum_{s,t} (f(E_s) [1 - f(E_t)] - f(E_t) [1 - f(E_s)]) \cdot |M_{st}|^2 \cdot \delta(E_t + V - E_s) , \quad (2.3)$$

where $f(E)$ is the Fermi distribution, V is the applied voltage, $|M_{st}|^2$ is the tunneling matrix element between the states ψ_s of the surface and ψ_t of the tip, and $E_{s,t}$ are the energies of these states. This expression can be simplified by assuming a step-like behavior for the Fermi function, which in principle is true only at zero temperature and is a rough approximation at 300 K, but provides reasonable insight in most cases. Then

$$I(V) = \frac{2\pi e^2 V}{\hbar} \sum_{s,t} |M_{st}|^2 \cdot \delta(E_s - E_F) \cdot (E_t - E_F) , \quad (2.4)$$

where we have introduced the Fermi energy E_F . According to Bardeen [60], the tunneling matrix elements are then given by

$$M_{st} = \frac{\hbar^2}{2m} \int d\mathbf{S} \cdot (\psi_s^* \nabla \psi_t - \psi_t \nabla \psi_s^*) , \quad (2.5)$$

where the integral is over the whole surface \mathbf{S} . In order to evaluate M_{st} , Tersoff-Hamann formulate an ansatz for the wavefunctions ψ_s and ψ_t with the approximation of an s -orbital like electronic configuration of the tip [59]. The summation over the absolute squares of the wavefunctions together with energy δ functions in (2.4) can be evaluated

to yield the local density of states (LDOS) of the sample ρ_s at the position (x, y) below the tip and the LDOS ρ_t of the tip. This allows to write (2.4) as

$$I(V) \propto \int_0^{eV} \rho_s(E, x, y) \cdot \rho_t(E - eV) \cdot \mathcal{T}(E, V, z) dE, \quad (2.6)$$

where the Fermi level is at $E_F = 0$ V and \mathcal{T} is the transition matrix describing the tunneling probability. Equation (2.6) shows that the tunneling depends on the density of states of the tip at the applied bias voltage V , on the density of states of the surface at the Fermi-level, and on the transition matrix \mathcal{T} . According to (2.1), \mathcal{T} can be written in the following form [61],

$$\mathcal{T}(E, V, z) = e^{\left(-2z\sqrt{(m_e/\hbar^2) \cdot (W_s + W_t - 2E + eV)}\right)}, \quad (2.7)$$

where $W_{s,t}$ are the work functions of the sample and tip. For deriving this expression it has been assumed, that the tunneling is purely vertical. As a further approximation, all surface state contributions other than of s or p_z symmetry have been disregarded (only surface states of quantum number $m = 0$ have been used). A further simplification to (2.7) is to neglect the contribution of the term $(-2E + eV)$ in comparison to the work functions which allows to take \mathcal{T} in front of the integral in (2.6).

$$I(V) \propto e^{-2\kappa \cdot z} \int_0^{eV} \rho_s(E, x, y) \cdot \rho_t(E - eV) dE, \quad (2.8)$$

where $\kappa = \sqrt{(m_e/\hbar^2) \cdot (W_s + W_t)}$ depends now only on the work functions $W_{t,s}$ of the tip and the surface. Equation (2.8) is the final result of the approach. The first factor of (2.8) describes the exponential z -dependence of the tunneling current, which is commonly called “topography” information, while the integral factor depends on the density of states of the tip and the sample.

Several implications for the interpretation of STM images can be seen from (2.8). From the integral factor of (2.8) it is clear, that the STM does not show a real geometrical surface contour as it reflects electronic configurations rather than the positions of nuclei. Instead of measuring “heights” with the STM it is thus more appropriate to speak of “apparent heights” which are influenced by the LDOS. It is important to realize that the STM does neither map contours of constant electron density (as would be given e. g. by orbital plots). As elastic tunneling only occurs for electrons at energies between E_F and $E_F + eV$, where V is the applied bias voltage, only the LDOS in this energy

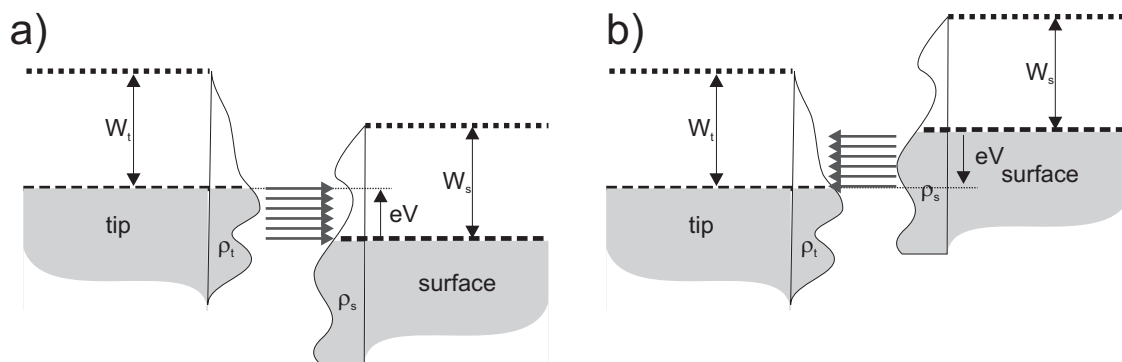


Figure 2.1: Energy level diagram of tip and sample for a) positive surface to tip bias voltage (tunneling from tip into unoccupied sample states) and b) negative bias voltage (tunneling from occupied sample states into tip).

window contributes to the I signal. This can be seen from the integration limits of (2.8) and is also graphically shown in Figure 2.1. The observed STM images are therefore also not plots of constant LDOS, instead they are plots of constant LDOS windows at the Fermi level. The LDOS (and therefore also such LDOS windows) can be computed using e. g. density functional theory which will be introduced in section 2.2.3. In principle this provides means to simulate STM images on the basis of a structural model. It should be noted, though, that the current or height signal of the STM is not dependent on the LDOS of the sample alone, as even in this crude approximation it also depends also on the LDOS of the tip, see (2.8). In total, the theory of Tersoff and Hamann already shows that STM images do not necessarily represent topographs of the surface atomistic structure but are influenced by different electronic contributions.

Further deviations between STM images and the surface topography arise from those contributions which have been neglected in the Tersoff-Hamann theory. As stated above, tunneling was assumed to occur only vertically from s into s or p_z states. The effect of tip states having different angular components ($m \neq 0$) can change the apparent heights and can even create an inversion in which positions in between of surface atoms are imaged higher than the positions of the surface atoms themselves [62–64].

The investigation of adsorbates on surfaces is even more complex and introduces further difficulties in comparison to measuring pristine surfaces [58]. Especially organic molecules typically only have a very small number of states at the Fermi level as this falls into their usually broad gap between the highest occupied and the lowest unoccupied molecular orbital (HOMO-LUMO). Non-resonant tunneling or inelastic tunneling can

thus form a significant contribution to the current in these systems [65]. As the overall molecular tunneling contributions can be low, they can even be of comparable size to the direct tunneling to the surface although the surface is further away from the tip than the molecule. Tunneling can thus happen either via tip-molecule-surface or directly from tip to surface, which creates two competing current channels. The interaction of these channels can create interference effects which can completely change the observed apparent heights [66].

Although these limits have to be kept in mind when analyzing STM data, the STM is in general able to provide fast and in-depth information on the structure of adsorbates on surfaces. All measurements in this work have been taken in constant current mode, if not stated otherwise. Typical scanning conditions have been $U = -1$ V and $I = 1$ nA, which corresponds to tunneling from surface to tip, so-called “filled state imaging”. In this configuration the role of tip and sample in (2.8) is seemingly exchanged (see Figure 2.1b). Under these conditions we have made good experiences in obtaining significant molecular tunneling contributions which create realistic apparent height values.

2.1.2 Scanning tunneling spectroscopy

Scanning tunneling spectroscopy (STS) is used in order to directly evaluate the electronic information which is present in the integral in (2.8). The scanning is stopped, the feedback loop is opened, which for a stable STM results in a constant z (in practice this is only true for a certain time that depends on the stability of the experimental setup). While ramping the bias voltage, the current I and the differential conductance dI/dV are recorded. The differential conductance can be calculated by taking the derivative of (2.8):

$$\frac{dI}{dV} \propto \left(\left[- \int_0^{eV} \rho_s(E) \frac{d\rho_t}{dE}(E - eV) dE \right] + \rho_s(eV) \rho_t(0) \right) . \quad (2.9)$$

It is typically assumed that the tip-DOS does not depend on the voltage. Then, the integral term in (2.9) vanishes, and the differential conductance becomes

$$\frac{dI}{dV} \propto \rho_s(eV) \cdot \rho_t(0) . \quad (2.10)$$

(2.10) describes the ideal case for STS, probing the surface LDOS by rapidly ramping V without other influences.

Practically, the situation is more complex. It is often observed that the dI/dV signal does depend on the electronic configuration of the tip in a much stronger way than indicated by (2.10)¹. As a rule of thumb, above the Fermi level often sharper unoccupied states exist whereas the occupied states below E_F are often more broadened and featureless [67]. As a result, STS is in general more reliable, when tunneling from broad, voltage independent (flat) occupied tip states to the sharp unoccupied sample states than vice versa, as this situation is closer to what was assumed above in deriving (2.10). Following the used conventions, this corresponds to STS spectra at positive voltages. In general, a flat tip LDOS cannot be guaranteed when taking ST spectra of adsorbates on surfaces. On the other hand, it is possible to take spectra both on clean surface areas and on the adsorbate. According to [67–69] the difference of both spectra provides a reasonable approximation to the real LDOS of an adsorbate as the contribution of the tip states is similar in both cases.

Finally, it should be noted, that the resolution of STS is limited by temperature broadening. For non-zero temperatures (2.9) will include broadening factors arising from the Fermi-Dirac distribution which was approximated by step functions in (2.4). The linewidth of STS spectra is given by the convolution of the broadening both of tip and of sample states and is thus larger than the broadening of the individual states.

2.2 Complementary techniques

STM is a local technique with high lateral resolution but with limited chemical sensitivity. Complementary information has thus to be gained from chemically more sensitive techniques. We present here a short introduction to reflection absorption infrared spectroscopy (RAIRS). All RAIRS measurements were performed in group of Sam Haq and Rasmita Raval at the Surface Science Center of the University of Liverpool, UK. The RAIRS setup also contained a low energy electron diffraction (LEED) system. LEED will also be introduced here as it provides a fast overview over structural periodicities, which allowed to connect the RAIRS measurements to the STM data acquired in our setup. We furthermore give here an overview over density functional theory (DFT) as many of the results in this thesis are based on a comparison between STM measurements and DFT calculations.

¹Different electronic configurations of the tip, which can but must not originate from different morphologies, are often referred to as “different tips”, although the same physical tip is used.

2.2.1 RAIRS

The study of molecules has always been closely linked to optical spectroscopy techniques. Visible and UV light are used for electronic transitions, microwaves for rotations, and infrared light (IR) for molecular vibrations. The resonant absorption of IR is caused by the interaction of an electromagnetic wave with a dynamic molecular dipole formed by a vibration of at least two neighboring atoms. The vibration frequency is characteristic for the specific bond as the vibrational energy levels depend on the masses of the involved atoms and on the bond strength (“spring constant”) [70, 71].

Reflection absorption infrared spectroscopy (RAIRS) shines IR light at grazing incidence onto a sample. The reflected light is recorded by a spectrometer outside the UHV chamber using IR transmitting windows. The signal for a surface with a molecular adsorbate is analyzed relative to a background signal obtained on the pristine surface.

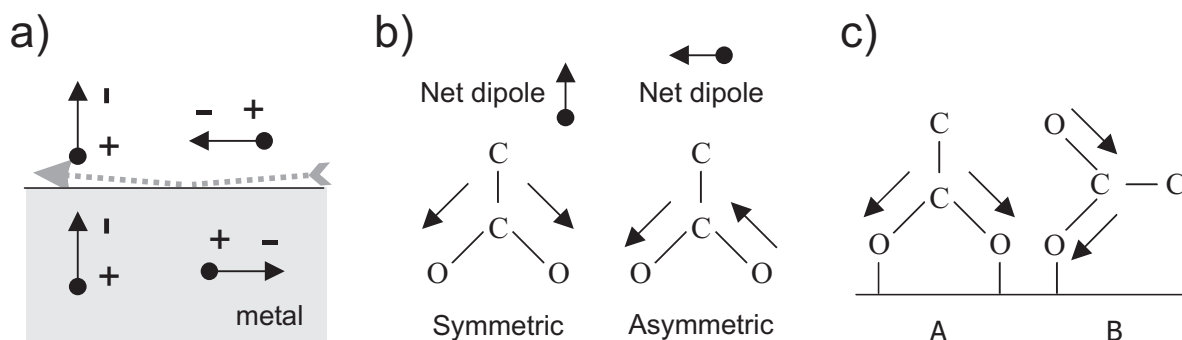


Figure 2.2: RAIRS at surfaces: a) dipoles and mirror dipoles; b) dipole moments of the symmetric and asymmetric vibration of the carboxylate group; c) vibration modes detectable with RAIRS [72].

Electric dipoles as generated by vibrating molecules in front of a metallic surface induce mirror dipoles (see Figure 2.2a). For dipoles oriented parallel to the surface, real and mirror dipole cancel each other, while for dipoles oriented perpendicular to the surface an increased overall dipole-moment exists. RAIRS can only detect vibrations of modes for which the dynamical dipole moment is oriented perpendicular to the surface. As an example, Figure 2.2b shows the asymmetric and symmetric stretch modes of the carboxylate group (see also section 4.1.3). As can be seen from Figure 2.2c, the symmetric mode can only be detected if the molecular group is oriented vertical on the surface. In an inclined orientation the signal strength will be reduced, for flat orientation no absorption will be detected. The asymmetric stretch, on the other hand, is only observed for a flat

orientation of the group, as only in this case a vertical dipole moment exists. RAIRS can thus provide double information: it shows which functional groups exist on the surface (if they are detectable). And in the ideal case it allows to deduce the orientation of the molecule from a combined analysis of the observed oscillation modes.

2.2.2 LEED

The de Broglie wavelength λ of electrons of energy E is given by

$$\lambda = \frac{h}{\sqrt{2m_e \cdot E}} . \quad (2.11)$$

Using electrons with energies between 10 eV and 100 eV this wavelength can be tuned between ≈ 0.4 nm and 0.1 nm. Electrons in this energy window interact strongly with the solid state lattice and have a mean free path of only 0.5-1 nm in the solid. When incident onto a surface, most of the electronic wave is thus scattered by the top 3-4 surface layers. Out of these, low energy electron diffraction (LEED) analyzes the elastically diffracted electrons [73]. They carry the reciprocal space information of the surface lattice and of overlayer structures, such as a molecular adlayer. The backscattered electrons are focussed by means of electrostatic optics onto a fluorescent screen where they show spots representing the 2D reciprocal lattice of the surface structure. From measuring the unit-cell vectors of the surface, one can reconstruct the real-space lattice. When analyzing an overlayer structure, the most straightforward way is to measure the extra spots of the overlayer vectors \mathbf{a}_O^* , \mathbf{b}_O^* with respect to the spots of the substrate lattice \mathbf{a}_S^* , \mathbf{b}_S^* of the reciprocal lattice. Using a matrix notation

$$\begin{pmatrix} \mathbf{a}_O^* \\ \mathbf{b}_O^* \end{pmatrix} = \mathbf{M}^* \cdot \begin{pmatrix} \mathbf{a}_S^* \\ \mathbf{b}_S^* \end{pmatrix} , \text{ with } \mathbf{M}^* = \begin{pmatrix} m_{11}^* & m_{12}^* \\ m_{21}^* & m_{22}^* \end{pmatrix} . \quad (2.12)$$

The real matrix \mathbf{M} is then the inverse transpose of \mathbf{M}^* [73]. This allows to construct the overlayer lattice vectors in real space \mathbf{a}_O , \mathbf{b}_O in terms of the real space substrate lattice vectors \mathbf{a}_S , \mathbf{b}_S [74, 75]

$$\begin{pmatrix} \mathbf{a}_O \\ \mathbf{b}_O \end{pmatrix} = \mathbf{M} \cdot \begin{pmatrix} \mathbf{a}_S \\ \mathbf{b}_S \end{pmatrix} . \quad (2.13)$$

Integer components of \mathbf{M} signify commensurate overlayers. For an orthogonal overlayer lattice which is parallel to the substrate lattice the off-diagonal entries of \mathbf{M} vanish and the compact $(m_{11} \times m_{22})$ notation can be used for describing the primitive unit cell. The case of a centered unit cell can also be described by a similar short notation as $c(n \times m)$.

2.2.3 DFT

Density functional theory (DFT) is a parameter-free theoretical method which is built only on physical laws and thus is “ab-initio”. Using DFT, it is possible to calculate the electronic structure of a set of atoms (typically less than about 100) with high precision. Periodic boundary conditions are mostly employed when used for a surface where the periodicity in z -direction is maintained by treating the surface as a slab with vacuum on-top and by periodically repeating both slab and vacuum in a supercell. All DFT calculations which will be shown in this work have been performed by Guido Fratesi and Stefano Fabris, Stefano de Gironcoli and Stefano Baroni at the SISSA and Democritos, Trieste, Italy.

DFT is based on the Born-Oppenheimer approximation which exploits the fact that electrons move much faster than atomic cores. A full calculation can thus be split into two nested calculation loops. In the inner one, DFT determines the electronic distribution for a given set of atomic nuclei positions, while in the outer loop this electronic distribution is used to calculate the forces between the atoms [76, 77]. The so-called relaxation of the atomic positions is then a step-wise movement of the nuclei according to these forces until the forces become smaller than a predefined value. Due to the loop nesting, each relaxation step includes a full inner loop of self-consistent calculation. The final configuration is then the energetically optimal configuration both for nuclei and electrons.

It is clear that important input parameters of DFT are the number and the type of the atoms of a structure as well as the periodicity of the structure as this is needed to build the initial supercell. A possibly crude model of the atomic position is also extremely helpful as input. Such a model can be build using the results of STM, LEED or similar structure-resolving experimental techniques.

DFT is a single particle theory which solves the Schrödinger equation for one electron in the electric field of all nuclei and all other electrons. The Kohn-Sham equations [78] state that all these interactions can be described by an effective potential v_{eff} that is formed by the external Coulomb potential of the nuclei v_{ext} (which, in the inner loop, is fixed), by the Coulomb potential of all electrons (Hartree-Potential) $v_H(n)$, and by an electronic exchange correlation term $v_{\text{xs}}[n]$. Both $v_H(n)$ and $v_{\text{xs}}[n]$ depend at each spacial position \mathbf{r} only on the electron density n :

$$v_{\text{eff}}(\mathbf{r}) = v_{\text{ext}}(\mathbf{r}) + v_H(n, \mathbf{r}) + v_{\text{xs}}[n](\mathbf{r}) . \quad (2.14)$$

v_{eff} is used in the Schrödinger equation for the electron wave function ψ_i and energy ϵ_i :

$$\left(-\frac{\hbar^2}{2m}\nabla^2 + v_{\text{eff}}(\mathbf{r})\right)\psi_i(\mathbf{r}) = \epsilon_i\psi_i(\mathbf{r}) . \quad (2.15)$$

Finally, to close the circle, the electron density n is nothing else than the probability distribution to find an electron at a position \mathbf{r} and thus the sum of the absolute squares of all wavefunctions ψ at this position

$$n(\mathbf{r}) = \sum_{i=1}^{n_e} |\psi(\mathbf{r})|^2 . \quad (2.16)$$

Let us assume to start with a certain initial test electron distribution n . This is inserted in (2.14) which produces v_{eff} . With this v_{eff} the Schrödinger equation (2.15) is solved. This provides the energy and the wavefunctions, which in (2.14) create a new n . The process is repeated until convergence, i. e. until the energy values obtained at the iteration $i + 1$ differ from those of iteration i by less than a pre-defined small value. The theorems of Hohenberg and Kohn [79] state that: 1) the lowest possible energy, i. e. the ground state energy, is attained as limit for infinitesimal convergence and that 2) the corresponding electron density is the real ground state electron density n_{gr} . Using n_{gr} all relevant physical quantities can be calculated, in particular the Hellmann-Feynman forces which are necessary to relax the nuclei positions in the outer calculation loop [76, 77]. The ground state energy can in general be used to compare the stabilities of different configurations of nuclei and electrons.

The strongest limitations of DFT are within the calculation of the exchange correlation term $v_{\text{xs}}[n]$ for which only approximate solutions exist. Today, the local density approximation (LDA) and the generalized gradient approximation (GGA) are the most commonly used ones. While LDA tends to slightly overestimate bond strengths and underestimates bond lengths, GGA produces errors of opposite sign (mostly smaller, though). Typical errors in GGA when calculating bond lengths are on the order of a few percent. It should furthermore be noticed, that DFT is a ground state calculation, which in principle is only valid at zero temperature. While increasing the temperature normally does not significantly alter the nuclei positions, excited electron states which are empty at 0 K are typically not well treated by DFT [80].

2.3 Organic molecules

2.3.1 Evaporation

The standard way to deposit substances onto a surface in UHV is by sublimation. In the case of organic molecules this is normally done by uniformly heating them in a crucible of inert material such as glass or aluminium oxide. In order to obtain reproducible molecular fluxes and a collimated beam, a closed volume with a small hole, as is provided by a Knudsen cell for organic molecular beam epitaxy (OMBE), is typically used. Heating is necessary as for many organic molecules the vapor pressure is small at room temperature. Heating, on the other hand, can also break internal bonds of the molecules [81]. Evaporation has thus to be carried out at low deposition rates (1 monolayer (ML) per several minutes) in order to keep the evaporation temperature low. Alternative techniques for transferring molecules into the gas phase have thus to be employed for the deposition of large and fragile molecules (e. g. biomolecules) in UHV. Electrospray ionization (ESI) deposition is such a method which has just recently been developed in our group [82,83].

2.3.2 Bonding types

For organic molecules different types of bonding are found such as covalent bonding, ionic bonding, van-der-Waals bonding, hydrogen bonding, and coordination bonding. Their variety is larger than in inorganic compounds. Hydrogen bonding can exist for example between an oxygen atom of a carboxylate group (COO^-) and a hydrogen of a phenyl-group (H-C) [84,85] and π - π -interactions, as known for graphite, are also found between parallel phenyl-rings of organic molecules. Coordination bonding is of particular relevance for the investigated structures. Its strength is of an intermediate level between e. g. hydrogen and covalent bonding. It arises from the partial transfer of electron density from an electron pair donor (Lewis base) to an electron pair acceptor (Lewis acid) [86]. Coordination bonding thus can be formed between atoms, molecules, or molecular groups which already formally exhibit a filled electronic shell configuration but which can further lower their groundstate energy by slightly increasing or decreasing their electronic filling level when transferring charge to a matching partner. In this sense, coordination bonding always changes the electronic filling level of its constituents. Typical Lewis bases are organic molecules with a lone pair of electrons as e. g. the amino group. Typical Lewis acids are carboxylic groups, protons or metal cations (e. g. Cu^{2+}) [86].

2.3.3 Chirality

If a molecular structure and its mirror image cannot be superimposed to each other by any means of rotations and translations, the structure is called chiral and the two mirror symmetric forms are referred to as enantiomers [75]. For organic molecules chirality can for example arise at a carbon atom which is bonded to four different residues (tetrahedral carbon, “chiral center”) as rotations only allow a cyclic change of the residues but not a direct exchange of two of them. The absolute chirality is defined either by using the Cahn-Ingberg-Prelog rules [87] (S, R) or, as will be done in the following, by using the older Fischer system [88] (D, L).

A surface breaks the space symmetry. A molecule deposited on a surface has less degrees of freedom as it typically cannot flip upside-down. Chirality can thus be introduced by surface adsorption and molecules that are achiral (non-chiral) in 3D but chiral in 2D are called prochiral. These molecules create surface patterns of both mirror symmetric forms in a (1:1) racemic mixture when deposited onto an achiral surface since they statistically fall into either form. Also completely achiral molecules can create chiral structures on the surface through a chiral supramolecular organization. Of course also here, a (1:1) racemic mixture exists across the surface [75].

2.4 Experimental setup

2.4.1 The STM system

Although the STM system had been planned before [82] it was firstly set in operation in the course of this work. We will thus describe here also some important parameters as well as known limitations of the system. The setup consists of two chambers, the preparation chamber for sample cleaning and deposition and the analysis chamber comprising the STM. A photography of the whole system is shown in Figure 2.3.

The preparation chamber is equipped with the following standard components: firstly, an ion gun which is used for sputter cleaning of the sample substrates. For the Cu(110) surface we typically have applied a high voltage of 900 V with a sputter current of 12-15 μA for a sample surface of about 13 mm². For this a filament current of 2.7 A for a new filament and about 1.5 A for an old filament was necessary with an almost linear degradation in between. The Ar pressure during sputtering was about $6 \cdot 10^{-6}$ mbar. Secondly, a quadropol mass-spectrometer for analyzing residual gases. Thirdly, a standard

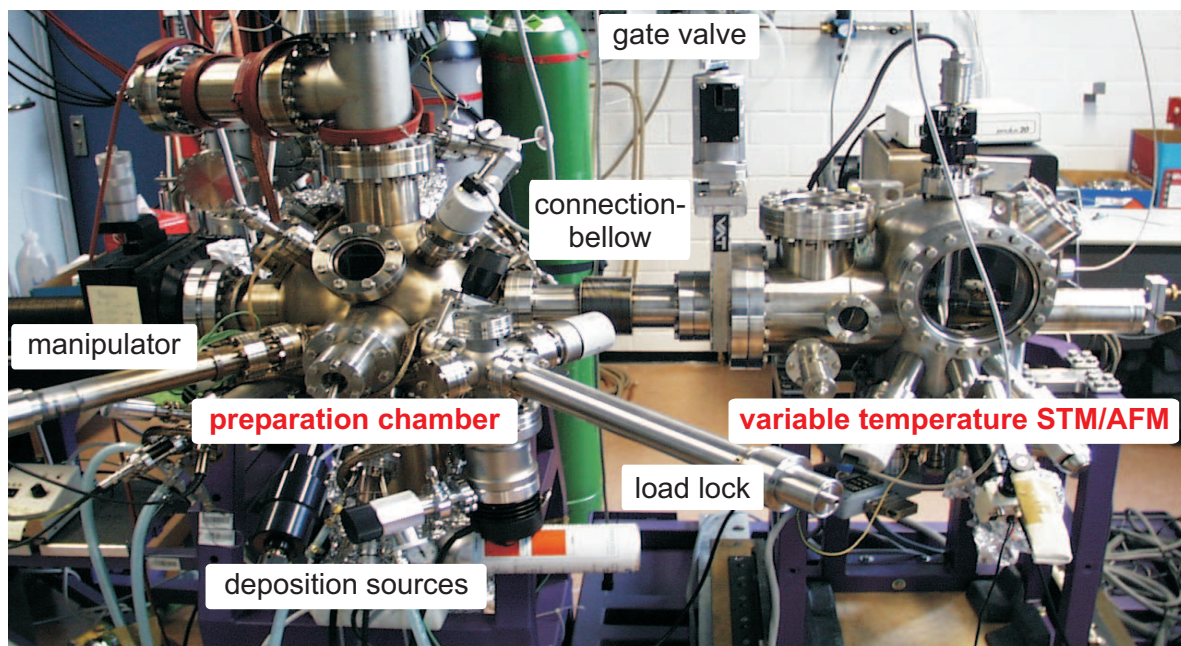


Figure 2.3: STM-Setup consisting of the preparation chamber and the analysis chamber comprising the STM.

molecular beam epitaxy source (MBE, Omicron Nanotechnology GmbH) for depositing metals such as Fe.

Next, organic molecular beam epitaxy sources for evaporating molecules, namely two single commercial sources and two home-built double sources. Both contain ceramic crucibles made of boron nitride or aluminium oxide. Heating is achieved by a metallic filament and the crucible temperature is read by a thermocouple. The temperature reading offset between the two source types turned out to be significant: when calibrating to obtain the same molecular flux with the same molecule, the commercial source showed a 35 K lower reading (at 460 K) than the home-built one. The home-built sources have been installed on retractable load mechanisms which allow a molecule change without breaking the vacuum of the chamber. This also prevents a total evaporation of the molecules which might occur when baking the whole setup at high temperatures. Fine dosing valves for dosing gases (especially oxygen for deposition and Ar for sputtering) are also mounted onto the preparation chamber.

The vacuum in this chamber is maintained by a turbo pump (Leybold, 360 l/sec) which allows to reach a base pressure of $1 \cdot 10^{-10}$ mbar. We have later added also an ion pump (Meca 2000, 400 l/sec) which is able to keep this vacuum when the turbo pump is shut off and isolated from the system by a plate valve to avoid vibrational

noise during STM measurements. The preparation chamber also contains a load lock for fast sample and tip transfer from outside. Finally, the chamber comprises a home built sample preparation stage mounted on a manipulator. Heating of the sample is achieved by a special filament in the sample holder, as will be explained in detail in chapter 3. The manipulator is also used to transfer the samples to and from the STM chamber without breaking the vacuum. The connection is made via a bellow to reduce vibrations on the STM chamber and via a gate valve to separate the vacua.

The STM chamber is pumped by a smaller ion pump (Varian, 150 l/sec). The base pressure in this chamber is in the low 10^{-11} mbar region, which allows to measure even reactive metal surfaces such as Cu over periods of several days or even a week without significant surface contamination. The chamber contains a sample carousel in which 12 samples or tip holders can be stored. No deposition sources were mounted to the chamber, only a fine dosing valve for in-situ deposition of oxygen. The STM itself is a commercial variable temperature STM/AFM (Omicron Nanotechnology) which is designed to work in the nominal temperature range of 25 K to 750 K. The lower temperature limit applies only for specific low temperature sample holders which prevent sample heating and were thus not used in this work. With the commercial resistive heating type sample holder, the nominal lowest temperatures is about 45 K when cooling with liquid He and about 110 K when cooling with liquid Nitrogen. The cryostat for cooling is a flow cryostat which can be coupled to the STM head via a moveable Au-cold-finger. The STM head itself is mounted on a very effective eddy-current damping stage for vibration isolation. Additionally, the whole STM chamber is mounted on a passive damping system (Newport). Unfortunately, strong problems persisted in the use of this passive damping system as explained the following section. Sample heating is possible either by counter-heating the cryostat upon cooling or by directly heating the sample through the heating mechanism of the sample holder (see chapter 3). In the STM position, the highest possible temperature reached was about 700 K although the scanning conditions significantly declined above 500 K.

The measurements have been performed on two Cu(110) crystals and one Ag(100) crystal. The miscut angle of the Cu(110) crystals was smaller than 0.1° , which allowed terrace widths of up to 200 nm. Tungsten tips were used for all measurements, which were stored also in the carousel. As tips can easily be re-prepared on a metal surface by “dipping” them into the surface [89], overall only 8 different tips were used for the measurements presented here.

2.4.2 STS

While STM measurements were routinely performed on the system, STS measurements showed the limits of the experimental setup. Low-frequency noise typical of mechanical pumps (e. g. Leybold, 1400 rotations per minute = 23.3 Hz) was found to be reflected in low temperature STS spectra. Although all mechanical pumps inside the laboratory were switched off during scanning, the noise of heavy mechanical pumps in neighboring labs was found to be strong enough to penetrate into the system. The main reason for this resides in the fact that in order to obtain a good cooling contact, the cold finger of the cryostat is firmly connected to the sample, thus partially bridging the eddy current damping isolations. In these conditions the system is supposed to rely on the passive damping isolation that should decouple the STM frame from the soil. Unfortunately, this is not the case because of the design of the STM frame, which had been built before the beginning of this work. The center of mass of the whole setup is so strongly outside of the working range of the passive damping system, that damping cannot be properly achieved. The only viable solution is the construction of a completely new frame. A newly adjusted design has recently been devised and will be installed within the next few months.

Although low temperature STS turned out not to be possible with the present setup, STS measurements at room temperature were only slightly influenced by the low frequency noise as the eddy-current damping system was able to sufficiently damp the oscillations.

For all STS measurements, a Lock-in amplifier was used to improve the signal to noise ratio. In the Lock-in technique a high frequency f_L sinusoidal reference signal is added to the DC bias voltage V . In Fourier space, this shifts the bias signal from the low frequency region where a high $1/f$ noise is observed to the high frequency range. The demodulation of the measured current signal I creates signals at the original low frequencies and at $2f_L$. The former is proportional to the derivative $\partial I/\partial V$ [90] and thus according to Equation (2.9) related to the sample LDOS. The $\partial I/\partial V$ -spectra recorded with the Lock-in were always checked against $\partial I/\partial V$ -spectra generated by software differentiation of the I/V -curves.

The software factory settings for the STS measurements were strongly changed after having tested different configurations [91]. Long acquisition times for individual points of the spectra were found to be necessary to overcome the residual noise problem. The

overall time necessary for one point of the spectrum was thus quite long (≈ 20 ms). The total time available for a full spectrum is experimentally limited by the time for which the system remains stable in open feedback conditions. This was determined by opening the feedback loop and checking the deviation with time of the current signal from its starting value [92]. On average, the current signal was found to stay within a limit of about ± 10 % of its original value within 1-2 seconds.

Spectra were mostly taken from -2 V to +2 V and the number of points was chosen such that the energy difference between two points (calculated as bias voltage times electric charge in eV) was similar to room temperature (26 meV) or higher. Also, the overall time for taking the spectrum was not exceeding 1-2 seconds. Several sets of parameter settings were tested for the software and the Lock-in amplifier. The best ones are reported in Table 2.1 together with possible variations still providing reliable spectra.

	parameter	used settings	possible range
STM software	I (nA) in 50 nA range	0.5	≤ 0.5 ^{a)}
	U (V) in 10 V range	-1	^{b)}
	spectroscopy range (V)	-2..2	-2.5..2.5
	acquisition time (μ s)	10240	5120-20480 ^{c)}
	delay (μ s)	10000	4000-11000 ^{c)}
	data points	80	40-120 ^{d)}
	T1 (T3) (μ s)	300	≥ 300
	T2 (T4) (μ s)	600	≥ 500
Lock-In	sensitivity (mV)	100	10-300
	ref./osc. frequency (kHz)	4.70	3.5-6
	osc. level (V)	0.010	0.005-0.012
	time constant (ms)	10	3-10 ^{c)}

further settings – STM: single points, no ramp speed

and Lock-In: auto phase, BP, Track, int, 6dB, XYV, no 2f [93]

Table 2.1: Parameters used for Lock-In-amplifier and STM software. Possible variations of the parameters for future experiments are listed in the last column. Restrictions: a) depends on the tunneling gap voltage, b) should be close to the voltage of the first spectroscopy point, c) acquisition time and delay should be larger than the time constant, d) maximum time for spectroscopy curve should be below 1-2 s in the current setup. More spectroscopy points are advisable for the future setup and low temperatures.

Drift-free images were found to be a prerequisite for taking reproducible and thus reliable spectra. The main reason is the relatively long acquisition time which together with lateral drift would result in spectra averaged over different positions (possibly molecule and bare substrate).

As the STM-software does not allow to take a series of STS spectra at the same position in a row, spectra were taken by manually defining a spatial position in the STM software. When measuring STS spectra on adsorbates, only every second spectrum was manually positioned at the adsorbate position, while the spectra in between were taken at a background position. Finally all molecular spectra were averaged as well as all background spectra and a last smoothing was applied. The final “real” spectrum was taken as the difference between the molecular spectrum and the background spectrum.

2.4.3 Sample preparation

The Cu(110) sample was cleaned by cycles of Ar⁺-sputtering (15 minutes with a kinetic energy of 900 eV and a current density of about 1 $\mu\text{A}/\text{nm}^2$) and flash annealing to 830 - 850 K. Argon as well as oxygen gas was used as supplied in metal bottles (nominal purity 5.0 and 4.5, respectively). The gases were inserted into the chamber through fine-dosing valves. The connection of the gas bottles to the fine dosing valves was formed by stainless steel tubes (delivered electrochemically purified) which were regularly cleaned by baking and cycles of flushing and pumping to $5 \cdot 10^{-6}$ mbar using a turbo pump.

Several organic molecules were evaporated from OMBE cells. TMA and TPA were inserted into the OMBE cells as delivered by the commercial supplier, L-Phe-L-Phe and D-Phe-D-Phe were first dried in a desiccator. All molecules were thoroughly degassed prior to evaporation. No significant pressure raise in the UHV chambers was observed during deposition. Table 2.2 lists the treatment procedures for the molecules.

Molecule	Supplier	Purity	Desiccator	Degassing in UHV	Evap. T.
TMA	Fluka Chemie	97%	–	≈ 40 h, up to 470 K	460 K
TPA	Fluka Chemie	99%	–	≈ 20 h up to 445 K	450 K
L-Phe-L-Phe	Bachem	99%	yes	≈ 10 h, up to 445 K	455 K
D-Phe-D-Phe	Bachem	99%	yes	≈ 10 h, up to 445 K	455 K

Table 2.2: Organic molecules: purity, cleaning, and evaporation temperature.

Chapter 3

Design of an integrated e-beam sample holder

As stated in section 2.4, the heating of the sample in the STM as well as in the manipulator of the preparation chamber is achieved by means of the sample holder. Commercially available sample holders have been specifically designed by the manufacturing company for this type of STM (Omicron Nanotechnology GmbH). Two types exist, a “direct heating” version for semiconductors and a so-called “resistive heating” version for metal and other samples. In the resistive heating type, sample heating is achieved by passing current (up to about 2.5 A) through a resistive wire ($5\text{--}7\ \Omega$, depending on the temperature) inside a boron nitride plate placed in close proximity to the sample holder. The electrical connections are made by two side bars which connect corresponding contact fingers in the STM or the manipulator head. Omicron provides a calibration chart for the electrical power that should be applied in order to reach a given temperature [94]. For cooling, the base plate of the sample holder is connected either to the cooling coupling of the STM or to the manipulator which both can be cooled by liquid He or N_2 . In order to reduce the thermic mass of the system, the whole sample holder is constructed in a lightweighted but fragile way.

3.1 The technical problem

By trying to use the commercial Omicron sample holders, we observed the following technical problems which have been independently confirmed by a number of other users of similar STM and AFM systems:

- **No temperature control:** the sample holder does not include any means of temperature measurement. The provided calibration chart has in our experiments proven to be quite inaccurate – even more as a significant dependence on the mechanical contact of the sample holder to the manipulator and especially on the annealing “history” of the manipulator was found. The reproducibility according to our measurements is worse than ± 70 K. Furthermore, the stated temperature is attained under conditions of thermal equilibrium, which is typically reached only after 12-30 minutes. So called “flash” annealings can thus not be performed with this type of sample holder. In this standard procedure, which is commonly used for crystal cleaning, the crystal is heated to a temperature of about 700-1000 K (depending on the sample material) within 2-5 minutes. Then, the temperature is shortly kept constant for few tens of seconds and finally a fast drop in temperature is needed. Using the Omicron sample holder, such annealings can in the best case be done “blindly” without temperature control, but this includes the risk to anneal the crystal to completely wrong temperatures or to even melt it. Furthermore, especially for organic molecules, a fine control of the surface temperature is often necessary. Without in-situ temperature reading (to an accuracy of at least ± 5 K) such investigations are just not possible.
- **Ineffective heating:** the employed method of heating a boron nitride plate which then by thermal radiation heats the crystal is extremely ineffective and heats the whole sample holder. This causes contaminants evaporation from heated areas and can severely damage the sample holder material itself (see below). Also, in our manipulator head, we could not reach temperatures of more than 850 K without exceeding the specified maximum power of 30 W.
- **Unusual and inflexible sample geometry:** the sample holder design requires a very peculiar sample geometry, whereas samples typically used in surface science studies have simple forms (e. g. flat shape geometries). This complicates the use of the samples in other machines e. g. with other measuring techniques. Also, the sample mounting procedure is complicated as small tolerances for positioning the crystal inside the sample holder coincide with imprecise adjustment possibilities.
- **Poor physical stability:** one effect of heating the whole sample holder is that the molybdenum components of the sample holder get hot and stick together. As

a consequence, nuts cannot be moved any more. As the whole setup of the sample holder is based on four metal posts to which all other elements are somehow screwed or pressed, this very often results in a breakdown of the whole sample holder when trying to change the sample.

- **Price:** despite of all the drawbacks of this sampleholder, it quite expensive, especially if one has to replace it frequently due to the poor mechanical stability.

3.2 Design of a new sample holder

In a first step, we have modified our existing Omicron sample holders by including thermowire contacts. This change allows to routinely use the old sample holders for all measurement purposes. On the other hand, as no reasonable change can improve the mechanical stability of the Omicron sample holders, we have chosen to design in parallel a completely new sample holder. Figure 3.1 shows a visualization of the 3D computer drawings together with a photograph of the sample holder.

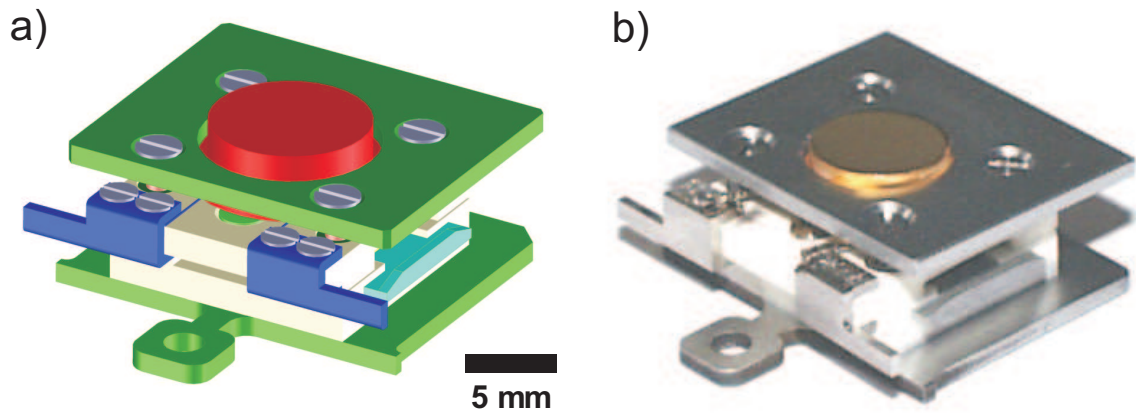


Figure 3.1: a) 3D-computer drawings for the sample holder. Red: crystal; green: metallic top and bottom plates; white: ceramic body; turquoise: electrical contacts; blue: thermowire contacts. b) Photograph of the sample holder including an Au sample.

We have kept the conditions set by the STM geometry and the electrical connection inside the STM. Instead of using a complicated sample geometry, we have designed the new sample holder for a hat-shaped samples. Other forms can also be easily implemented as long as the overall size is in the range of a disc with a diameter of maximum 11 mm and a height of less than 3 mm. As the new sample holder has only about half as many

parts as the old one and is built in a sandwich stacked way, it can be mounted easily within a few minutes. It furthermore consists of two separated parts: The lower filament part is specially encapsulated and is only to be opened for filament exchange. The upper part carries the sample and allows a quick and easy sample exchange that leaves the rest of the sample holder unchanged even in the case of a mechanical failure of any of the screws fixing the sample.

For the heating we use an electron bombardment heating (“e-beam-heating”) as is commonly done for the preparation of metal samples. A current (e. g. 2.5 A) at low voltage is passed through a filament wire inside the sample holder. Thermal radiation from this wire can heat the sample to modest temperatures (up to 500 K, see below). This allows long term measurements at slightly elevated temperatures e. g. inside the STM. For fast and high heating, a high voltage can be applied between the wire and the sample. The high voltage accelerates electrons emitted by the wire onto the sample and thus allows a focussed and very efficient sample heating. The application of a high voltage to the wire requires that both electrical contact fingers are isolated in respect to the grounded sample. This was easily accomplished in the manipulator. In the STM we have not made this change as, so far, we never had the need to heat the sample in this position at a temperature higher than 500 K. While the change in the STM reduces in principle to just cutting one connecting wire, some effort should be made in isolating the high-voltages wires from ground.

A further change in respect to the original Omicron design is the inclusion of a thermocouple to the sample holder. The sample connects individually to two wires of matching thermocouple material (type K) and closes the electrical contact so that the measured temperature is averaged over the sample. The thermowires lead to contact fingers also made of thermocouple material at the sample holder edges. Corresponding thermocouple fingers exist at the manipulator from where thermowires run to a readout device. This thermocouple circuit allows to precisely measure in-situ the temperature of the sample. Similar contact fingers can in principle be added also in the STM, the most important problem being the transfer of the thermowire to outside the STM without bridging the eddy-current-damping system.

In the design of the sample holder we have used only materials which have a high thermal conductivity. While in principle this could make the heating less efficient, it is necessary to be able to achieve low temperatures upon cooling. The cooling is transmitted from the molybdenum base plate in two ways: firstly, by four metallic posts which

connect to four metallic screws and to the metallic top plate which is pressed from the front side to the sample; secondly directly via thermo-conductive ceramics to the back of the sample.

3.3 Performance

Using only the radiation heating, temperatures of 500 K can easily be reached. The final temperature stays constant within ± 1 K, which is a very good value even for temperature sensitive STM measurements. Using the e-beam heating, the sample temperature can be fast increased. With a high voltage of only 600 V and with an e-beam emission current of about 30 mA, the sample can be heated easily beyond 1000 K as can be seen from the measurement curve in Figure 3.2a where we even started from a manipulator cooled with liquid N₂. In this measurement, we have stopped the heating at 1000 K and then again at 1150 K, in order not to melt the thermocouple wires. From the slope of the curve we can deduce that it is possible to reach even significantly higher temperatures ¹⁾. In this case a different thermocouple type has to be employed. From the visual impression of the hot crystal, the heating is quite homogeneous across the whole crystal, see Figure 3.2b.

We have tested the cooling performance using liquid nitrogen at the manipulator. Using the Omicron sample holder with an attached thermocouple wire, we reach about 95 K in our manipulator. Using the new sample holder we reach about 91 K. From this we conclude, that the cooling performance is well comparable to that of the Omicron type sample holder.

We have performed STM measurements at liquid nitrogen temperatures as well as room temperature. The stability against thermal drifts at reduced temperatures is at least as high as it is for the original sample holder. Figure 3.2 shows an atomic resolution STM image on Ag(100) which has been acquired using the new sample holder.

In the future, the heating principle of this sample holder will be included also into a new manipulator head which will be able to work with simple base plates and new as well as old sample holders. Simple base plates will be heated by the same e-beam heating mounted fixly to the manipulator. The necessary changes to apply the e-beam heating and temperature measurement also in the STM position are currently being tested.

¹⁾In fact, the only breakdown of the new sample holder type ever observed so far, occurred because of the melting of a thermocouple type K (melting point in air 1315 K [95]) while testing the heating performance and not checking the temperature reading.

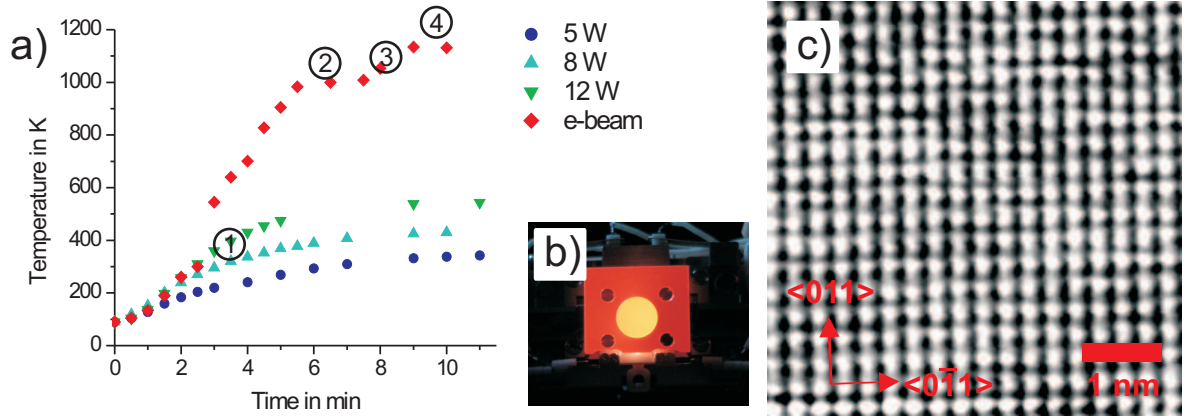


Figure 3.2: a) Sample temperatures recorded during counter heating from 90 K. Blue, turquoise, and green curves: thermal radiation heating only, red curve: heating with e-beam turned on at 1), reduced at 2) to stabilize at 1000 K, increased at 3), and stopped at 4) to avoid the melting of the thermocouple. b) Glowing sample at about 1150 K. c) Atomic resolution on Ag(100) at room temperature. Image has been corrected for the known tip distortion and low-pass filtered.

In conclusion, the new sample holder is at least equally good in all relevant properties compared to the old sample holder. It furthermore allows to in-situ measure the temperature allowing thus an efficient and accurate temperature control; it has a much more efficient heating which is important for reducing surface contamination, and its mechanical stability is significantly higher than that of the commercial sample holder.

Chapter 4

Intrinsic metal-organic structures

4.1 Introduction: Metal-organic coordination networks

4.1.1 MOCN in 3D

Crystal engineering is nowadays a wide field of structural chemistry. One important goal of this field is the creation of novel materials with tailored properties for specific application needs. While standard material science employs the large but nevertheless limited variety of the periodic table for creating new materials, crystal engineering broadens this approach by utilizing organic molecules as fundamental units. The advantage of the latter approach is the enormous variety of organic molecules which can also be tuned to exhibit specific properties using synthetic chemical methods.

Designing the geometry and dimensionality of an organic crystal has been shown to be most effectively accomplished by tuning the intermolecular bonding together with the overall symmetry of the molecules [96]. Various intermolecular interaction schemes – so called “synthons” – exist, which include electrostatic interaction, hydrogen bonding or coordination bonding. A synthon includes the use of specific functional groups of the molecules which interact via a certain type of bonding, such as two carboxylic groups which can interact via dimeric hydrogen bonding, see Figure 4.1a [96].

Metal-organic coordination bonding (section 2.3.2) is also used as synthon involving functional organic groups and metallic centers. It combines the advantages of organic molecules, namely their enormous variety and the possibility to design their functionality, with the properties of individual metallic atoms such as high magnetic moments, catalytic

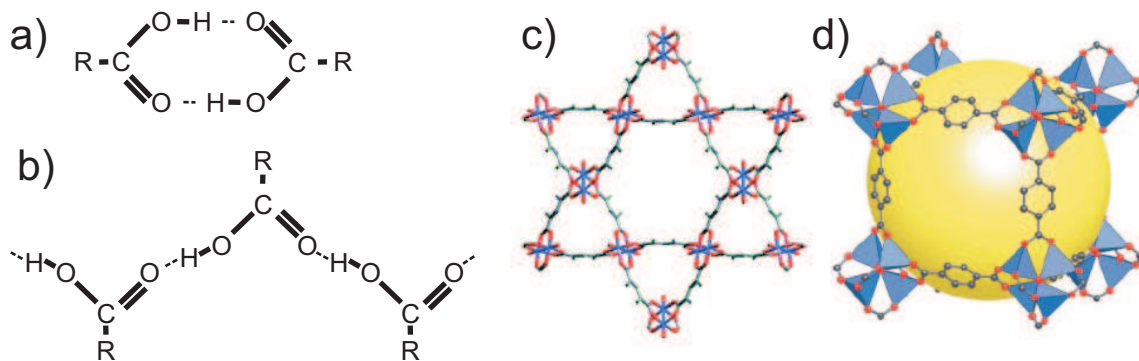


Figure 4.1: a) Dimeric hydrogen bonding of two carboxylic groups as synthon; b) monomeric hydrogen bonding as continuous interconnection, from [96]. c) and d) 3D MOCN structures. The sphere in d) is drawn to show the hollowness of the structure, from [13, 97].

activity, and a high and variable coordination. From the geometrical point of view the metal centers can be used as connection points (“nodes”) to which several (typically 2-6) organic molecules can bind. By using molecules with two or more functional groups, metal-organic coordination networks (MOCNs) can be built, e. g. in the form of small crystals, where the organic molecules interlink the metal nodes [12–14, 98]. Most of these networks are hollow structures in 3D with a porosity that is tunable through the organic linker molecule. MOCNs have been used as storage places or reaction centers for small molecules which can penetrate through hollow channels [99]. Two examples of MOCN architectures can be found in Figure 4.1c-d.

As has been explained in section 2.3.2, coordination bonding always changes the electronic filling level of its constituents through partial charge transfer. For the metal atom in a MOCN this means that its electronic occupation and thus important physical properties like e. g. magnetism or catalytic activity can be efficiently tuned by choosing a matching ligand [14]. Unlike covalent bonding coordination bonding is reversible and thus allows the formation of structures close to thermodynamical equilibrium. This induces self-organized ordering and can lead to extended domains, a high degree of spacial coherence and periodicity as well as self-correction.

Although 3D MOCNs can show interesting magnetic properties [100, 101], their application for magnetic information storage or processing is limited as no effective readout mechanism exists. In the current state-of-the art techniques any magnetic readout (or writing) requires direct access via a surface which is not given for metallic spins buried in 3D bulk [16–18]. It is thus natural to try to transfer the concept of MOCNs to surfaces.

4.1.2 Surface based MOCNs

MOCNs can in principle be fabricated using the standard procedures and then be transferred onto surfaces. For such approaches mainly highly oriented pyrolytic graphite (HOPG) [17, 18, 102, 103] or glass and mica [104] substrates have been used. On the other hand, so far, only very small networks consisting of only a few molecules have been transferred successfully [102, 103].

It has recently been shown that it is also possible to create in situ surface-MOCNs by co-depositing organic ligand molecules and metal atoms onto a substrate. Most of these studies have been performed on metal surfaces in UHV [15, 105–112]. The results obtained for these systems will be described in more detail below.

In one case MOCNs have been grown in situ at the solid-liquid interface in the form of chains on HOPG [113]. Yet, special solvent molecules were necessary to stabilize the chain structure on the surface. In another more recent study, it was shown that it is possible to obtain 2D complexation and pattern formation at the liquid-solid interface using bipyridine molecules [114]. These structures may constitute interesting objects if a high enough stability on the surface can be accomplished. For a detailed analysis, we believe that UHV conditions offer more well-defined conditions to investigate the obtained structures than investigations in solution. Nevertheless, we expect that these solution based systems might be preferable for any type of mass-produced application where sub-monolayer coverages and well-defined surfaces are less important than production efficiency.

The first molecular linkers used for the in-situ growth of MOCNs under UHV conditions were benzene polycarboxylates such as trimesic acid (1,3,5 benzenetricarboxylic acid, TMA), trimellitic acid (1,2,4 benzenetricarboxylic acid, TMLA) and terephthalic acid (1,4 benzenedicarboxylic acid, TPA) [15, 105–112]. All of these molecules are flat and consist of a central phenyl ring surrounded by two (TPA) or three (TMA, TMLA) carboxylic groups. TPA is linear, TMA has a three-fold rotation symmetry axis, while TMLA with the carboxylic groups at the ring carbon atoms 1, 3 and 4 has no symmetry within the plane of the molecule. Longer polycarboxylate molecules with more than one central phenyl groups, were employed, too [111, 115] as well as molecules including pyridyl groups [116, 117].

TMA, TPA and TMLA were used in their carboxylate form, in which they can form extended metal-organic networks on the surface, with metal centers such as Cu

or Fe. These can either be deposited from a molecular beam epitaxy (MBE) source during or after deposition of the linker molecule or they exist already as adatoms on the surface as will be explained in the following section. Metallic single crystal surfaces were used as substrates, especially Cu(100) which has a quadratic symmetry. The obtained structures are either localized 0D complexes as shown in Figure 4.2a where four TMA molecules coordinate a Cu center or extended 2D networks as in the case of Fe with longer dicarboxylate molecules shown in Figure 4.2b. In order to obtain all these structures an annealing to about 400 K was typically necessary.

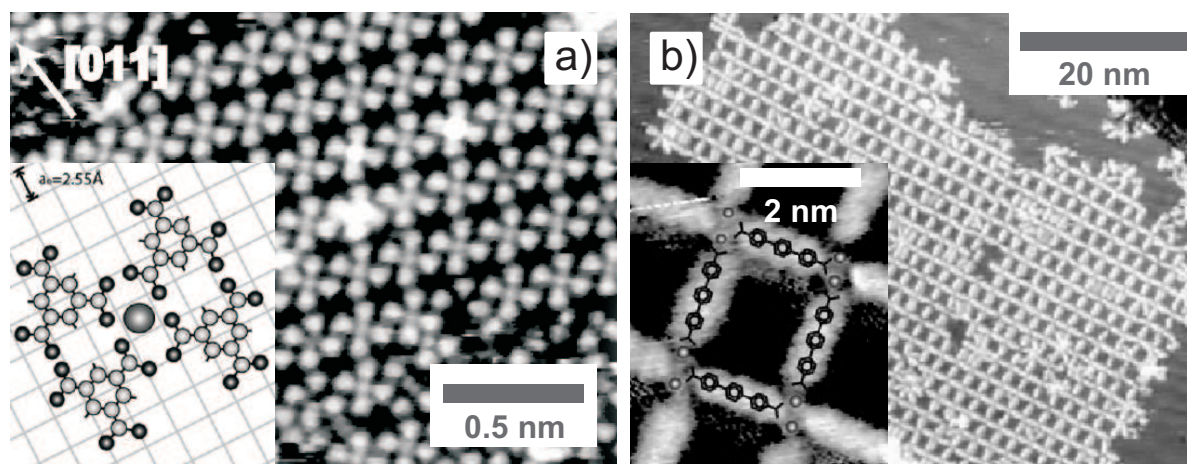


Figure 4.2: Surface MOCN. a) 0D complexes of Cu-TMA on Cu(100). Four TMA molecules coordinate the central Cu according to the model shown in the inset, taken from [106]; b) 2D network of extended dicarboxylate molecules with Fe centers [111].

4.1.3 Carboxylate formation on surfaces

It is well established that carboxylic acids deposited on Cu surfaces, may undergo a loss of the hydrogens of the carboxylic groups [118–122]. Such a process leaves behind COO^- (carboxylate) groups and is similar to the process of proton donation of acids in aqueous solution. Whereas in solution the extra protons can attach to water molecules, protons here may leave the surface as H_2 , with electrons supplied by the surface if not adsorbed at another surface position. The formation of the carboxylate group has been confirmed for several different molecules by a variety of experimental methods, including IR [118–122] and XPS [123].

Perry, Richardson, Haq and coworkers have attributed an important role in the carboxylate formation to Cu adatoms [119]. Indeed, it has recently been established that

the carboxylate formation process is catalyzed by the presence of Cu adatoms on the surface [124]. Already in the original work by Perry and coworkers it had been concluded that the reactivity of the Cu surface with respect to the deprotonation and carboxylate formation of benzoic acids depends on the number of available Cu adatoms [119].

Adatoms exist on the surface as a permanent background gas, feeded by the emission of atoms from terrace step edges and especially from kink sites. Emission and re-attachment are in thermal equilibrium on the surface, implying that there is a steady average number of adatoms present and that this number increases with the substrate temperature for entropy reasons [119]. Perry and coworkers pointed out that a number of different parameters determine the adatom surface density such as the surface energy, the coordination of adatoms on the surface, or the coordination of atoms within surface terraces. They estimated the density of Cu adatoms at 300 K on Cu(110) to be about 500 times higher than that on Cu(100) and about 10^4 times higher than on Cu(111) [119]. The main reason for this trend was found in the more “open” structure of the (110) surface with respect to the (100) orientation and even more in comparison to the densely packed (111).

When depositing organic linker molecules such as TPA, TMA or TMLA, the adatoms can serve in a double way, as they can catalyze the deprotonation and can also act as “intrinsic” metal centers for the formation of metal-organic coordination networks [106, 124].

4.2 Templated growth of MOC chains

While 3D MOCNs rely on the interplay of molecular symmetry and synthon interaction, the in-situ creation of 2D MOCNs on surfaces offers an additional set of parameters to tune the MOCN structure. As the molecular groups as well as the metallic atoms prefer specific adhesion positions (“sites”) of the surface, its geometry can predefine the adhesion structure of a metal-organic complex which may translate to the structure of the whole MOCN.

We will show here that by exploiting the structure of the surface it is possible to template the growth of the MOCNs. By using the anisotropy of a 2-fold low-symmetry fcc (110) surface, 1D metal-organic coordination chains (MOCCs) are created with the same technique employed for the growth of 0D and 2D MOCNs [15, 105–112, 115–117].

In order to point out the templating effect, we have used the Cu(110) surface (see

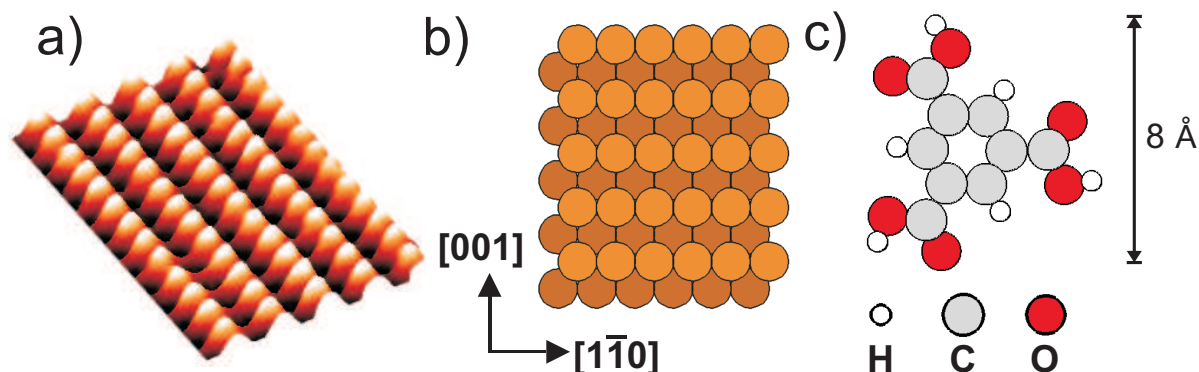


Figure 4.3: a) High resolution STM image in 3D representation and b) structural model of the Cu(110) surface. c) trimesic acid (TMA).

Figure 4.3a-b) which has a similar chemistry but a different geometry in respect to Cu(100). The unit cell size of Cu(110) is $a_0 = 3.615 \text{ \AA}$ along the $[001]$ direction and $\sqrt{2}/2 \cdot a_0 = 2.556 \text{ \AA}$ along the $[1\bar{1}0]$ direction, where a_0 is the Cu lattice constant for bulk Cu. As can be seen from Figure 4.3a, the corrugation of the Cu(110) surface is significant and diffusion on such a surface is expected to happen mainly along the $[1\bar{1}0]$ direction (see e. g. reference [125]). From a chemical point of view, Cu(110) is expected to behave similarly to Cu(100) although it is expected to have a slightly higher reactivity because of the lower coordinated surface atoms. Moreover, the formation of Cu-based metal-organic complexes should be easier on Cu(110) than on Cu(100) because of the higher free adatom gas density.

The templating role of (110) surfaces of fcc crystals has been used before to create unidirectional structures for atoms [22–26] and molecules [27–29]. The (110) surfaces of some transition metals are thermodynamically close to reconstruction. Reconstructed (110) surfaces have also been used as templates [30–34]. It should be noted that upon deposition of molecules or specific elements like oxygen and nitrogen a surface reconstruction can occur which fundamentally change its templating effect [52, 126, 127] as will be discussed in section 7.1.

We have chosen TMA as a molecule which is not at all ideal for a 1D-like linear geometry to highlight the templating effect of Cu(110). As the three carboxylic groups of TMA are ordered in a planar triangular shape around the central phenyl ring (see Figure 4.3c), TMA comprises a threefold rotation symmetry that mostly translates into a hexagonal supramolecular geometry. Architectures containing only TMA in its standard

tri-acid form often show dimeric hydrogen bonding as synthon between the carboxylic groups of neighboring molecules resulting in hollow 2D hexagonal “honeycomb” networks which are found in 3D-bulk-crystals [128, 129] as well as on low interacting substrates like in solution on HOPG [130] and Au(111) [131, 132] and in UHV on Ag(111) [124], and on Ag-passivated Si(111) [133]. For illustration, TMA on Ag(100) is shown in Figure 4.4 for which we found again the same hexagonal behavior. If on the other hand, TMA is in its deprotonated tri-carboxylate form (comprising three COO^- groups, see sections 4.1.2 and 4.1.3) it can effectively bind to metal centers giving rise to another manifold of molecular architectures, which are mostly also of hexagonal symmetry [97, 134] or arrange in 2D sheets [135].

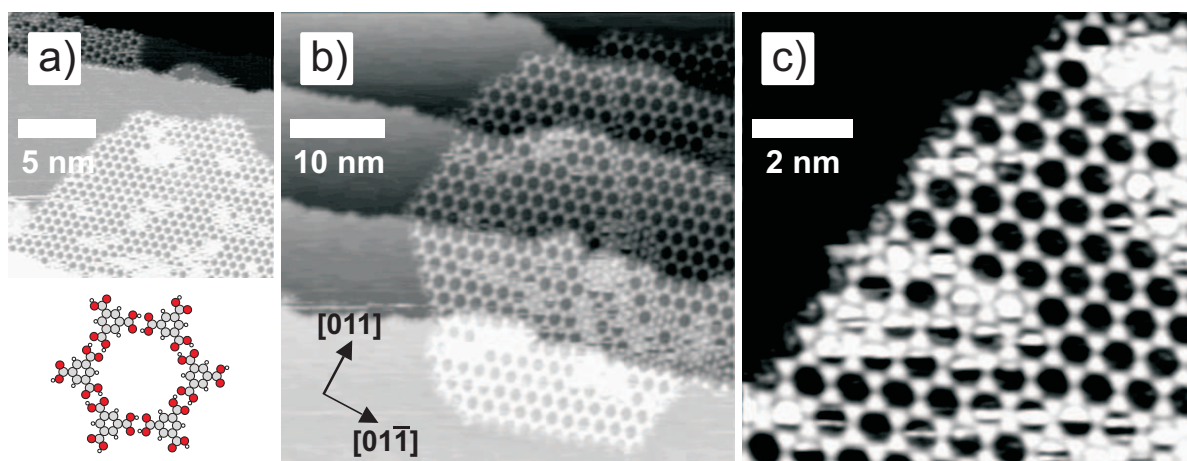


Figure 4.4: *TMA/Ag(100) at around 110 K forming honeycomb networks. Each honeycomb ring is formed by six TMA molecules that interact via dimeric hydrogen bonding. Some honeycombs are filled, probably with extra TMA molecules.*

As explained above, TMA forms 0D complexes on Cu(100) (see Figure 4.2a) upon deposition at 300 K and annealing to 400 K. Yet, upon deposition below 280 K, hydrogen mediated honeycomb motives are found which are attributed to the typical dimeric hydrogen bonding [105]. In order to be able to compare the results for Cu(110) with those for Cu(100), we have performed a series of experiments in which TMA has been deposited on Cu(110) at increasing substrate temperatures. In a combined effort we have used variable temperature scanning tunnelling microscopy (VT-STM), density functional theory (DFT), low energy electron diffraction (LEED), and reflection absorption infrared spectroscopy (RAIRS) to analyze the obtained structures. The results of these experiments will be shown in the following sections. The analysis of the 1D chain structures

observed at temperatures of 300 K and above will then be discussed in detail in section 4.3. This chapter will be limited to the case in which the metal centers necessary for the creation of metal-organic complexes are provided by the surface itself and are thus of the same element as the surface. The complexes arising from this will be called “intrinsic” MOCNs. “Extrinsic” MOCNs will be discussed in chapter 5.

4.2.1 TMA deposition at 130 K

For the deposition of TMA on Cu(110) we have used the parameters listed in section 2.4.3. Deposition at 130 K does not result in a significant structure formation. When investigated by STM, flat triangles are observed on the surface which can be assigned to flat-lying TMA molecules [105–107, 109, 130–132]. The molecules partially form clusters without specific substructure or are scattered on the surface with no recognizable specific alignment (see Figure 4.5).

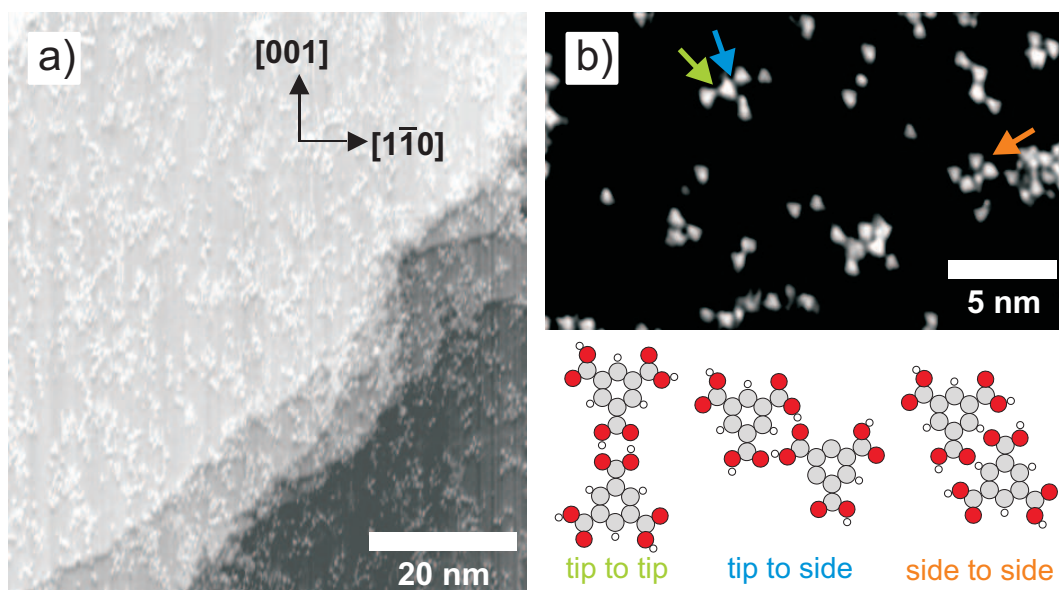


Figure 4.5: TMA deposited onto Cu(110) at 130 K. Following deposition, the substrate was fast cooled to 40 K for measurements. a) Overview image at 100×100 nm and b) enlarged image and frequent bonding motifs.

While long range correlations and ordering can be ruled out, neighboring molecules seemingly interact, and a partial short range intermolecular alignment can be recognized. On the contrary, no specific step attachment of TMA molecules is observed. This signifies intact carboxylic acid groups of the TMA molecule since deprotonated carboxylate

groups are expected to interact strongly with low coordinated Cu atoms at step edges as will be explained in section 4.3. Hydrogen bonding is thus expected as intermolecular interaction mechanism as this is typically observed for TMA comprising intact carboxylic acid groups [105, 130–132].

A “tip-to-tip” alignment of neighboring molecules is often found in which the carboxylic group at the “tip” of a TMA molecule points to that at the tip of a neighboring one. This implies a dimeric hydrogen bonding as explained in Figure 4.1. “Side-to-side” and “tip-to-side” attachments of neighboring TMA are also occasionally observed which would, depending on the intermolecular distance, also allow hydrogen bonding. Similar bonding motifs are also observed, which can also be attributed to hydrogen bonding. We interpret the absence of any long and medium range ordering as the result of hindered surface diffusion induced by the low substrate temperature.

4.2.2 IR measurements at low temperatures

IR measurements were used to further analyze the adhesion (see section 2.2.1). The measurements were carried out in the Surface Science Center, Liverpool, UK in the group of R. Raval and S. Haq. Figure 4.6 shows a series of IR spectra for increasing coverage during TMA deposition on Cu(110) at 85 K. All curves are relative to the spectrum of clean Cu(110) (see vertical scale-bar for an absolute value of the variation of signal strength). For low coverage (Figure 4.6a-d), bands are found at 743, 940, 1427 and 1643 and 1708 cm^{-1} . With increasing coverage broad features are found in the region between 1240 and 1440 cm^{-1} and at 3265 cm^{-1} . A strong signal appears at about 1750 wavenumbers. The negative peak at about 2300 cm^{-1} is a CO_2 signal within the infrared spectrometer.

For assigning the bands in this and all following IR spectra different resources were used. IR spectra of a 3D-Cu-TMA polymer [135] and of TMA and different benzene carboxylic acids [136] provided an insight into the TMA carboxylate modes undisturbed by the substrate. Comparisons to IR investigations of other carboxylic acids [72, 118–122] on the same substrate and to TMA on Au(111) [137] were used to identify the modes of Cu(110) adsorbed TMA. Table 4.1 provides a rough overview over repeatedly encountered modes.

The band at 743 cm^{-1} which is visible in all spectra is attributed to the out-of-plane C-H bend of the phenyl group. The 940 cm^{-1} likewise is the out-of-plane O-H bend,

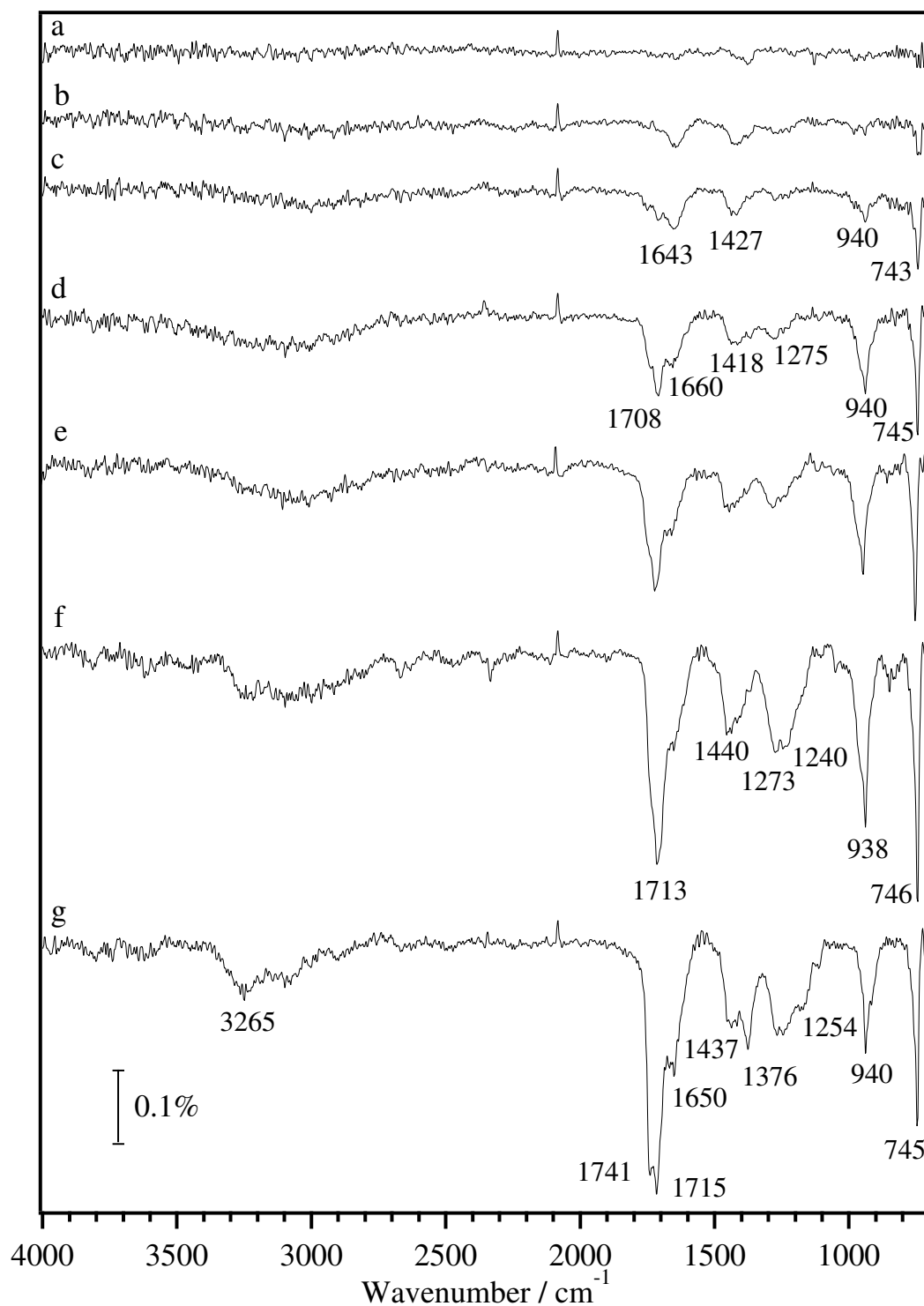


Figure 4.6: RAIRS measurements of TMA/Cu(110) at 85 K. Series of increasing coverage. All spectra are relative to the spectrum of a clean substrate. A precise coverage calibration is not possible but from a rough calibration using LEED at higher substrate temperatures (see e. g. section 4.3) we can suppose that spectrum b corresponds to a situation as depicted in Figure 4.5a.

Peak (in cm^{-1})	Origin	orientation	deprotonated/acid
750	phenyl C-H bend	out of plane	both
940	O-H bend	out of plane	acid
1250	C-O stretch	in plane	acid
1150-1400	C-O-H bend	in plane	acid
1350-1450	symmetric carboxylate stretch	in plane	deprotonated
1500-1650	asymmetric carboxylate stretch	in plane	deprotonated
1720-1750	C=O stretch	in plane	acid
3060	phenyl C-H stretch	in plane	both
2600-3600	O-H-stretch	in plane	acid

Table 4.1: Repeatedly encountered IR modes. Peak positions as found in the spectrum, physical origin of the mode and orientation of the dynamic dipole moment relative to the TMA molecule plane. Broad frequency ranges are mostly due to hydrogen bonding.

its broadening in comparison to the 743 cm^{-1} being due to H-bonding [119, 122, 136]. The visibility of these two modes shows that the molecule is flat-lying indeed. The frequencies between 1100 and 1450 cm^{-1} are assigned to C-O stretch and C-O-H bend modes with frequencies depending on the degree of hydrogen bonding [72, 137]. The 1643 cm^{-1} mode is a signature of a asymmetric carboxylate. Its occurrence signifies (partially) deprotonated TMAs which are either upright standing or flatlying with a carboxylate group bending to the substrate for bonding. The signal is not dominant here so that we can assume that only a fraction of all groups is deprotonated.

The strong peaks in the area from 1708 to 1750 cm^{-1} originate in the C=O stretch with the lower wavenumbers being formed by groups involved in hydrogen bonding and the upper once being free of this. The mode at 3165 can be likewise attributed to the O-H stretch [122, 135–137]. It can thus be shown that most of the functional groups retain their acid character as strong signals from the acid groups are obtained. H-bonding between protonated groups is likewise observed from the shifts of the peaks. The onset of the C=O stretch at high coverages (from spectrum d onwards) indicates upright or at least upright tilted carboxylic molecules. The strong rise of the peak with coverage is assigned to molecules which are found in an upright configuration either due to packing in limited space or due to being accumulated in a second or higher layer. The non-existence of this peak at low coverage (spectra a-c) shows that the IR is thus consistent with flat-lying molecules which in some cases may interact via hydrogen bonding.

4.2.3 TMA deposition at 240 K

Increasing the substrate temperature (during or after deposition) does not significantly affect the molecules up to temperatures of at least 210 K. It should be noted, though, that from 210 K on very rarely (a few percent of all TMA molecules) structures are found locally which resemble those found at higher temperatures (see section 4.2.4).

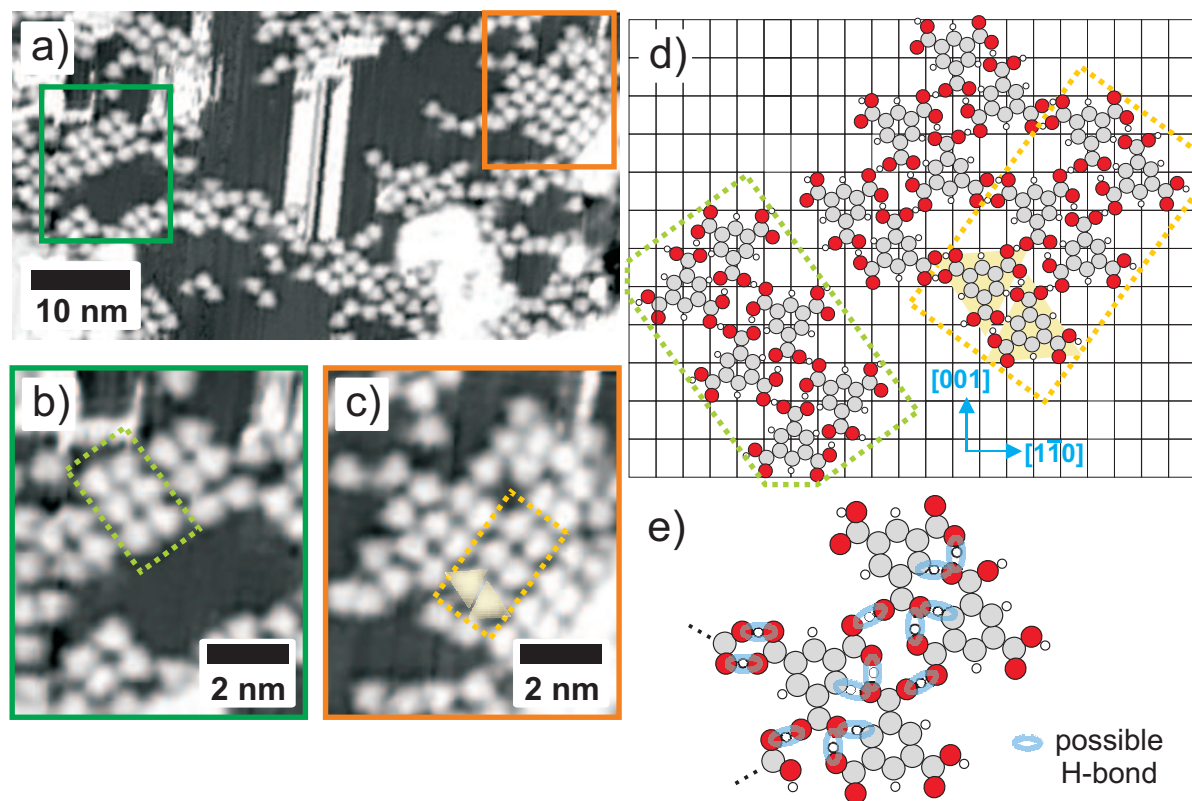


Figure 4.7: TMA deposited onto Cu(110) at 250 K. Following deposition, the substrate was fast cooled to 40 K for measurements. a) The TMA molecules form small networks of two different chiralities, b) and c) enlarged view of chiral domains, d) model of the adhesion geometry for both chiralities, e) enlarged view, on the possible hydrogen bonds.

At substrate temperatures of 240-250 K a more ordered phase is observed (see Figure 4.7a). TMA forms local arrangements of densely packed molecules that typically extend over several nanometer and thus incorporate some dozens of molecules. The island formation is chiral, as islands of different chiral packing are observed as can be seen from comparing Figure 4.7b and c. The chiral chains are found to grow along an orientation which is tilted by $\pm (55 \pm 3 \text{ deg})$ out of the $[1\bar{1}0]$ direction of Cu, where the clockwise direction applies for the domain in Figure 4.7b and the counterclockwise direction for the mirror-symmetric domain in Figure 4.7c. These orientations correspond

to the $[1\bar{1}2]$ and the $[112]$ directions, respectively. Inside the chiral domains the molecules are all tilted by a small angle of $\pm (5 \pm 3 \text{ deg})$ from an orientation in which they would have one side aligned to the $[1\bar{1}0]$ direction. This angle is measured by comparing the orientation in islands of opposite chirality. The tilt is clockwise in Figure 4.7b and anticlockwise in Figure 4.7c. We assume that this little twist from a high-symmetry orientation improves the bonding possibilities inside the domain. Chirality thus depends on the molecule packing inside the island and is reflected in a small chiral twist of the individual molecules.

From the measured angles and intermolecular distances it was possible to establish a tentative model of the adhesion structure which is shown in Figure 4.7d. As we cannot determine positions of the molecules in respect to the underlying Cu atoms, the substrate lattice is just shown as a grid representing the surface periodicity. All TMA are placed on equivalent substrate positions. Four possible orientations exist, given by the two orientations of the TMA tips along $+$ or $-[001]$, each of which can be twisted either clockwise or anticlockwise by 5 degrees. In a chiral domain only molecules of the same twist direction are found. The molecules form double rows (highlighted in green and yellow in Figure 4.7b-d) that are connected by dimeric hydrogen bonding (see upper right part of Figure 4.7d). Within the double row multiple-hydrogen bonding is possible. In particular, in this configuration oxygen atoms can form electrostatic interactions with two hydrogen atoms of neighboring molecules belonging to the carboxylic group and to the phenyl ring. It should be noted that these bonds are possibly less strong. In fact, only a slight rotation out of a high symmetry molecular orientation allows to form these many hydrogen bonds. In Figure 4.7e a set of four molecules is shown in an enlarged view and the possible places for hydrogen bonds are highlighted. When dividing the total number of possible bonds by the number of TMAs (thus attributing each bond unambiguously to one TMA) the number of bonds per TMA is thus four. This is higher than the number of three in the honeycomb network.

When comparing the model in Figure 4.7d to the STM images in Figure 4.7a-c a high degree of agreement is reached. Not only the molecular positions and orientations are in agreement, also the small free Cu areas inside the islands agree in their shape between the model and the STM images.

Here we have assumed hydrogen bonding as intermolecular interaction. We cannot exclude the presence of adatoms inside the structure which would allow to form metal-carboxylate bonds for deprotonated TMAs. As the structure seems to be optimized for

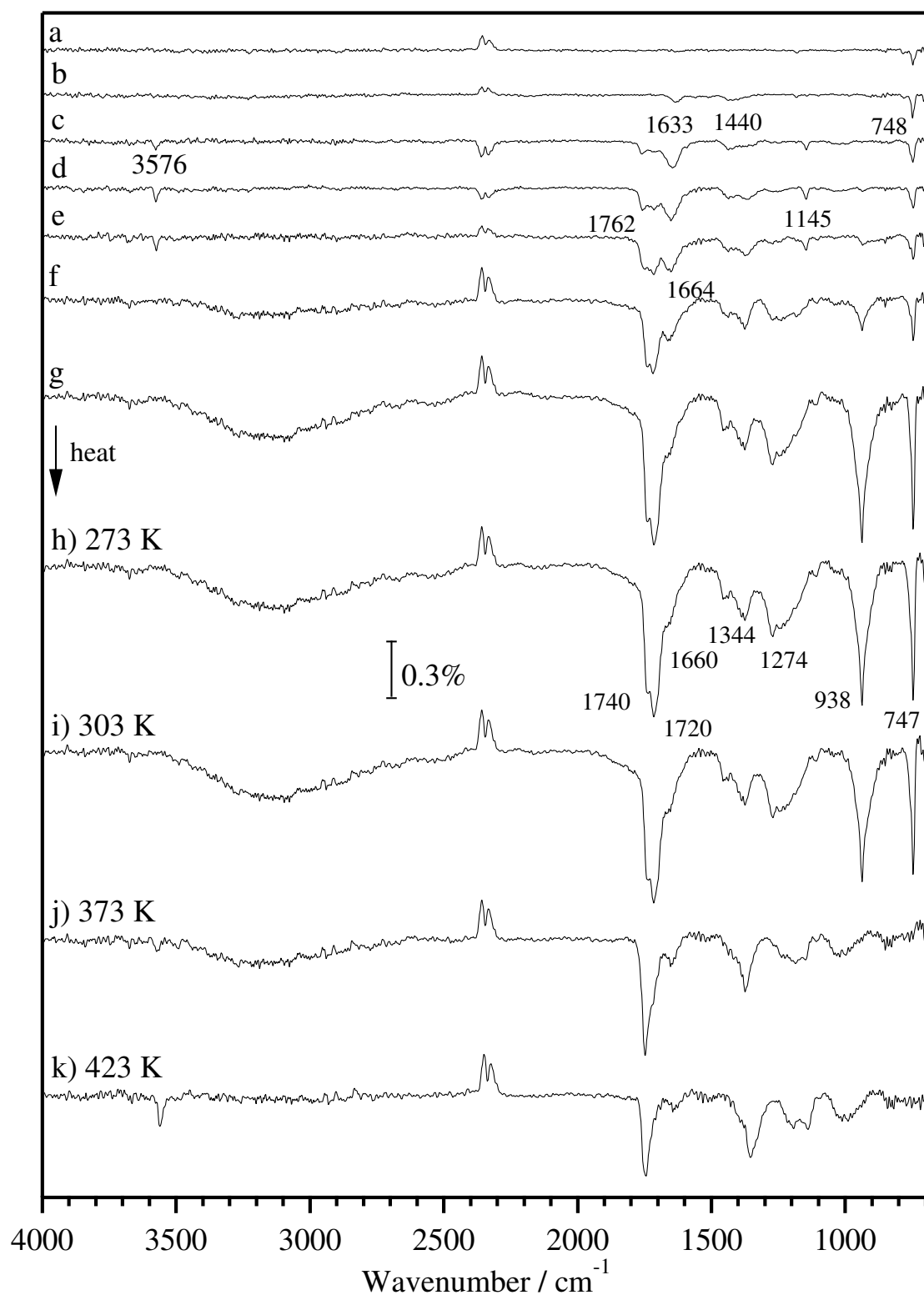


Figure 4.8: Measurement of TMA/Cu(110) at 250 K. a-g: series of increasing coverage, h-k: subsequent stepwise annealing. The effect of annealing is described in section 4.4.3. The positive peak is due to CO_2 within the spectrometer.

multiple hydrogen bonding we nevertheless favor this bonding mechanism as the most probable. Also, from STM we see that again only few molecules seem to attach to step edges (more though than at 130 K) providing again an indirect proof of intact carboxylic acid groups and thus hydrogen bonding.

The IR spectra taken at this temperature (see the spectra a-g in Figure 4.8) are generally similar to those at 85 K (see Figure 4.6). The same peaks are observed, with slightly different relative weight. The 940 cm^{-1} mode appears only at higher coverage than for the 85 K spectrum. This may signify less O-H absorbers and thus more deprotonated carboxylate groups. Partial deprotonation can thus be assumed but it is not clear, if all molecules are partially deprotonated or if some molecules have more and others less deprotonated groups. In general, the overall chemical picture is not much different at 250 K from what it was at 85 K.

4.2.4 Chain formation at room temperature and above

Deposition of TMA at substrate temperatures of 280 K and higher results in the formation of patterns clearly distinct from the low temperature behavior described above. The same effect can be achieved by annealing the low-temperature structures at 280 K or higher.

The main feature of this new type of structure is that it is unidirectional, consisting of individual chains running along the $[1\bar{1}0]$ direction of the Cu(110) surface, see Figure 4.9. The chains are formed alternately by triangles, which again are attributed to flat-lying TMA molecules [105–107, 109, 130–132] and by round protrusions. Following previous analysis on Cu(100) it can be safely concluded that the round protrusions are formed by Cu adatoms [105–107, 109]. The apparent height of the TMA molecules of $140 \pm 30\text{ pm}$ is nearly double the height of the Cu protrusion of $75 \pm 20\text{ pm}$ when scanning at -1 V and 1 nA . Faint protrusions at the end of the chains suggest, that the chains are terminated by Cu adatoms (see Figure 4.9). One side of the TMA triangle is aligned to the $[1\bar{1}0]$ direction of the Cu substrate, implying that one functional group on each side is facing the Cu adatoms. The third functional group of the TMA molecules points perpendicularly out of the chain. The whole structure can thus be described as a metal-organic coordination chain (MOCC).

While for deposition temperatures around 300 K the chains are typically kinked, a post-annealing at 380 K (typically one minute) or directly a deposition at this tempera-

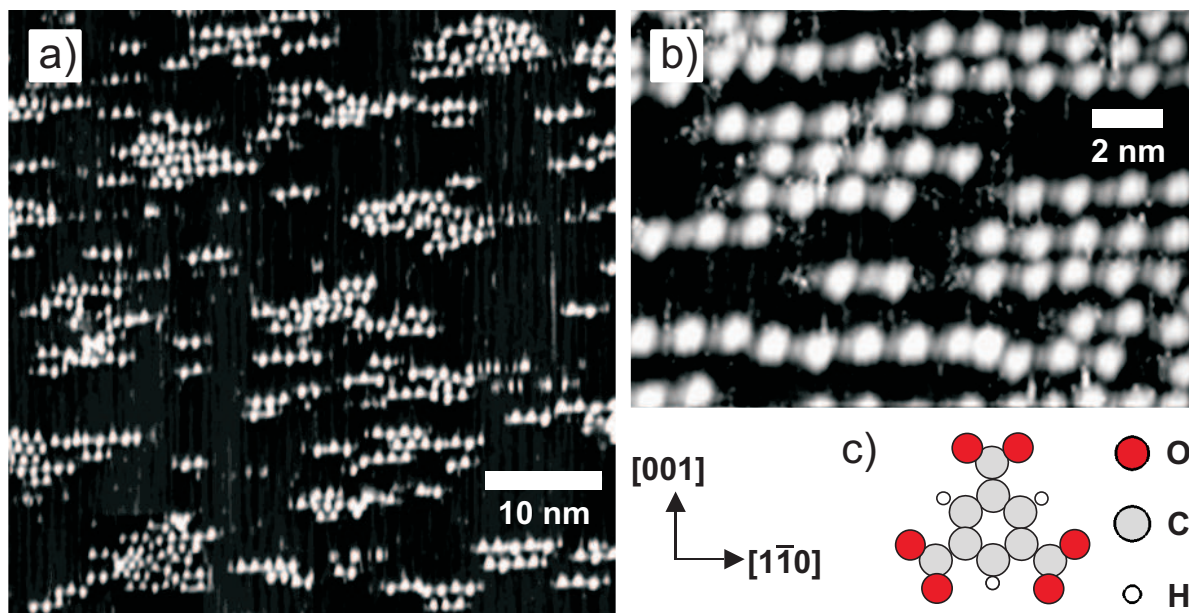


Figure 4.9: a) and b) Representative STM images for TMA supramolecular structures created around room temperature. Although the chains show kinks and irregularities and tend to cluster, the supramolecular geometry is already unidirectional. a) TMA deposited at 240 K then annealed to around 280 K. b) TMA deposited at 300 K, enlarged view. c) Deprotonated TMA.

ture creates straight and highly ordered chains (see Figure 4.10). The structure of these ordered chains is basically the same as for the chains grown at 300 K, yet they are much more ordered on a larger scale and are straight and nearly free of kinks. For the chains grown at 280 K-300 K we can not fully exclude the partial occurrence of some protonated carboxylic groups, due to the clustering observed in Figure 4.9. For the annealed chains, on the other hand, no such clustering is observed (see Figure 4.10) and we are sure that all functional groups are fully deprotonated (see also the results of the IR measurements below). An even higher annealing has shown to yield no further change to the structure even up to temperatures well beyond 500 K, where the desorption of TMA was found to occur. These annealed MOC-chains will be referred to as MOCC-S (with “S” for single-chains) hereafter and will be described in detail in section 4.3.

For low coverage of <0.04 monolayer (ML) there is a predominant attachment of chains to step edges with a TMA-molecule as first element of the chain, showing the affinity of TMA to low coordinated Cu-atoms (see Figure 4.10a). For coverage >0.04 ML TMA nucleates also on the terraces (see Figure 4.10b). With increasing coverage, the chains become longer and denser until the whole surface is filled and chains run all the way across terraces (see Figure 4.10c). Above this limit, two denser packed phases

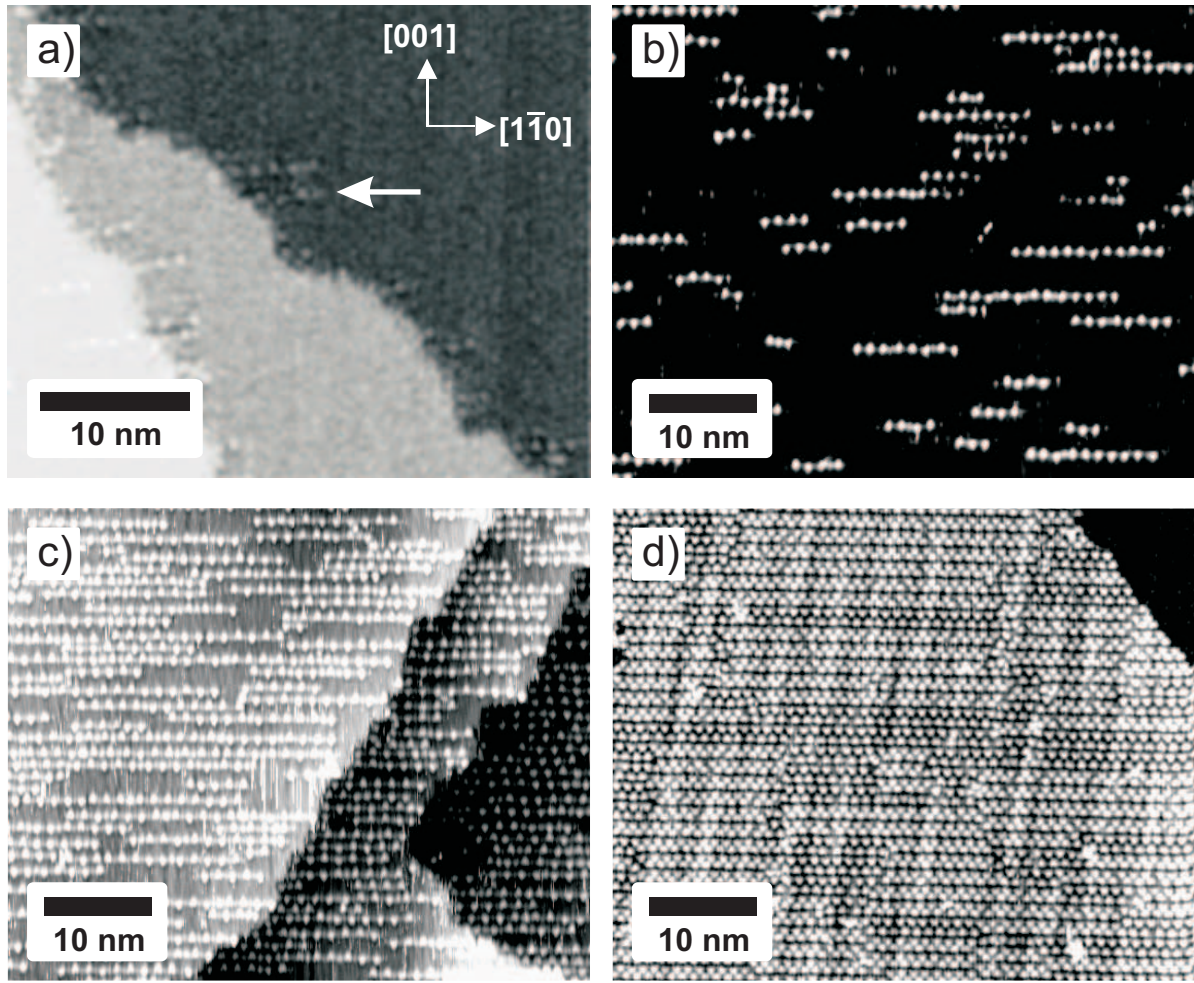


Figure 4.10: Representative STM-images of TMA/Cu(110), deposited at 300 K a)-c) annealed to 380 K, d) annealed to 500 K. Coverage: a) step attachment at 0.02 ML (indicated by arrow), b) MOCC-S on terraces at 0.07 ML, c) surface nearly covered with MOCC-S at 0.36 ML, d) denser packed phases at 0.9 ML (detailed discussion follows in section 4.4).

nucleate, first a transition phase (referred to as MOCC-T) and at even higher coverage a double chain phase (MOCC-D), which can coexist with each other (Figure 4.10d) as will be described in section 4.4. Only after the MOCC-D has completely covered the substrate, the formation of a second layer starts. In the following all coverage values will be given in ML, whereas 1 ML signifies the coverage reached for a complete ideal MOCC-D phase just before the nucleation of a second layer. In this normalization the single chain MOCC-S phase spans the coverage range from 0 ML to about 0.53 ML.

The presence of the Cu protrusions which connect the individual TMA molecules in the single chains together with the step attachment can be seen as a strong hint for the deprotonation of the TMA molecules and the complexation of Cu adatoms. Most

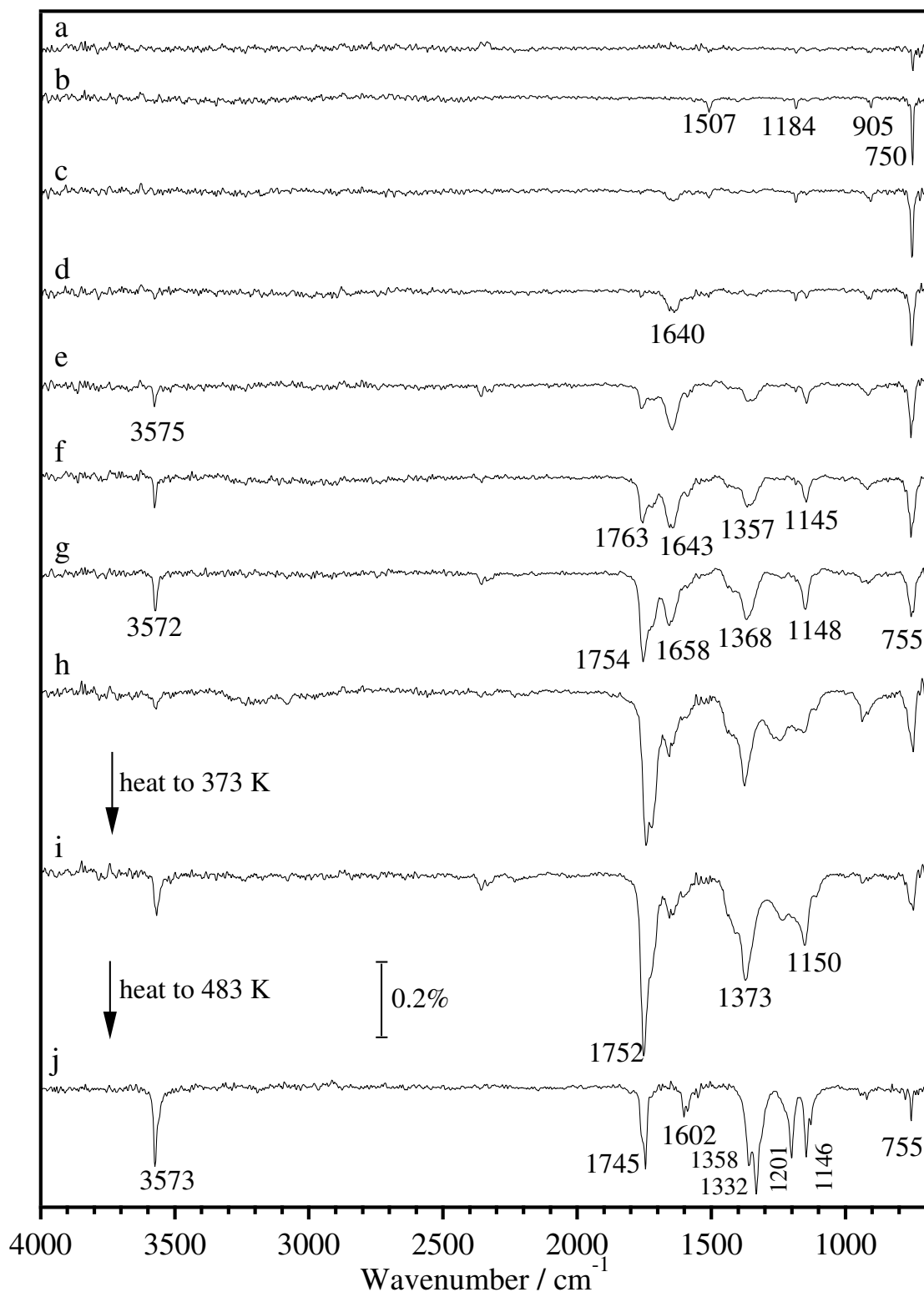


Figure 4.11: Representative RAIRS spectra series of increasing coverage taken at 300 K. The MOCC-S phase is represented by the spectra a-c. The higher coverage phases will be discussed in section 4.4.3.

evidence, nevertheless comes from the IR spectra. A representative IR spectra series taken at 300 K is shown in figure 4.11. The low coverage phase which is discussed here (<0.53 ML) is represented by the spectra a-c. Bands are found at 750, 905, 1184 and 1507 cm^{-1} . More bands appear at higher coverage which will be discussed later on. The strongest band at 750 is again the out-of-plane C-H bend of the phenyl ring. From its visibility the flat-lying orientation of the molecule is confirmed. The signal at 903 cm^{-1} could in principle derive from the out-of-plane O-H bend mode which was found at 940 cm^{-1} at lower temperatures. But on the other hand, it is expected to be shifted to wavenumbers lower than 800 without hydrogen bonding [72]. As hydrogen bonding motifs are not observed by STM, the origin for this band is more likely to be found in a C-C bend of the phenyl group [72, 136]. The mode at 1184 cm^{-1} is similar to that of an in-plane C-O-H bend of an acid group but as other acid modes are not observed, this possibility can be ruled out and we cannot attribute this mode here. Contrary to what was observed at lower temperatures, no other acid features are found between 1100 cm^{-1} and 1450 cm^{-1} . The mode at 1506 cm^{-1} is due to the asymmetric stretch of the carboxylate group. Its frequency is as expected for a carboxylate group bound to a Cu atom [72, 122, 136]. These IR spectra thus show big differences in comparison to the low temperature data presented above. Especially the appearance of the carboxylate mode and the non-existence of the acid features below 1400 cm^{-1} proof the importance of the deprotonation for the formation of the chains.

The IR spectra obtained for a low coverage of TMA at 300 K and 370 K (for a as deposited and an annealed MOCC-S) do not differ significantly. It thus can be concluded that the improvement of the structural regularity observed by annealing to 380 K is not due to a chemical change (such as a further deprotonation or a significant reorientation of the molecule resulting in a different chemical bonding). This annealing thus only improves the long-range order through a redistribution of unchanged constituents.

4.2.5 Chain length

The chain formation can be seen as a submonolayer 1D island growth. On a mesoscopic scale (as is e. g. in the images in Figure 4.10) such a process can be described only by statistical methods [49]. One possibility to statistically quantify the chain growth is to plot the chain length distribution at different coverages as shown in Figure 4.12 where the occurrence of chains of size s is plotted. For normalization, s has been divided

by the average island size S for each coverage. The ordinate values have likewise been multiplied by S . When plotted in this way, in a first approximation, the island length

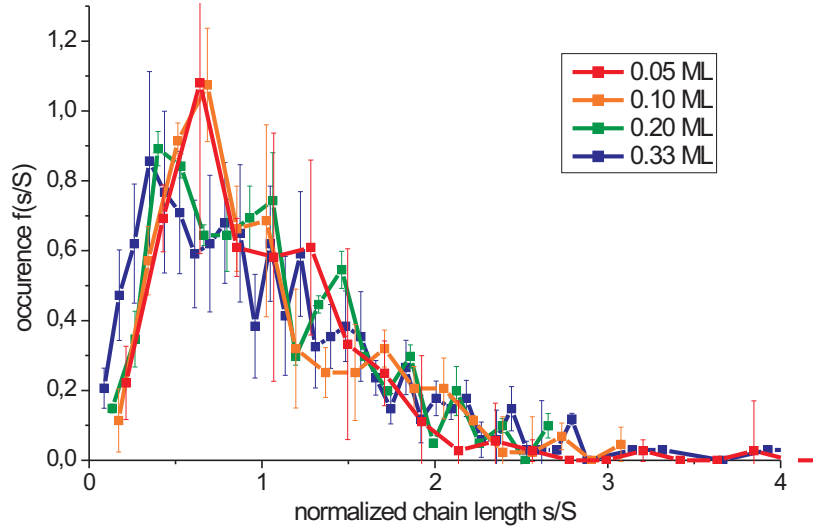


Figure 4.12: Chain length distribution for TMA at different coverage. The curves list the occurrence of chains of size s , where s is the number of TMA molecules in the chain. The curves have been normalized in the abscissa by division and in the ordinate by multiplication with the average chain size S for each coverage. A full surface coverage in the MOCC-S phase is obtained for about 0.53 ML.

distribution appears to be coverage-independent, i. e. the curves for all plotted coverages fall on a uniform curve. A closer inspection reveals, that especially the distributions at low coverage (0.05 ML and 0.10 ML) have a shape showing one maximum at about ($s/S=0.65$). For higher coverages, this maximum splits into two. One should remember that a full surface coverage in the MOCC-S phase is reached at about 0.53 ML. The curves at 0.20 ML and at 0.33 ML thus represent values of significant coverage (see also the images in Figure 4.10) where single chains cannot be considered independent any more but coalescence phenomena start to appear [49].

Theoretical models exist that try to describe such a length distribution [49, 138, 139]. Figure 4.13a shows a simulated distribution for irreversible 1D growth [139], the curve for reversible 1D growth within such a model is expected to be not significantly different if no other effects are assumed [140, 141]. For these models, the existence of a universal curve has been proven. The underlying model of this distribution assumes that each island has a capture zone which extends half way to the neighboring islands (see Figure

4.13b). All particles deposited in this area either attach to the existing island or nucleate as new islands. The formation of a new island happens exactly then when two single particles (monomers) meet (see Figure 4.13c) [138, 139].

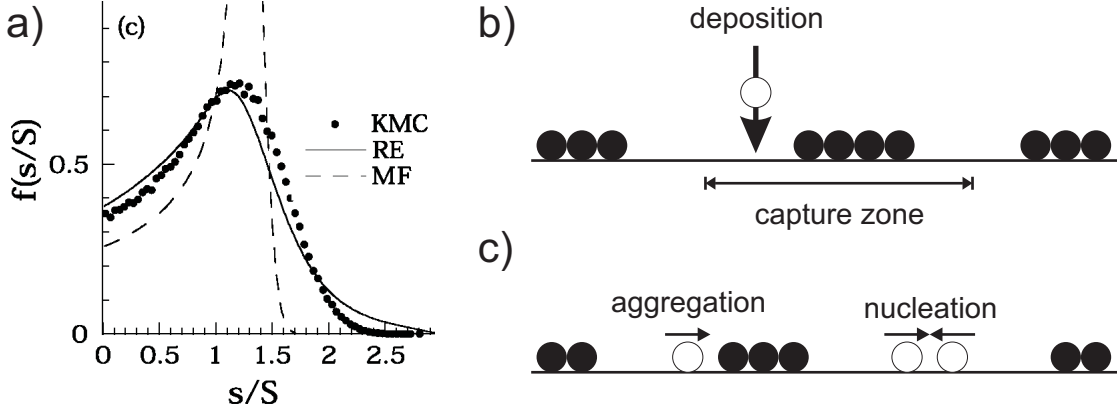


Figure 4.13: Theoretical model for irreversible 1D growth: a) calculated chain length distribution using kinetic Monte Carlo (KMC), rate equation (RE) or mean field (MF) calculations. b) Islands grow by capturing particles deposited in their capture zone which extends half way to the next island, c) aggregation to existing islands and nucleation of new islands [139].

A typical result of many models is that the distribution has a single maximum. This originates in the first growth stages where many nucleation processes occur that create islands of the minimum size $s=2$ (dimers). In the later growth stages, these islands grow uniformly in size, as the size of their capture zone is constant (as long as no further nucleation occurs in between). As a consequence, the maxima of the theoretical distributions are always at the average chain length or even above that ($s/S \geq 1$) [140].

In comparison to this theory we first note, that the coverage independence is also found in our experiments. Also, one maximum per curve exists for the low coverage curves. A possibility to explain that in our case this maximum splits up at higher coverage is coalescence [140]. This describes the joining of chains to larger chains having on average about double the size as before. This effect may explain the appearance of a second peak at higher s values. Coalescence also increases the average island size S which, by means of the employed normalization, shifts the whole distribution to lower (s/S) values. The leftmost peak of the high coverage curves can thus be ascribed to the shifted original peak, the second peak at higher (s/S) to coalescence.

While the peak splitting at high coverage can be explained, a strong disagreement to the theoretical model exists for the position of the maxima of the low coverage curves

which, as stated above, is at about ($s/S=0.65$). Due to this difference in the position of the maxima, the growth of the MOCC-S chains cannot be described with the existing models and we assume that other mechanisms underly the growth of the presented chains. In principle, any mechanisms preferring long chains at all coverage would shift the average chain length S up and at the same time reduce (s/S). Ostwald ripening is such a possible effect [49, 142, 143] for which large chains grow to minimize boundary energy. As we see detachment from chains by STM at room temperature, we can conclude that in principle such a process is possible and that the island growth is not fully irreversible. But from a chain analysis just after deposition we have no evidence for the existence of a non-ripened phase. Also, annealing should be expected to speed up such a ripening process. For this again, we do not have evidence. Instead, the distribution seems to be linked to the growth mode itself. No theoretical explanation has thus been found so far for the underlying growth mode.

From the fact that long chains exist in significant numbers, we can at least conclude that the chains can grow without apparent length limitations. This signifies that no relevant strain is present inside the chains which would preferentially terminate the island growth after a certain maximum length (see also the discussion on stress in chain growth in section 6.1.5).

4.3 MOCC-S: Analysis of the Cu-TMA-Cu-chains

As we have shown above, the anisotropic structure of the Cu(110) surface templates the growth of single metal-organic coordination chains (MOCC-S). In order to be able to extend this recipe for the creation of other nanostructures, a detailed understanding of the structure and of the interactions between the molecules, the adatoms and the surface has to be reached. In a combined approach, STM, LEED, DFT and IR have been used for this analysis.

4.3.1 STM and LEED analysis

In Figure 4.14 representative high-resolution STM images of the MOCC-S are shown. In order to determine their detailed structure, the periodicity of the Cu-TMA-chains was

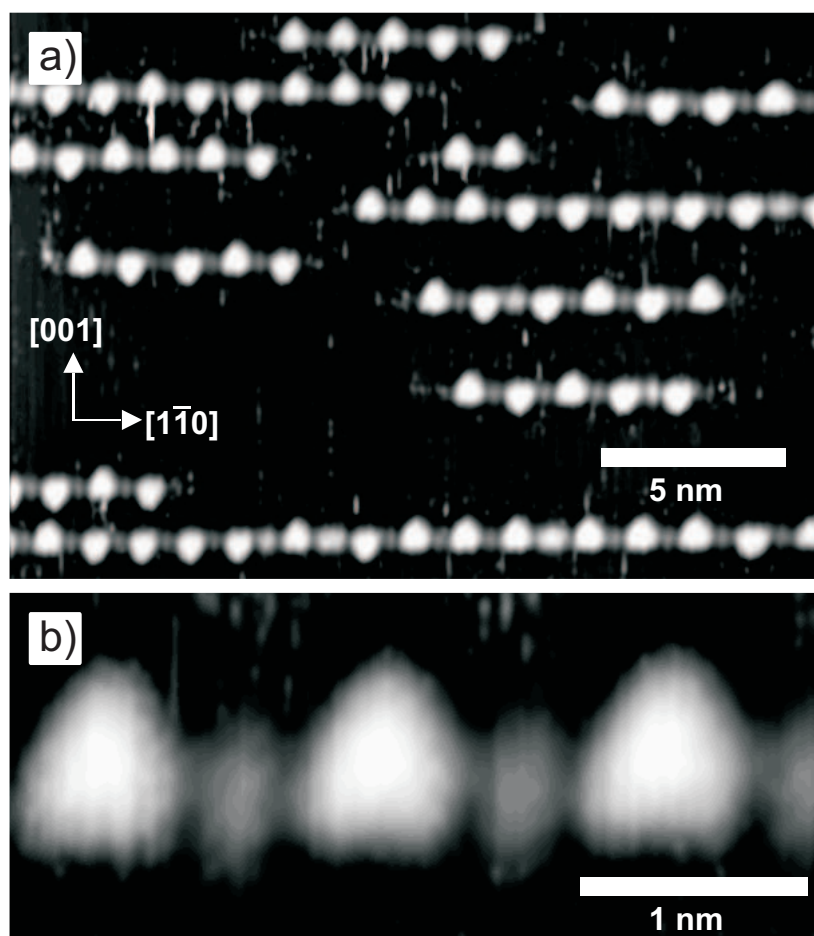


Figure 4.14: Representative STM images of the annealed single chain MOCC-structure of TMA/Cu(110) (MOCC-S).

measured with respect to the underlying Cu-lattice. For this task, the STM was precisely calibrated with respect to images showing atomic resolution of the substrate, and only drift free images were used. The resulting periodicity of the MOCC-S was measured to be $(12.69 \pm 0.15) \text{ \AA}$, which corresponds to (4.96 ± 0.06) – i. e. five – Cu-lattice spacings in the $[1\bar{1}0]$ direction of Cu. This periodicity was experimentally confirmed by LEED measurements showing a clear $5\times$ periodicity of the overlayer (Figure 4.15a).

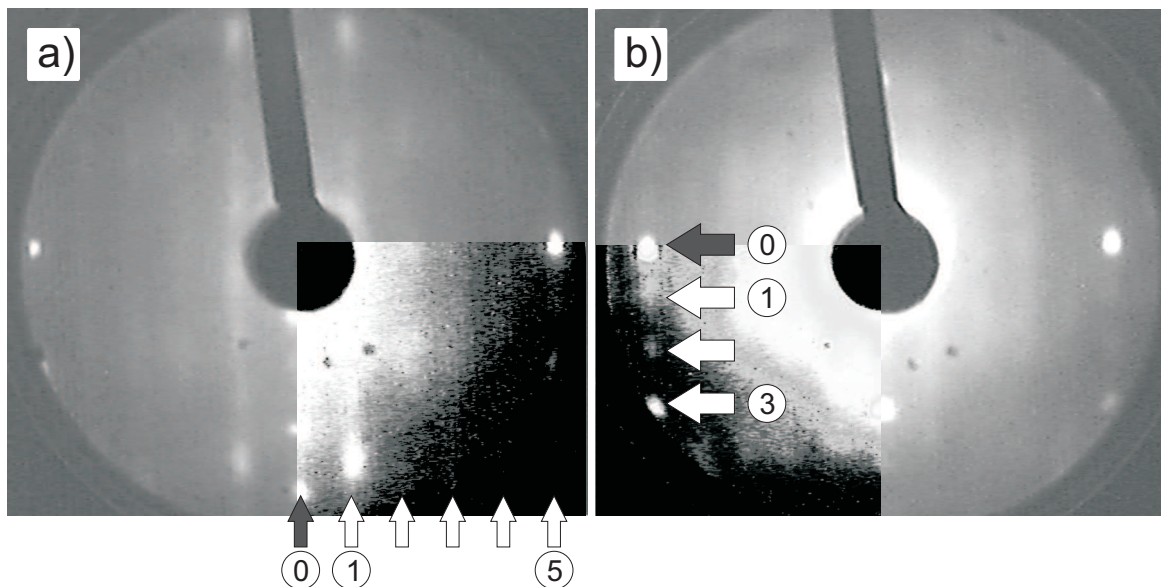


Figure 4.15: LEED patterns of the MOCC-S structure. One quarter of the images has been contrast enhanced to show the weak features more clearly in the printout. a) Low coverage, 58 eV, showing a $5\times$ periodicity along $[1\bar{1}0]$: the horizontal distance between the overlayer spots 0 and 1 is one fifth of the horizontal distance between 0 and 5. b) Close to full surface coverage of MOCC-S, 75 eV, $5\times$ periodicity along $[1\bar{1}0]$ as before. Spots in the vertical direction correspond to a $a \times 3$ periodicity along $[001]$.

It should be noted, that the $5\times$ periodicity is by far the most frequent (more than 77% of all cases) but also other TMA-TMA distances exist. A periodicity of six Cu-lattice spacings is sometimes found as a kind of dislocation for about 17% of the TMA-TMA distances, and in less than about 3% of all cases even longer periodicities (of 7 and more) are observed. These longer spacings can directly be explained by additional Cu atoms in between the TMAs. In very few cases (3% of the chain segments) a periodicity of 4 is found (see also the discussion in section 5.2.1).

With increasing TMA coverage, the chain density is increased but the chains always stay at a minimum distance of three 3 Cu lattice spacings along the $[001]$ substrate

direction. The whole structure can thus be described as a (5×3) superstructure. The LEED pattern for a surface nearly fully covered with MOCC-S is shown in Figure 4.15b. The spots of the $\times 3$ periodicity are much weaker than those of the in-chain periodicity as ordering is less pronounced in this direction. The appearance of the $\times 3$ periodicity along $[001]$ in the LEED measurement was used as one of two reference points to roughly calibrate the flux of TMA on the setup comprising IR and LEED relative to the STM measurements obtained at the STM setup.

A real (5×3) periodicity would imply that all TMAs point in the same direction. Actually, this is not the case, as can be seen from the STM images. Within a chain, the third functional group of each TMA molecule (its “tip”) points up or down without any recognizable regularity. In order to quantitatively proof this arbitrary behavior and to furthermore show that there does not exist any difference between neighboring TMA which are aligned parallel or antiparallel, we have performed a statistical analysis of the STM data. The results are summarized in Table 4.2.

	coverage (ML)	counted TMAs	% up	% down	% parallel	% anti- parallel
MOCC-S	0.08	471	55,6%	44,4%	52,7%	47,3%
MOCC-S	0.22	1407	48,0%	52,0%	47,7%	52,3%
MOCC-S	0.38	1507	48,8%	51,2%	55,8%	44,2%
MOCC-S & T	0.64	1174	48,6%	51,4%	71,1%	28,9%

Table 4.2: Statistical analysis of the TMA orientation. No preference is observed for pointing in $\pm [001]$ as expected from symmetry arguments. Also, no preferential relative parallel or antiparallel orientation was observed for neighboring TMAs within a chain (MOCC-S only). For the discussion of the mixed phase MOCC-S & T, see section 4.4.

As can clearly be seen, no preferential up or down orientation was found for individual TMAs, as was expected from the symmetry of the substrate. Moreover, by analyzing the relative orientation of neighboring TMA molecules, no correlation was found. Neither parallel nor antiparallel alignment of neighboring TMA is favored in MOCC-S as can be seen in the rightmost column of Table 4.2. Nevertheless, a preferred parallel orientation exists in the transition regime between MOCC-S and MOCC-D as will be further discussed in section 4.4.2. We will use this statistical information here for some considerations that help in extracting an adsorption model from the experiment. Afterwards this model will be tested by a DFT analysis (see section 4.3.2).

Let us consider first the position of the TMAs. Since no preferential up or down orientation and no preferential parallel or antiparallel configuration is found, the configurations must be degenerate in energy and we can safely assume that all TMA molecules sit on equivalent substrate sites. This has implications for the position of the Cu protrusion as well. A position in the middle between two antiparallel TMAs must be a position on a high-symmetry line (a mirror line) in the $[1\bar{1}0]$ -chain-direction of the substrate. This mirror line can be either the line connecting the hollow and long-bridge sites, h and lb , line I in Figure 4.16, or the line connecting the top and short-bridge sites, t and sb , line II in Figure 4.16. A Cu-protrusion between two parallel TMAs on the other hand must - again for mirror symmetry reasons be located on a high-symmetry line along the direction perpendicular to the chain (along $[001]$) (line III or line IV in Figure 4.16).

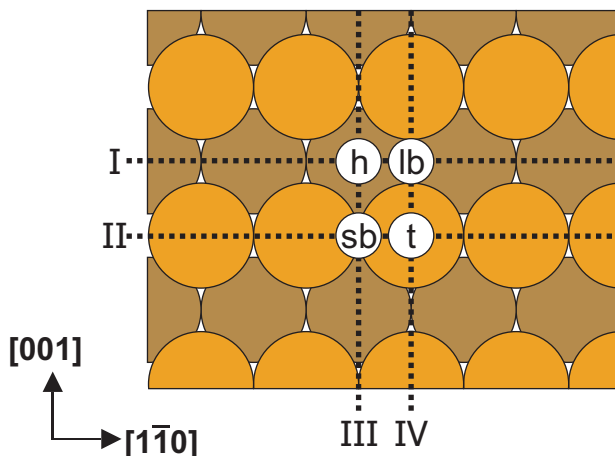


Figure 4.16: Definition of the high symmetry sites on Cu(110): h : hollow, lb : long bridge, sb : short bridge, t : top. Lines I-IV: high symmetry lines of the substrate: line I connecting h and lb (trough), line II connecting t and sb (row), line III connecting h and sb , and line IV connecting t and lb .

As parallel and antiparallel configuration are statistically equally often encountered, the sites for the Cu-protrusions in both configurations must be energetically equivalent. It is then natural to assume that all Cu-protrusions are located on equivalent sites no matter if located between parallel or antiparallel TMAs. Combining the symmetry arguments for both configurations, one can then conclude that the Cu-protrusions are located on one of the intersections of the four high symmetry lines I-IV in Figure 4.16, which are the four high symmetry sites: h , t , sb and lb . Using the known (5×3) periodicity one can then furthermore conclude that also all the TMA molecule are located on

one of the high-symmetry lines in the [001] direction (line III or line IV in Figure 4.16, which is also expected from their own symmetry). We have thus reduced the possible adhesion positions to a few high symmetry points.

A direct experimental determination of the adhesion site can, in principle, be drawn from STM topographies that show a contemporary atomic resolution of the substrate and a molecular one of the chains. This was obtained only under particular tip and scanning conditions for this system. Furthermore, it is well known in the literature, that STM can be misleading in absolutely determining the position of atomic sites, e. g. in deriving which site is a hollow and which one is a top. As the STM measures electronic densities and *not* topography, the question which position is seen higher than another depends on a number of influences, topography being just one of them. The case in which - due to a certain electronic tip state - the tunnelling current is higher above a hollow site than above a top site and in which the measured STM image is seemingly “inverted” has been reported for various substrates (see section 2.1.1 and [62–64]). To avoid this inversion effect, we have used a different method to determine the adhesion sites of the TMA molecule and of the Cu protrusion.

For the position of the chain relative to the [001]-direction of Cu, tip manipulation experiments were performed on MOCC-S-structures cooled to 100 K. While measuring at normal scanning conditions (about -1 V, 1 nA), the bias voltage was strongly decreased to -0.15 V and the current set point was raised as high as 50 nA at specific positions. By this we decreased the tunnelling resistance to 3 M Ω and moved the tip very close to the surface. We continued to scan on a line¹ which was perpendicular to a chain and centered on a TMA molecule inside the chain. By this we were able to move individual TMA molecules of the chain, leaving behind the neighboring Cu adatoms and the rest of the chain (see Figure 4.17). The displacement was confirmed by switching back to normal scanning conditions and taking a full image.

The process was iterated, and after successively removing the TMA molecules of a chain, we were left with 1D-Cu-islands, consisting of three to six Cu atoms in a row. Cu atoms in a Cu chain can naturally be expected to be located upon hollow sites of the substrate. Having thus clearly determined the troughs (line I in Figure 4.16), the positions of neighboring TMA and Cu were deduced using images showing both 1D Cu islands and MOCC-S (see Figure 4.17). As there is no resolution of the individual atoms

¹In the STM software this is achieved by defining a rectangle with one very short side.

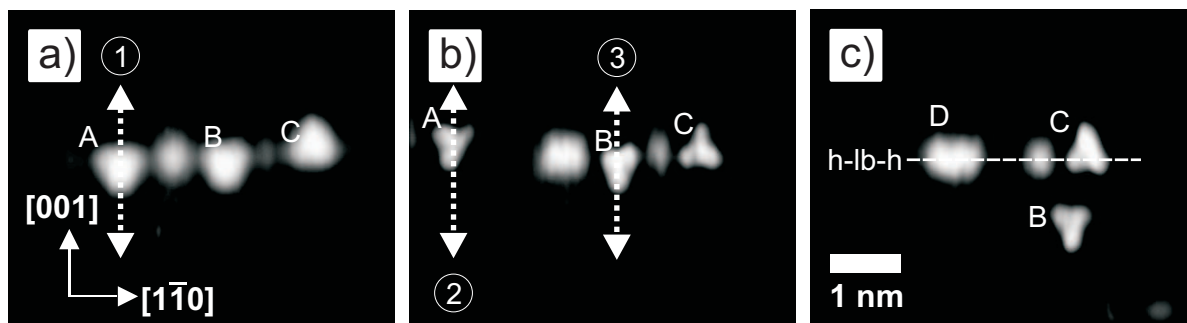


Figure 4.17: Example for Low-Temperature Manipulation. a) A chain of three TMA molecules A, B, and C with a distance of 6 Cu lattice spacings between A and B (including 1 extra Cu adatom) and of 5 between B and C. Low resistance scanning for manipulation were applied along the line 1 (back and forth). After switching back to normal scan conditions A has moved. b) Two further manipulations at 2 and 3 move A out of the image and displace B. This creates the Cu-island D which can be used to identify the position of C and its attached Cu adatom relative along the $[1\bar{1}0]$ direction. Different imaging conditions arise from tip switches during manipulation or scanning.

in a Cu chain for electronic reasons [144], their position could only be determined to be *h* of *lb* for Cu and *t* or *sb* for the phenyl ring of TMA.

For determining the position in the direction of the chains the Cu(110)-(2×1)-O stripe pattern [52, 145] was employed. This pattern consists of stripes along the $[001]$ -direction and forms on Cu(110) upon partial coverage with oxygen, as will be explained in more detail in section 7.1. The deposition of TMA onto this substrate results in the formation of MOCC-S in the wide Cu areas between the Cu-O stripes for small oxygen-coverage. The adhesion geometry of the Cu-O stripes is well known [52, 145] and consists of chains of alternating Cu and oxygen atoms running along every second $[001]$ row, i. e. vertical to the $[1\bar{1}0]$ troughs. This structure can thus be used to determine the absolute position of Cu protrusions and TMA molecules along $[1\bar{1}0]$. TMA molecules far from the Cu-O stripes were measured, in order to avoid localized interactions between the Cu-O stripes and molecules. It is important to note, that any influence of inversion is evaded by this approach as the periodicity of the Cu-O stripes is double the periodicity of the Cu-lattice along the $[001]$ -direction. Therefore, Cu-O stripes and Cu-O troughs are both upon the same sites of the Cu-lattice (line III in Figure 4.16) and it does not matter which one is seen as stripes and which as troughs. We thus concluded that the Cu-protrusion is located either on *lb* or on *t* and the TMA phenyl ring center either on *sb* or on *h*.

Finally, the results of both approaches were combined. The only possibility left was the TMA being located with its central phenyl ring above the short-bridge site (*sb*) of the substrate and the center of the Cu-protrusion on the long-bridge site (*lb*).

The fact that the Cu protrusion should be placed on a long-bridge site is surprising as one might expect any Cu adatom to sit in a hollow site *h* where it is fivefold coordinated instead of fourfold. Also the measured periodicity of $5 \times (12.8 \text{ \AA})$ is somewhat surprising, as the length of a TMA-molecule is only about 8.1 \AA (in gas phase [105, 146]). When measuring the size of the TMA using STM in images as shown in Figure 4.14, this size is confirmed. One TMA would thus just occupy about three Cu-lattice spacings along the $[\bar{1}\bar{1}0]$ -direction, while the Cu protrusion appears as a relatively large spot in the images. Furthermore, the estimated bond length between the Cu-adatom and the oxygen atoms of the carboxylate groups would then be $\approx 2.8 \text{ \AA}$, which is a relatively large value in comparison to the typical bond length of $1.9\text{-}2.2 \text{ \AA}$, reported in literature [147]. In order to clear up the real geometry underlying this structure, other methods are necessary and DFT calculations are ideally suited for solving this problem.

4.3.2 Theory

The theoretical investigations using density functional theory (DFT) calculations were performed by our collaboration partners Guido Fratesi, Stefano Fabris, Stefano de Gironcoli, and Stefano Baroni at DEMOCRITOS and SISSA in Trieste, Italy. The results of these studies will be summarized here.

The DFT calculations were carried out in the generalized gradient approximation (GGA) of Perdew-Burke-Ernzerhof [148] in the pseudopotential plane-wave framework (plane wave cutoff of 326.4 eV) with ultra-soft pseudopotentials [149] using the PWscf simulation package [150]. A simplified 3-layer slab model was used for the Cu(110) surface. While the upper layer was relaxed, the distance between the other layers was kept fixed at the bulk value. Cu adatoms and deprotonated TMA molecules were positioned on the upper surface layer. Structural relaxation was carried out according to the Hellmann-Feynman forces. Using the relaxed atomic structure, the ground state energy and electron density was determined. This electron density was then used to analyze the localized density of states (LDOS) by angular resolved projection on spheres centered at the atomic positions. The LDOS was furthermore used to create simulated STM images by the Tersoff-Hamann method [151] of spatially resolved integration of the DOS

in energy from a bias potential (-1.0 eV) to the Fermi energy (see also section 2.2.3 for an overview of the DFT technique).

At first, all possible adhesion positions for the individual deprotonated TMA and Cu were compared. It turned out that the TMA indeed favors the *sb* site as position for the center of the phenyl ring, while the Cu - not surprisingly - favors the *h* site. The TMA forms a strong binding of 8.0 eV with the surface.

For modelling the chain, a (TMA-Cu)_n geometry was first tried. In best possible adhesion geometry the TMA is on an a position between *sb* and *h*, closer to *sb*. Although the simulated STM images would in principle fit to the experimental data, the Cu adatom is not stable on *lb* in between two TMA. This unstable configuration is shown in Figure 4.18a. The Cu atom would easily further relax into one of the *h* sites of the substrate being thus closer to one of the TMAs, thereby further lowering the total energy by 0.8 eV. As this would either mean to break up the chain or to relax into a 4× periodicity (4.18b and f) which is experimentally not observed, this structure can be ruled out.

The lowest energy structure is indeed formed by a (Cu-TMA-Cu)_n geometry. This is a structure in which two Cu adatoms are placed between neighboring TMAs (see Figure 4.18c). The Cu dimer fills both *h* sites and provides a much better bonding. This structure with two Cu-adatoms in *h* and TMA in a position between *sb* and *h* (closer to *sb*) is the lowest energy 5× configuration and is preferred over a 4× periodicity by further 0.4 eV². The Cu-carboxylate bond length is 2.02 Å, in accordance with values reported in [147]. Furthermore, as can be seen from Figure 4.18g, the simulated STM image of this structure shows only one single spot for the two Cu adatoms. This is in perfect agreement with the STM observation. Finally, the apparent heights obtained from the simulated STM image of 170 pm for TMA and 90 pm for Cu are in very good agreement with the STM measurements of 140±30 pm and 75±20 pm, respectively.

The DFT analysis of this (Cu-TMA-Cu)_n-structure further shows that the TMA is located 1.14 Å above the outermost Cu layer and that its carboxylate groups bend towards the surface by 0.69 Å. The two carboxylate groups facing the Cu adatoms bind to the Cu adatoms with only one of their oxygen atoms (“unidentate” bond) while the other oxygen atom binds to the surface in an almost on-top position. In order to form the two Cu-bonds, the carboxylate groups are significantly twisted from a flat geometry as can be seen from figure 4.18d.

²For this calculation the bulk cohesive energy of Cu had to be calculated. This is discussed in more detail in section 5.

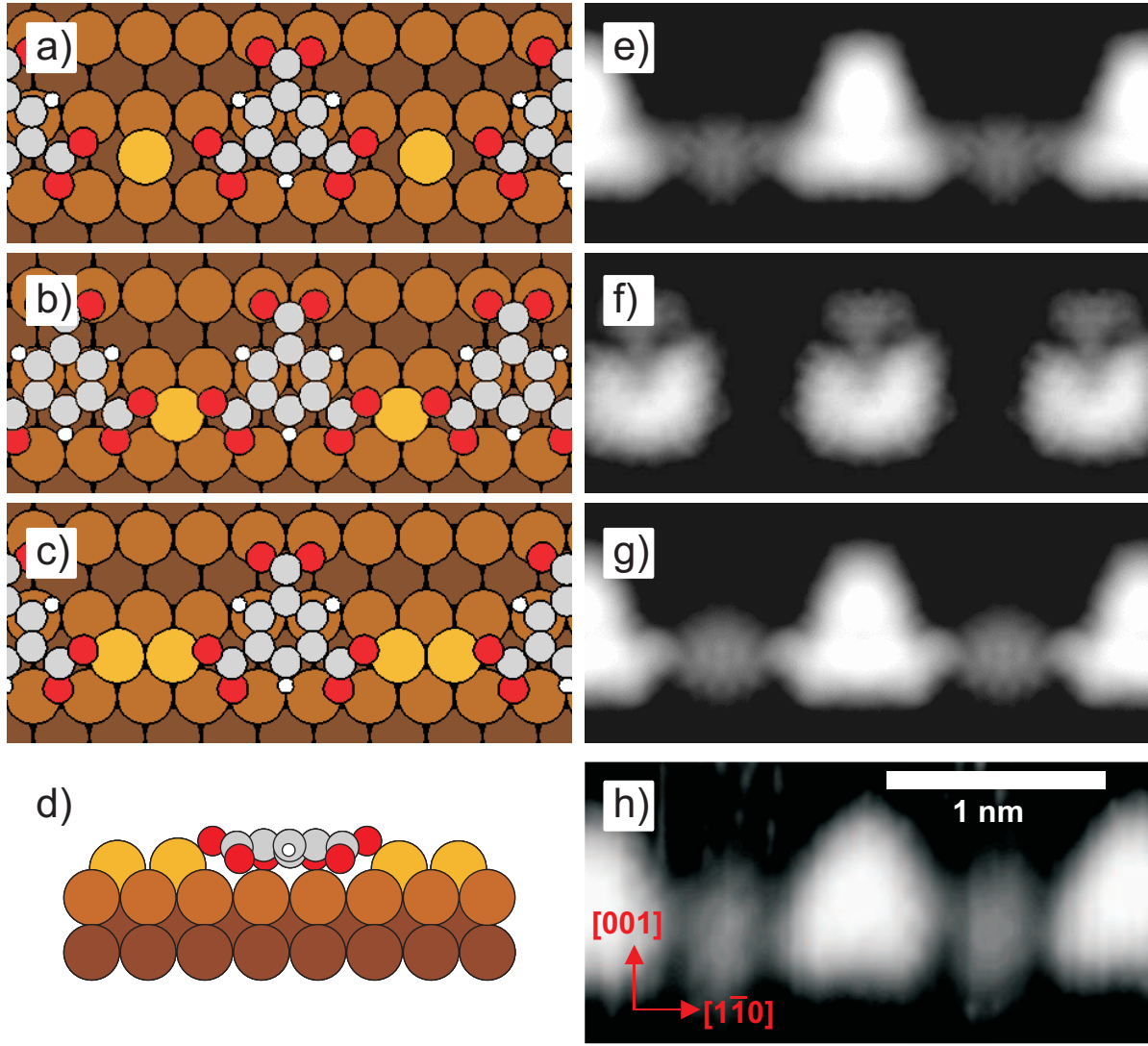


Figure 4.18: DFT results for different possible geometries for MOCC-S: a)-c) fully relaxed atom configurations in top view; d) side view of configuration c); e)-g) simulated STM images; h) experimental image. a) and e) (5×3) geometry with one adatom, energetically not stable; b) and f) (4×3) configuration, experimentally not observed; c), d) and g) Cu dimer, (5×3) configuration, lowest energy structure.

The IR spectra for an as deposited MOCC-S were shown and discussed in section 4.2.4. From the fact, that the asymmetric carboxylate mode is seen with weak intensity one can conclude that the carboxylate groups are not perfectly flat on the surface as they would otherwise not show any effective signal in IR. This result is in good agreement with the DFT result of the carboxylate groups bending to the substrate which can also be seen from Figure 4.18d.

DFT also allows to look beyond the geometry and investigate the electronic configu-

ration. Analyzing the charge transfer is complicated as not only two but three different partners (TMA, Cu adatoms, Cu surface) are involved. Only final charge filling levels can be analyzed and not the charge flux. With respect to a neutral Cu atom, the electronic occupation of a Cu adatom is reduced by 0.4 e, half of the reduction in the *s*-states and half in the *d*-states. The electronic structure of the (Cu-TMA-Cu)_{*n*}-MOCC-S will be discussed in detail in section 4.3.3.

4.3.3 Analysis of the electronic structure

To experimentally analyze the electronic structure of the MOCC-S we have used scanning tunnelling spectroscopy (STS, see section 2.1.2). STS measurements were carried out at low coverage (0.1 ML and less) of MOCC-S to allow tip preparation and testing on clean substrate areas. Test measurements at higher coverage turned out to be less reliable concerning the tip states. The STS measurements were performed at room temperature according to the procedures outlined in section 2.4.2.

The STM tip was prepared to show a flat and featureless curve in the differential conductance $\partial I/\partial V$. As a reference for the $\partial I/\partial V$ of the clean substrate, measurements of the same surface on a different STM at a temperature of around 5 K were used [152]. STS spectra were taken alternatingly on the clean substrate (background spectra) and on-top of the TMA molecules, with the tip being centered as well as possible on the middle of the phenyl ring. Spectra on molecules were only taken as long as no significant change in the background spectra was observed that were measured far from the molecules (more than 1 nm away) to avoid any influence of the molecules.

While the actual Cu background spectrum was found to depend on the actual tip properties, the difference of the molecular and the background spectrum was found to be relatively independent of the tip structure. Qualitatively similar final spectra were indeed obtained after background subtraction with tips showing different small features on the Cu background (while all being in general flat). This observation is in agreement with theory (see section 2.1.2) and was seen as a confirmation of the reliability of the obtained spectra. It was on the contrary not possible to measure reliable spectra of the Cu adatoms. This can be caused either by the experimental problem of reliably placing the tip above the Cu-adatoms when manually positioning the spectra in the STM software or by the electronic structure of the Cu-adatoms, especially concerning the angular components as will be explained below. The analysis will be thus limited

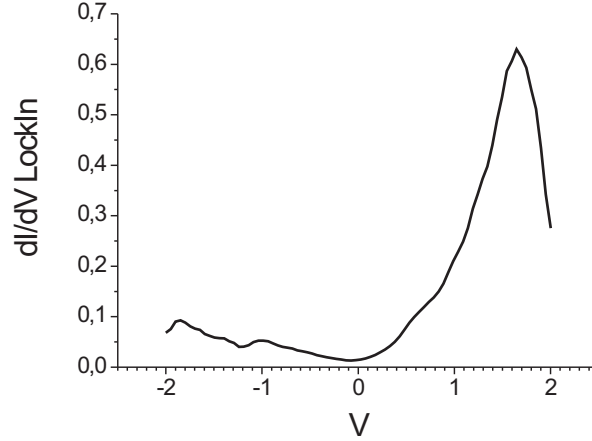


Figure 4.19: *ST-Spectroscopy of TMA in MOCC-S. The spectrum is averaged over 24 individual spectra and the Cu(110) surface signal (averaged over 55 individual spectra) has been subtracted. The spectrum is smoothed according to next-neighbor averaging.*

to the investigation of the TMA molecule. The background corrected spectrum of the TMA can be seen in Figures 4.19.

The TMA spectrum in Figure 4.19 is almost featureless below the Fermi level (located at 0 V), while showing a strong rise above the Fermi energy. Its main feature is a peak centered at 1.65 V with a width of about 0.6 eV. The small signatures in the occupied states (negative voltages) start from -0.8 V with small peaks at -1.0 V and -1.9 V. From other spectra obtained with different tip configurations these peaks within the occupied states are sometimes more pronounced but the occurrence within the data is not often enough to reliably claim that these peaks should be on average more pronounced. While the significance of these small features is thus not fully clear, the main peak is reproduced throughout the experiments and therefore for sure connected to a real electronic structure.

The spectrum in Figure 4.19 can be compared to the localized density of states (LDOS) as calculated by DFT. However, as outlined in sections 2.1.2 and 2.2.3, this comparison is limited for two reasons: STS does not directly show the LDOS but a spectrum which, only under the assumption of a flat tip-DOS, is proportional to the LDOS of the sample. Moreover the spectrum is especially reliable above the Fermi level, i. e. for empty sample states (see section 2.1.2 and [68]), whereas DFT is in principle only valid for filled electronic states below the Fermi level (see section 2.2.3). Nevertheless,

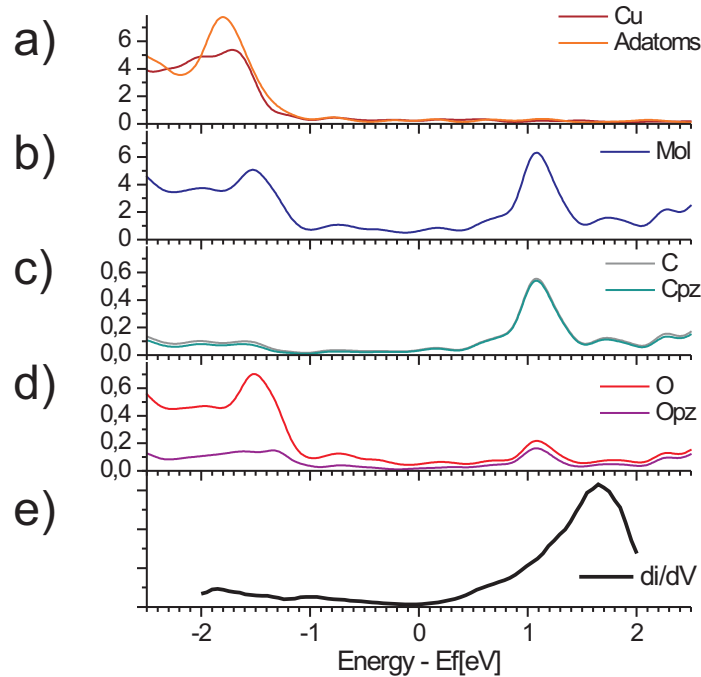


Figure 4.20: Density of States calculated from the fully relaxed DFT structure of MOCC-S. Local projected DOS of a) all Cu atoms (brown) and Cu-adatoms (orange); b) all atoms within the TMA molecule; c) the carbon atoms in TMA – the total C LDOS (grey) and the C- p_z LDOS (green), the spectra are almost identical; d) the oxygen atoms in the TMA – the full oxygen LDOS is shown in red and the O- p_z -LDOS in purple; e) the measured STS curve. All calculated LDOS curves have been broadened by a Gauss smearing of 100 meV.

such a comparisons has been repeatedly and successfully made in the literature and will also be given here [144, 153–155]. In Figure 4.20a-d the angularly resolved projected density of states is shown. In a rough comparison it can be seen that the distance of the peaks above and below the Fermi level is about 0.55 eV smaller in the DFT results than in the STS data which are again plotted as a reference in Figure 4.20e. This difference is most probably due to the well-known effect of DFT underestimating the gap size [156]. As a comparison we point out that DFT calculations of TMA in vacuum also underestimate the gap in respect to what is determined by Ultraviolet Photoemission Spectroscopy measurements of TMA powder with 3.7 eV instead of 4.0 eV [157]. Assuming as a first approximation that the DFT gap size underestimation just rigidly shifts the states without strong further changes, we can tentatively ascribe the peaks seen in STS to their physical origin by means of the DFT calculations.

The main peak can directly be attributed to the C- p_z states of the molecule with some contribution of the O- p_z states, as can be seen from Figure 4.20. These states are likewise hybridized to the Cu states of the surface. The small features in the STS spectra below the Fermi level may be attributed to oxygen p -states hybridized to the d -states of the adatoms. While the peaks in STS are small and thus the argumentation should not be overstretched, their position fits reasonably well to the spectra a and d in Figure 4.20. Among the oxygen p -states, the p_z -contribution is small, which in turn means, that these states are mainly p_x - and p_y -states, hybridized to d -states of the adatoms. In other words, the main peaks below and above the Fermi level are formed by different angular components. Depending on the electronic structure of the tip, we thus assume that the tunneling probability is enhanced for either the $m = 0$ angular components above or the lateral components below the Fermi level. The fact, that the adatoms are not visible as a clear signal within the STS can thus in principle be explained, as we have tried to prepare the tip always in the same way, which generally creates strong signals of the C- p_z components but only in accidental cases provides strong signals of the states below the Fermi level. Additionally, it should be noted, that independent of the angular components, tunnelling through the C- p_z states is probably facilitated by the spacial orientation of the electron distribution of these states which stick out perpendicular from the planar molecule and are thus always closer to the tip than localized states in the plane of the molecule.

A side result of this investigation is that some of the best resolved STM images seem to depend on a specific tip configuration which is not usable for STS. Spectra acquired in an imaging mode producing highly resolved images typically resulted in a Cu spectrum showing extensive features above the Fermi level while the $\partial I/\partial V$ on the molecules was almost close to zero between -2 V and 2 V except for small peaks. In such a configuration a gap-feature is also observed in z-V-spectroscopies. From these results we expect that a molecule is bound to the end of the STM-tip. This would explain the strong features on the bare Cu spectra, which do not correspond to a metal-to-metal tunnelling but to a tunnelling through a molecule in between. The enhancement of image quality by molecules adsorbed to the tip has been seen several times in the literature [158–161]. Competing tunneling channels might further complicate such a geometry [66].

4.3.4 Final discussion and summary of the MOCC-S structure

We have analyzed this system by means of a series of experimental and theoretical investigation techniques in order to obtain a full description both of its structure and of its electronic properties. STM measurements are able to provide information about the overall geometry showing the chain structure, the two constituting species, as well as the periodicities along the main crystal directions. Nevertheless, by STM alone it is not possible to determine the detailed adhesion structure. DFT and STM turned out, once more, to be highly complementary to each other. We have shown that by feeding the input parameters from STM into DFT calculations, the precise adhesion structure with the Cu dimer can be determined. LEED measurements confirmed the periodicities observed by STM. The deprotonation, which can only be assumed from looking at the STM and DFT results, is confirmed by RAIRS. Also the fully relaxed adhesion geometry as obtained from DFT is confirmed by the RAIRS data. DFT was found to underestimate the gap, but comparisons to STS are still possible and allow to determine the electronic states that are responsible for the bonding. In this sense, all methods together provide a uniform and full picture of the MOCC-S structure, whose main characteristics can be summarized as follows:

Deprotonated TMA molecules are found at room temperature and above. Linear chains are formed in which TMA molecules alternate with Cu dimers with a periodicity of 5 Cu lattice spacings along the $[1\bar{1}0]$ direction. The metal-organic coordination chains can grow without apparent length limitations and fill the whole surface with high regularity. The TMA molecules lie flat on the surface but two carboxylate groups are bent towards the surface to allow bonding of the oxygen atoms to the substrate. The center of the phenyl ring of the TMA is located closer to the *sb* site, while the Cu adatoms sit in *h* sites. The orientation of the third functional group of TMA does not influence the geometrical structure of the chains. The electronic states of TMA (mainly *p*-states) are hybridized with substrate Cu-*d* states, forming the HOMO of the molecule. The LUMO is formed by C-*p_z* states of the phenyl-ring with some additional components through hybridization. The obtained MOCC-S structure shows that it is indeed possible to create 1D-metal-organic chains by using the surface as a template.

4.4 MOCC-D: Cu-TMA-Double chains

As mentioned before, it is possible to increase the coverage of TMA molecules up to the point for which the whole surface is filled with MOCC-S which happens to be at about 0.53 ML. A further coverage increase results in a structural change of the MOCC-S. After a structurally complicated transition regime which we will describe below, a highly ordered full monolayer of MOCC-D is obtained.

4.4.1 The structure of MOCC-D

The structure of the MOCC-D (see Figure 4.21a) is significantly different from that of the MOCC-S. The unit cell comprises two TMA molecules and the in-chain periodicity is reduced from $5\times$ to $4\times$ ($3,96\pm0,15$ as measured from driftfree STM images) while the periodicity perpendicular to the double-chains is four, when measured from one double chain to the next. The (4×4) can also be seen from the LEED image in Figure 4.21b that was taken after annealing to 470 K.

The packing is greatly enhanced in comparison to the MOCC-S since the unit cell now comprises two TMA molecules while having a similar extension. The reduced in-chain periodicity only leaves space for one adatom between the molecules. Starting from highly resolved STM-images (such as shown in Figure 4.21e) and basing on the results obtained for the (5×3) structures discussed above, the DFT model of the (4×4) structure can be constructed straightforwardly. In the lowest energy structure (see Figure 4.21c) TMA is again located with its phenyl ring above the high symmetry line connecting the *sb* and *h* sites (line III in Figure 4.16 on page 54). But in comparison to the MOCC-S structure, TMA has now relaxed into the direction of *h* which results in the dense packing within a double row. The Cu adatom is still located on an *h* site. The simulated STM image agrees well with the experimental one as can be seen from Figure 4.21d and e. When deposition is continued beyond the point of a full monolayer of MOCC-D, the growth of a second layer is observed. STM ceases to be a useful tool to analyze these structures as scanning conditions rapidly worsen beyond 1 ML. A very high annealing of about 500 K allows to lift the second layer off, leaving behind a monolayer of MOCC-D where a few standing molecules are typically still incorporated.

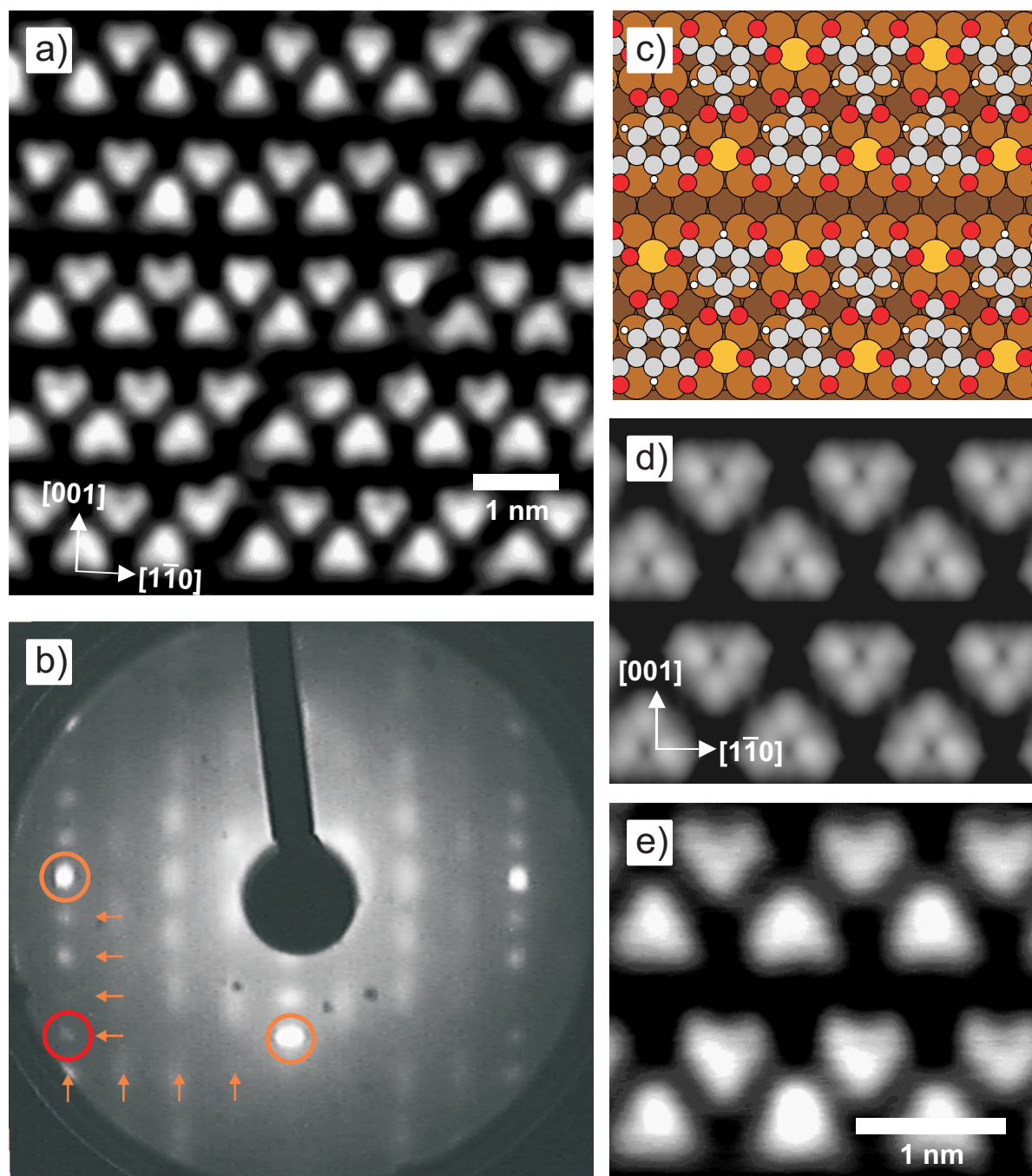


Figure 4.21: a) Representative image of MOCC-D. b) LEED pattern showing a (4×4) adhesion geometry. c)-e) Comparison of: c) fully relaxed lowest energy adhesion structure, d) simulated STM image as obtained from DFT, and e) high resolution STM image.

4.4.2 The transition regime

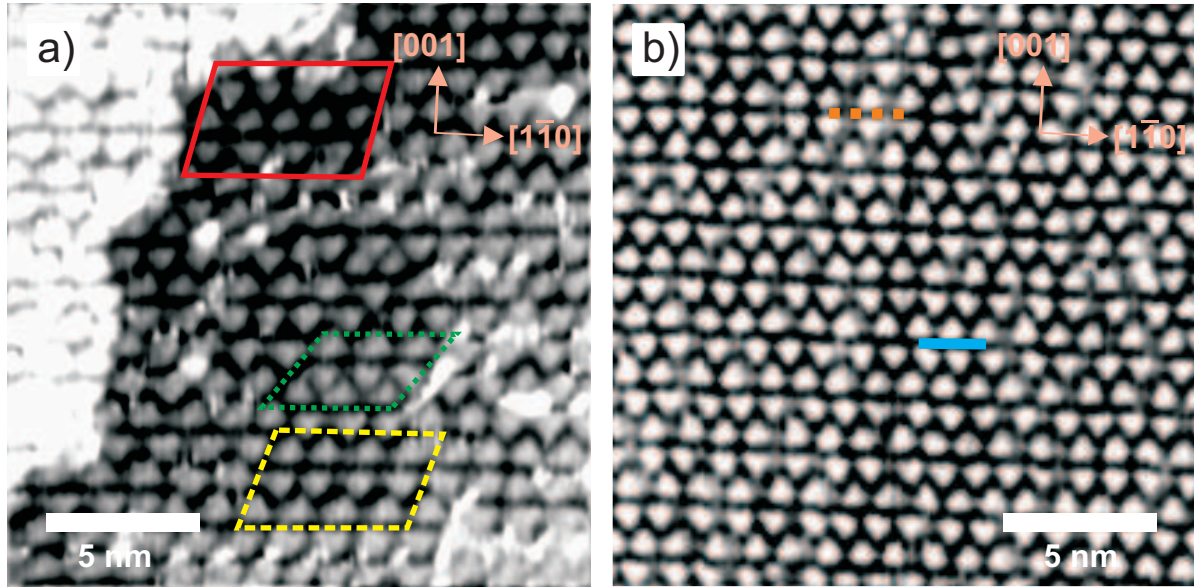


Figure 4.22: Intermediate TMA coverage regime, 0.64 ML TMA coverage. a) Annealed to 380 K: Coexistence of MOCC-S (red, solid), MOCC-T (yellow, dashed) and MOCC-D (green, dotted) and interstitial impurities. b) Annealed to 500 K: MOCC-T in (5×5) domains (orange, dotted) and (4×5) domains (blue solid).

Single chains are always formed below 0.53 ML coverage. Double chains are found at coverage of exactly 1 ML. We will focus now on the coverage regime in between. Without annealing (as deposited at 300 K) no ordered structures are found. Poor scanning conditions are ascribed to loosely bound molecules on top of the first layer which can be moved with the STM tip. After annealing to around 380 K, a partial ordering of the structure is obtained (see Figure 4.22a). A similar result can be reached by leaving the surface at 300 K for about a day. Locally, poorly resolved structures are found with an apparent height of at least 220 pm which can be ascribed to molecules that are still in a virtual second layer but are pinned on molecules or adatoms. Alternatively, this could also be partially upright molecules possibly only bound to the surface by one or two carboxylate groups. For the flat lying molecules, coexistence of several small domains is observed which locally form MOCC-S or MOCC-D as well as intermediate structures. For the intermediate domains in-chain periodicities of $5 \times$ and $4 \times$ are found along $[1\bar{1}0]$. The occurrence of an in-chain periodicity of 4 in LEED for the structures annealed to 380 K was used as a second rough reference point for flux calibration of the IR measurements relative to the STM measurements. The periodicity across the chains is either $\times 3$ as for

MOCC-S or $\times 4$ for two molecules in MOCC-D or $\times 5$ for two molecules which hereafter will be referred to as MOCC-T (for transition). The structure of MOCC-T is similar to that of MOCC-D with the difference, that the chains have not relaxed so closely to each other as in MOCC-D (see Figure 4.22).

A strong annealing to about 500 K is able to increase the ordering and remove the unresolved interstitial molecules either by incorporation or desorption. Extended domains are formed at this temperature. For coverages of about 0.53 ML to 0.6 ML a coexistence of MOCC-S and MOCC-T is found, where the number of MOCC-T increases with coverage. For about 0.6 ML to 0.8 ML only MOCC-T are found which partially have an in chain periodicity of 4 and of 5 (see Figure 4.22b). A further coverage increase creates the (4×4) domains of MOCC-D which coexist with MOCC-T (4×5) domains. The MOCC-D domains again grow with coverage until at 1 ML MOCC-D fill the whole surface.

4.4.3 IR measurements

The IR measurements for a high coverage of TMA/Cu(110) deposited at room temperature can be seen from the spectra d-j in Figure 4.11 on page 46. Strong bands are observed at 754, 914, 1145, 1341, 1367, 1643, 1760 and 3575 cm^{-1} . The 3575 cm^{-1} mode is due to the O-H stretch and the 1760 to the C=O stretch. These correspond to extra molecules being incorporated as acid molecules standing on the surface in an upright position. The peaks of the flat-lying molecules, mainly the 754 peak as well as the weaker 914 are still there showing that the flat-lying species still exists. The mode at 1643 cm^{-1} can be attributed to an asymmetric carboxylate stretch, which is different from the one observed for the single chains at around 1510. It is similar nevertheless to the 1650 mode seen at 85 K (see Figure 4.6). As in that case, one may assume a deprotonated carboxylate group which has not yet found a Cu adatom to bend down and thus creates the vertical component of the stretch. Such a group may be located in the first layer or in a virtual second layer on top of an adatom. Alternatingly, a conformational change for TMA molecules in chains could also result in such a band. It is noteworthy, that even a post-annealing to 470 K does not fully remove the acid components. This probably means that, while all second and higher layers are removed, standing molecules are still left within the first layer in agreement with the STM results. Similar results are obtained for annealing TMA deposited at 250 K as can be seen from the spectra h-k in Figure 4.8

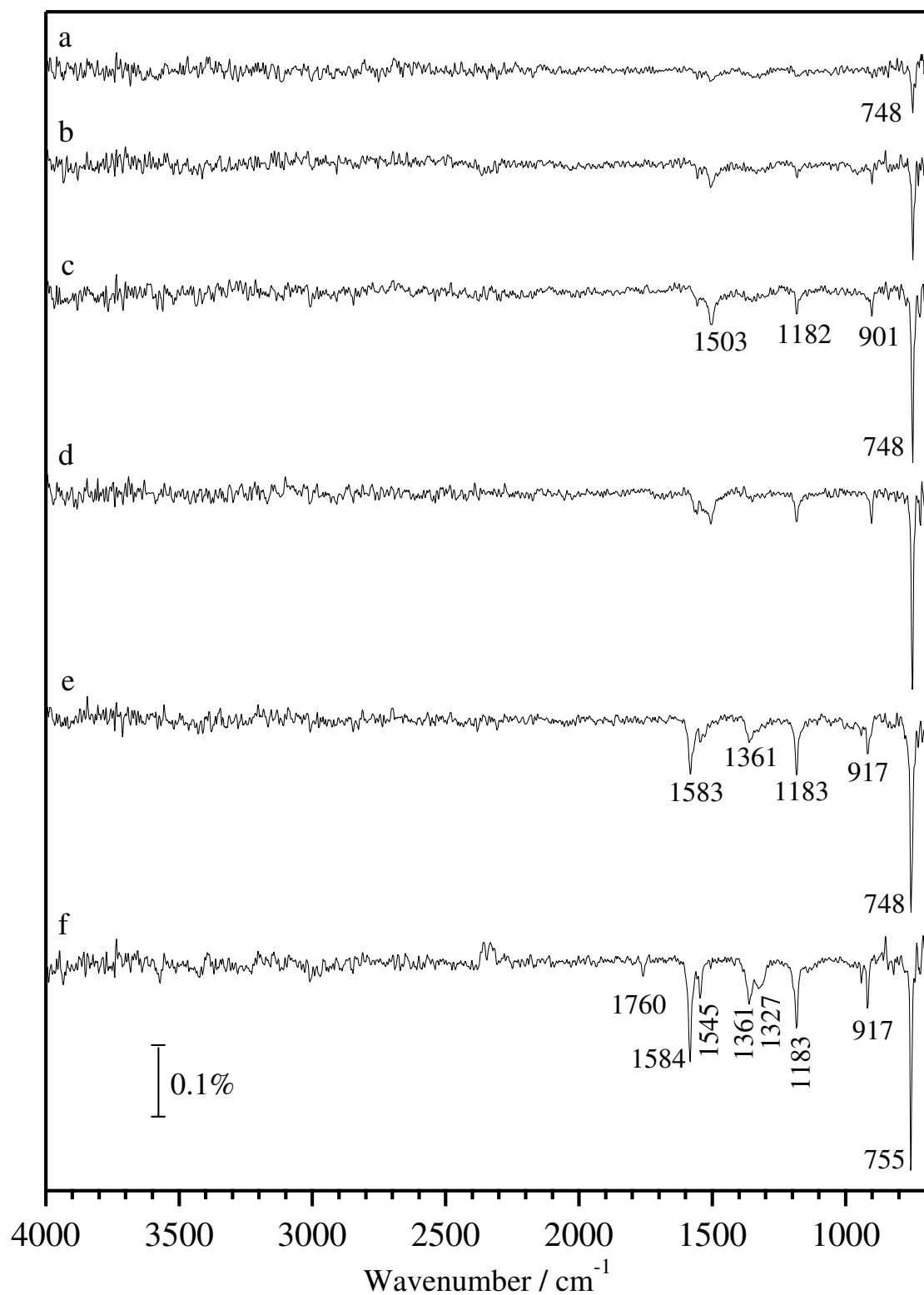


Figure 4.23: IR measurement of TMA adsorbed at 470 K. Series of increasing coverage. Fewer and sharper lines are obtained at this substrate temperature.

on page 42. Here, by annealing, one can visibly follow the reduction of acid components either by desorption of the acid molecules or by deprotonation. Nevertheless, with a maximum annealing temperature of 423 K and probably coming from a much more disordered structure, the finally obtained lines are not as sharp as upon annealing a layer deposited at room temperature as shown in Figure 4.11 on page 46.

For comparison, the IR spectra of an adhesion directly at 470 K is shown in figure 4.23. Here, clear and sharp peaks are visible. For low coverage the known bands of MOCC-S appear which change only slightly at high coverage to a structure which can be fully attributed to MOCC-D according to the LEED and STM analysis presented above. No O-H stretch modes are seen at high wavenumbers and only a faint signal is observed at 1760 for the C=O stretch. Full deprotonation can thus be assumed in agreement to STM and DFT. The bands at 1327 and 1361 are hard to explain in this context. But they are very similar to what was found for the inorganic Cu-TMA polymer forming 2D sheets in 3D supramolecular crystals which exhibit modes at 1350 and 1369 [135]. In general, this supramolecular crystal has a very similar IR structure which underlines that the templated surface MOCN are a real extension of 3D bulk chemistry designs.

4.4.4 About packing and energetics

The analysis of coverage dependent phase formation naturally leads to the question about its driving force. The fact that the MOCC-T and MOCC-D structures only form, when the TMA coverage exceeds the limit of a full layer of MOCC-S, shows that the higher packed phases are not generally energetically favorable. At low coverage, the MOCC-S structure is indeed favorable as was shown by DFT. On the other hand, molecules in a virtual second layer or in non-flat configurations at interstitial sites have for sure a higher energy than molecules either in the MOCC-S, MOCC-T, or MOCC-D structure. Figure 4.24 symbolizes the energy scaling with increasing number N of molecules. At low coverage MOCC-S is the structure with the lowest energy. Upon filling the whole surface with MOCC-S at N_{1max} , extra molecules have to be incorporated in a second layer or at interstitial sites at high energy cost. The overall energy starts to rise fast until it crosses the energy per molecule of MOCC-T. The same situation exists for MOCC-T and MOCC-D. Instead of switching fully from one phase to another, coexistence areas are formed which in this view would correspond to intermediate lines between two phases.

These experimental observations are confirmed by DFT total energy calculations for

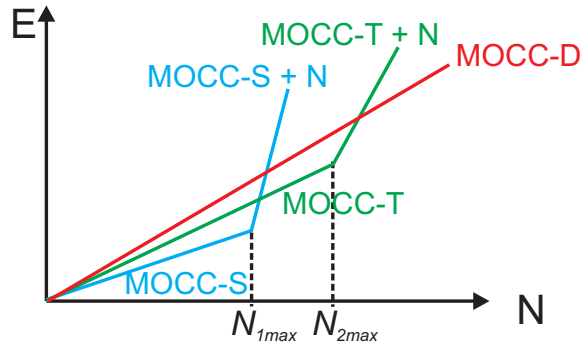


Figure 4.24: Energy scheme for packing molecules in the different phases MOCC-S, MOCC-T, and MOCC-D.

MOCC-S and MOCC-D [156]. The free energy of the MOCC-S is $-0.9(1)$ eV, whereas it is $-1.7(8)$ eV for the double chain MOCC-D. As one TMA is incorporated in every MOCC-S and two in MOCC-D, the energy per TMA molecule is $-0.9(1)$ eV for MOCC-S and $-0.8(9)$ eV for the double chain. At low coverage, where the energy per TMA molecule is maximized, the single chains of MOCC-S are energetically preferred. At high coverage, when space is limited, the free energy per unit cell of the substrate is maximized. As both structures require about the equal amount of space and MOCC-D has nearly double the free energy, it is not surprising that the MOCC-D is favored with -0.11 eV per unit cell of the substrate in comparison to -0.06 eV for the MOCC-S [156].

The observations so far are describing the situation at 500 K at which all molecules and adatoms are free to move into the lowest energy configuration at each given coverage, i. e. for conditions close to thermal equilibrium. From the fact that such nice ordered configurations are not observed at lower temperatures, one can readily conclude that kinetic barriers exist which limit the transition. This is most clearly demonstrated by the fact that leaving the system for one day at 300 K without any annealing can already improve the ordering. The possible causes for these kinetic barriers are: firstly, all molecules have to be deprotonated for being incorporated in the layer. As explained above, this is caused or at least catalyzed by adatoms [124]. On the free surface, adatoms are readily available at 300 K and above [119]. For a surface already covered with MOCC-S only adatoms inside of metal-organic structures exist and their ability to catalyze the reaction might be lower than that of free adatoms. This would imply a preferential nucleation of the next phase around step edges, for which we do not have evidence. On the other hand, extra adatoms for deprotonation might also be supplied directly from

terraces at a higher energy cost than from step edges. Secondly, energy barriers can exist for descending from the second layer to the first layer. This implies to move and flip bound TMAs and to break existing Cu-Cu bonds, specifically when the in-chain-periodicity is changing from five to four. A definite decision about which reason is the important kinetic limiting factor cannot be made here.

Turning these argument around one can definitely conclude that at a temperature of 500 K both TMA and the adatoms are mobile enough to reach the lowest energy configuration. For the adatoms, this is in agreement with the fact that Cu-O stripes can be grown at 450 K, which requires a high adatom mobility at this temperature (see also chapter 7). From the result here, we can furthermore conclude that also the TMA mobility is high enough at 500 K (even within a full covered layer) to reach the equilibrium configuration in timescales of a minute or less.

4.5 TPA on Cu(110)

Having analyzed the structure of TMA on Cu(110), a natural extension is to investigate the adhesion of TPA on the same substrate. As discussed in the introductory section of this chapter, TPA is very similar to TMA with two oppositely positioned carboxylate groups. TPA being a linear molecule, one might expect, that it should be even better suited than TMA for the formation of metal-carboxylate chains. As we will show here, this expectation turns out to be at the same time correct and incomplete.

The growth of TPA on Cu(110) was investigated by D. S. Martin and coworkers by means of RAIRS, LEED and thermal desorption spectroscopy [122]. Using LEED, these authors have seen the formation of a $c(10\times 2)$ superstructure at low coverage and deposition temperatures of 300 K and higher. RAIRS measurements revealed the presence of carboxylate groups oriented parallel to the surface indicating that the $c(10\times 2)$ is composed by flat-lying deprotonated TPA. A detailed insight into the supermolecular structures was nevertheless not reached nor was the origin for the $c(10\times 2)$ superstructure revealed. We have therefore decided to conduct an STM analysis of this system with the goal to link these TPA data with our results for TMA on Cu(110).

TPA was deposited using the parameters outlined in section 2.4.3. For substrate temperatures of 240 K and below unordered patterns were obtained similarly to the TMA deposition. Deposition at 280 K and higher resulted in ordered patterns of high regularity even without any post-annealing. A high temperature annealing did also

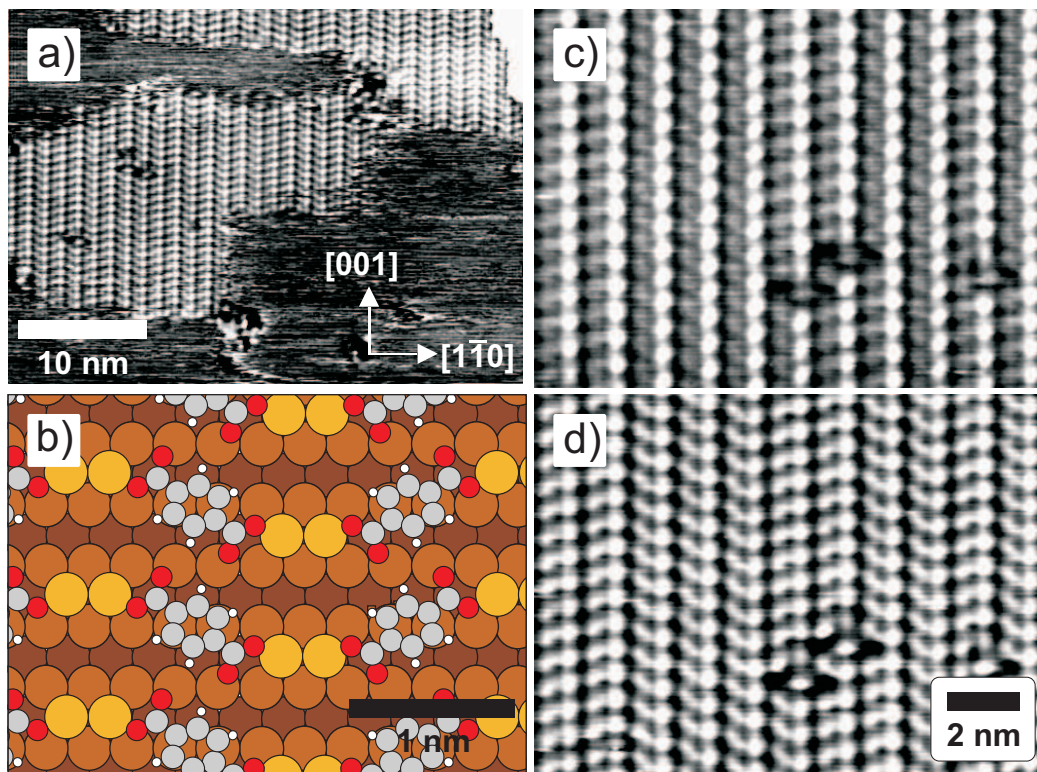


Figure 4.25: Representative STM images of TPA on Cu(110). a) Compact islands formed at low TPA coverage. b) Model of the adhesion structure. c) and d) Consecutive images of the same area showing the tip dependent imaging of the MOCCs.

not change the observed structures, at least for the low coverage regime. 300 K grown structures were used to further characterize the adhesion geometry. Representative STM images of TPA/Cu(110) are shown in Figure 4.25. For low coverage compact islands are formed (see Figure 4.25a) which all have the same internal structure. With increasing coverage the island size grows and a full coverage can be reached, still with the same adhesion structure. Above this limit, TPA starts to show a denser packing into several different phases. Here we will limit the description to the first low coverage phase, as the further structures are beyond the scope of this investigation.

A clearer view of the adsorption geometry is shown in Figure 4.25c and d. It should be noted, that the visual appearance of this structure strongly depends on the scanning parameters, i. e. on the tunnelling bias and current and probably also on the tip geometry. In most scanning conditions it is possible to distinguish two different species within the structure, one rounded and the other elongated. Their apparent height in comparison to the free surface is less than 80 pm (the exact value depending again on the tip condition).

Standing molecules can thus be excluded, the TPA being flat-lying in accordance with RAIRS [122].

As for the case of TMA, the geometric characteristics of the supramolecular arrangement were deduced from driftfree STM images. The periodicity along the $[1\bar{1}0]$ direction is 5 Cu lattice spacings when measured from one round protrusion to the next. In the $[001]$ direction the periodicity is 2. Thus the adhesion structure would be a (5×2) . A close inspection of Figure 4.25c reveals however that only every second round protrusion is on the same $[1\bar{1}0]$ Cu-line while that in between lies on the neighboring line. The effective adhesion structure is thus a $c(10 \times 2)$ as obtained by LEED. Scanning conditions such as those in Figure 4.25d clearly show that the elongated structures within the unit cell are not fully aligned to the $[1\bar{1}0]$ direction but form an angle of $\pm(18 \pm 3)^\circ$. An alternation of up and down tilted protrusions is often observed.

Basing only on these results – even when taking into account the LEED and RAIRS data – a model of the adhesion geometry would be hard to construct. However, the extensive analysis of the TMA/Cu(110) system allows a straightforward construction of a structural model. Similar to the TMA case, one of the observed species can be attributed to a flat-lying fully deprotonated TPA molecule and the other to Cu adatoms. The $5 \times$ adhesion geometry (or its $10 \times$ double equivalent) could be surprising in the TPA context alone, but appears to be quite natural by comparison with the TMA-MOCC-S structure. The rounded protrusions can thus be expected to be likewise formed by a Cu dimer which is located in two adjunct hollow sites of the substrate. The elongated species on the other hand can then be attributed to TPA molecules which are slightly tilted out of the $[1\bar{1}0]$ direction. This structure was again used as an input for DFT calculations that result in the fully relaxed structure shown in Figure 4.25b. It was found that TPA indeed rotates out of the $[1\bar{1}0]$ direction in order to form monodentate coordinations with the Cu adatoms. It is worthwhile to note that TPA also improves its commensurability with the substrate by such a rotation. The adatoms are again located upon the h sites of the substrate, while the phenyl-ring of the TPA is again located upon the sb sites of the Cu-lattice. The oxygen atoms of the carboxylate group which are not involved in the monodentate bonding to the adatoms are located in vicinity to a Cu atom in the first layer, although not fully on a t site.

As can be seen from Figure 4.25b, TPA indeed forms metal-organic coordination chains. These chains are roughly aligned to the $[1\bar{1}0]$ direction of Cu with the Cu dimers alternatingly on two neighboring Cu-troughs. In this sense, the Cu(110) template works

similar for TPA as for TMA. Nevertheless, TPA is not fully aligned to the $[1\bar{1}0]$ direction. Furthermore, the mesoscopic structure does not follow a 1D but a 2D arrangement in form of compact islands, see Figure 4.25a. The reasons for this is that neighboring chains easily align next to each other being probably stabilized by hydrogen bonding. In this sense, the seemingly unnecessary third functional group of TMA is essential to create separated 1D chains, as it increases the minimum distance between chains and limits the possibility for inter-chain hydrogen bonding.

4.6 Comparison and Discussion

A striking feature of the MOCC-S and also of the TPA-MOCC is that the Cu dimer is imaged by STM as one single spot, whereas a single Cu adatom in a hollow site does not give any significant feature at all in the STM (see Figures 4.18b and 4.21d). This in turn means that also for other systems adatoms may be involved in the structure formation process without being visible by STM. At least the possibility of having adatoms involved in the structure formation without being directly visible by STM should thus be kept in mind. This might explain other seemingly not fitting adhesion data in a better way, in particular for supramolecular systems involving carboxylate acids [119,120].

The comparison of the TMA-MOCC-S and the TPA-MOCC shows, that the templation concept is in principle extendable from one adhesion molecule to another. Metal-organic chains can likewise be created with very similar adhesion geometries. While transferability thus seems to be in general quite high, certain limitations apply:

- **Details of adhesion geometry might vary.** TMA and TPA seem to prefer a quite similar adhesion geometry for their functional groups. On the other hand, the functional groups are differently positioned on the phenyl ring for TMA and TPA. This results in a different orientation of the molecule as a whole in order to accommodate its functional groups on their preferred sites. Generally, one should thus expect different molecular orientations for geometrically different although functionally similar molecules. As seen here, this influence is not as strong as in 3D chemistry where TMA and TPA would form completely different networks since the presence of a surface strongly influences the adhesion geometry. Nevertheless, at least a second order correction in the structural properties should be anticipated for every change of the molecule.

- **Lattice mismatch.** The same argumentation is of course even more true when using non-commensurable molecules. The case of TPA seems to hint that commensurability to the substrate is of great importance for an effective ordering induced by the substrate. This issue will be discussed in more detail in chapter 6.
- **Linear molecules not necessarily form 1D structures.** TMA has been shown to form individual metal-organic chains though having a triangular symmetry itself. The linear TPA forms chains but within compact 2D islands as it lacks the third functional group of TMA as spacer. In a more general way, we can conclude that the creation of isolated 1D chains requires spacing mechanisms by any means, i. e. provided by the nanotemplate or by the structure of the molecule itself.

Especially this last point clearly shows that the use of an anisotropic surface does not solve alone the issue of defining an adhesion geometry. While such a substrate favors a unidirectional growth, it does not exclude the possibility of growth also in any other direction. Another example for this behavior will be shown in section 6. A way to solve this issue would be to use a surface with a much stronger distinction between the two surface directions. This might include a reconstructed or vicinal surface [30,31,40,43,45]. Nevertheless, one should note that the reconstruction of a surface might also depend on the presence of an adsorbate which can lead to its removal.

A natural extension to the results presented here are metal-organic coordination chains having metal centers of different elements than that of the substrate. In the following chapter we will investigate the possibility to create such extrinsic metal-organic coordination structures in the same templated growth mode as shown here.

Chapter 5

Extrinsic metal-organic structures

5.1 Introduction

As explained in the introductory paragraph of chapter 4, the high flexibility of metal-organic coordination networks (MOCN) is due to the possibility to freely combine metallic node and organic linker molecules depending on the desired application. The metal-organic coordination chains (MOCCs) introduced in the last chapter were formed by Cu dimers and TMA on a Cu substrate. While it was shown there that it is possible to exchange the organic linker molecule and still keep the general principle of templation, the possibility to exchange also the metal centers has still to be demonstrated. Metal-organic structures formed by metal nodes which are not of the same element as the underlying metal surface will be referred to as “extrinsic” structures in comparison to intrinsic structures using the same element.

It has already been shown that extrinsic MOCNs can be formed on a metal surface in UHV by the co-deposition of other metal atoms (e. g. Fe or Co) and carboxylic acids on Cu(100) and other isotropic surfaces [38, 107, 109–112, 124]. Different bonding motifs were generally observed when using different metal atoms. It is thus not a priori clear, if it is still possible to use the principle of substrate templation when using a different metal center.

Such an exchange of the metal centers would be important especially for the creation of functional surfaces. Although ferromagnetic [162] and antiferromagnetic [163, 164] behavior is reported for Cu carboxylates in 3D supramolecular structures, we do not anticipate specific magnetic properties for Cu in our case due to the coupling with the Cu surface. The first choice are thus intrinsically magnetic atoms like Fe, Co or Ni. 2D

surface MOCN have so far experimentally shown paramagnetic effects [165] but it is not clear if this is a general phenomenon or if it depends on the details of the used structure. Moreover, no matter what the result for 2D MOCN is, the creation of a one-dimensional chain of equally spaced magnetic nodes on a surface would offer interesting possibilities to test 1D magnetic properties.

It has recently been demonstrated that by self-organization it is possible to create 1D chains of close-packed magnetic atoms at surfaces [40, 42, 166]. The adatoms there are arranged in chains of finite length, showing unexpected ferromagnetic behavior [40]. Ferromagnetism was only observed at sufficiently low temperature when the spin flips caused by thermal agitation (superparamagnetism) are suppressed. The distance of the metal centers in these chains is given by the lattice constant of the substrate. The use of organic linkers would allow on the contrary to regularly place the metal centers at distances that are multiples of the substrate lattice constant. Depending on the existence of an interchange mechanism this might lead to interesting 1D magnetic phenomena.

5.2 Fe-TMA-chains

5.2.1 Chain growth and structure

Fe was deposited onto the Cu(110) surface from a metal MBE source during or after the deposition of TMA. The post-deposition of Fe on MOCC-S did not significantly alter the MOCC-S structure but created Fe islands in between the MOCCs. The exchange of Cu with Fe in existing MOCC-S therefore seems not to be possible in this direct way. To achieve Fe-TMA chains, the creation of Cu-TMA-MOCCs has thus to be prevented. On the Cu(001) surface this is more easily done since, at room temperature, Cu-TMA-complexes do not form automatically without further annealing. On that surface, a direct co-deposition at room temperature with post-annealing is indeed enough to form Fe-TMA local complexes [107, 109].

In order to prevent the formation of MOCC-S structures, TMA was deposited at a substrate temperature below 250 K, where, as it was shown above, nearly no MOCC-S are found. 240 K was typically used to allow for an effective TMA diffusion on the surface to occur. Fe was then deposited, while keeping the substrate cooled. The Fe deposition (see Figure 5.1a) does not induce any structure formation which is significantly different for what was found without Fe at this temperature (compare with Figure 4.7). Fe

deposition on a clean substrate at this temperature results in the formation of small islands (sizes of about 1-2 nm, see Figure 5.1b). Such measurements were also used to calibrate the Fe flux, as the Fe does not intermix with the Cu(110) substrate at these temperatures [167]. Similar Fe islands are also found in between the low-temperature TMA-structures (Figure 5.1a).

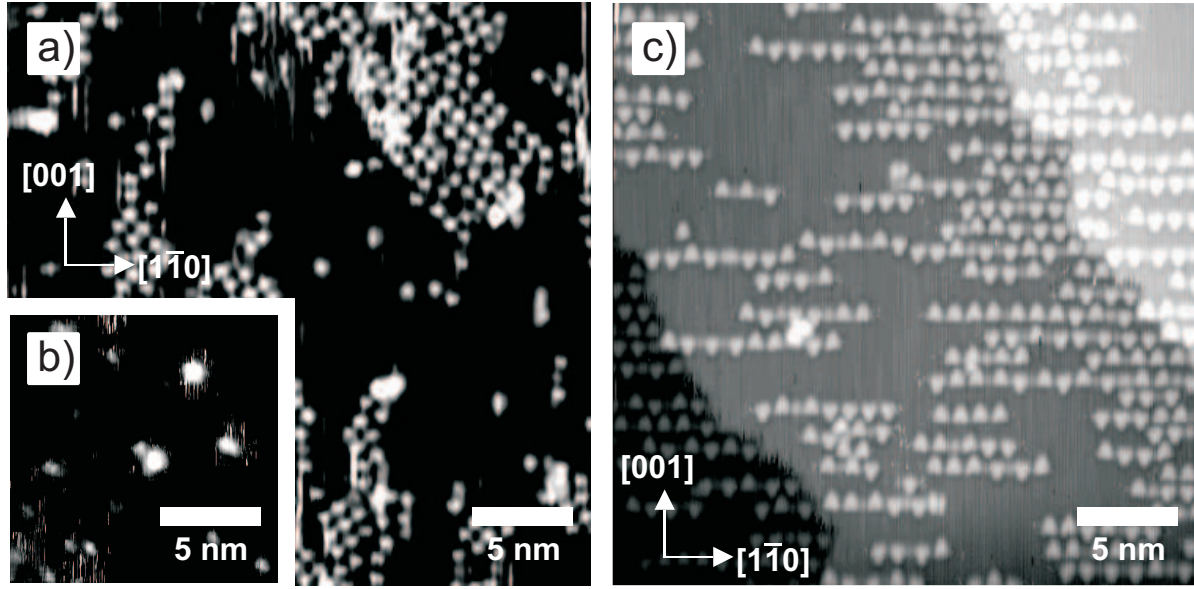


Figure 5.1: a) 240 K deposition of 0.30 ML TMA and 0.04 ML Fe. No difference is found for the low-temperature TMA structures with and without iron (compare with Figure 4.7). b) Island formation without TMA for Fe deposition at 240 K. c) Same surface as in a) after annealing to 380 K: MOCC-Fe chains on Cu(110).

Only upon annealing to room temperature, or – for even more regular structures – upon shortly annealing to 380 K, a new type of MOCC (MOCC-Fe hereafter) is created (see Figure 5.1c). The obtained MOCC-Fe have an in-chain periodicity of (10.3 ± 0.2) Å, corresponding to (4.04 ± 0.15) lattice spacings. The minimum distance of neighboring chains along [001] is again three lattice spacings. The supramolecular structure is thus a (4×3) . The relative number of MOCC-Fe grows monotonically with the Fe coverage as can be seen from Figure 5.2a, demonstrating that the MOCC-Fe chains are indeed due to the Fe deposition. An Fe coverage of 0.04 ML is enough to observe more than 63% of MOCC-Fe, while for Fe coverages larger than 0.08 ML a saturation is observed and Fe islands start to nucleate on the terraces. This proves that the reduced periodicity of $4 \times$ is not due to a lack of Fe but is the intrinsically preferred adhesion geometry for $(\text{Fe-TMA})_n$.

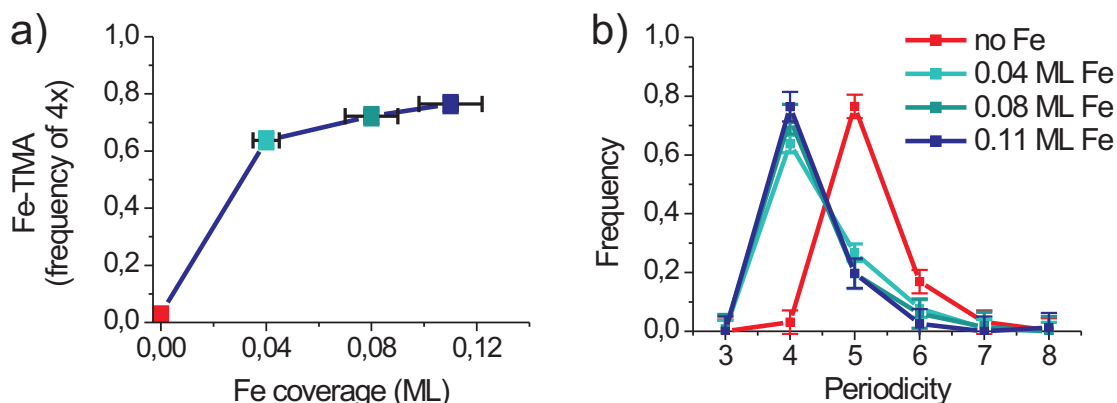


Figure 5.2: a) Number of MOCC-Fe as a function of Fe coverage. The colors of the measurement points correspond to the distributions shown in b); b) Distribution of measured periodicities for different Fe coverages, red: without Fe, cyan, blue, dark blue: increasing Fe coverage.

Figure 5.2b shows the distribution of measured periodicities for various Fe coverages. As can easily be seen, the distributions with and without Fe have a very similar shape, being only shifted in the peak position. For the case of $(\text{Cu-TMA-Cu})_n$, the long tail of the distribution shows that a significant number of chains has a periodicity of 6 or longer (17% for $6\times$, 3% for $7\times$). Also, about 3% of all Cu-TMA-chains have a periodicity of four. This can only be explained by admitting that in about 25% of the cases two TMA molecules are not separated by two but by one, three, four or even five Cu adatoms. These less frequent configurations are most probably energetically less favorable. For the case of just one Cu adatom this has indeed been proven in section 4.3.2. Such structures may nevertheless form locally, as there is still a net gain in energy in comparison to unbound molecules and atoms.

For the Fe-TMA system the situation is more complex. In fact, the $5\times$ periodicities that are still observed after Fe-structure formation can either be explained by chains which keep a Cu dimer as metal center (MOCC-S) or by chains having a Fe dimer (a $5\times$ MOCC-Fe) or by a mixture of both. From the similar shape of the distributions for Fe and Cu one can argue, that statistical reasons exist in both cases to have 25% of chains with more or less than the ideal adatom number. This would mean that also the $5\times$ structures would be formed by Fe. A fine resolved STS might in principle allow to discriminate the two cases. On the other hand, no direct in-situ comparison to the $(\text{Cu-TMA-Cu})_n$ is possible and comparisons could only be made to the $(\text{Fe-TMA})_n$ which in

principle can have a different electronic structure at the Fe centers than a hypothetical $(\text{Fe-TMA-Fe})_n$. Given the problems expressed in section 4.3.3 in reliably measuring the STS on the Cu adatoms, we refrained from STS experiments on these structures, leaving as an open question the nature of the metal nodes in the $5\times$ impurities.

5.2.2 DFT-results

DFT calculations were performed by G. Fratesi et al. to clarify the structure also for the MOCC-Fe systems [156,168]. Due to the preferential $4\times$ periodicity along the chain and basing on the results obtained for the MOCC-D high-coverage phase, only one Fe adatom was placed in between two TMAs. After full structure relaxation the lowest energy structure turned out to be again a structure in which the Fe adatom is located upon an h site of the substrate and the TMA is close to a sb site. By comparing with the MOCC-S structure, the position of the phenyl ring is only 0.09 Å higher. The metal-carboxylate bond is still unidentate and the Fe-O distance is 1.95 Å, i. e. 0.07 Å shorter than for the Cu-O bond. The fully relaxed structure can be seen from Figure

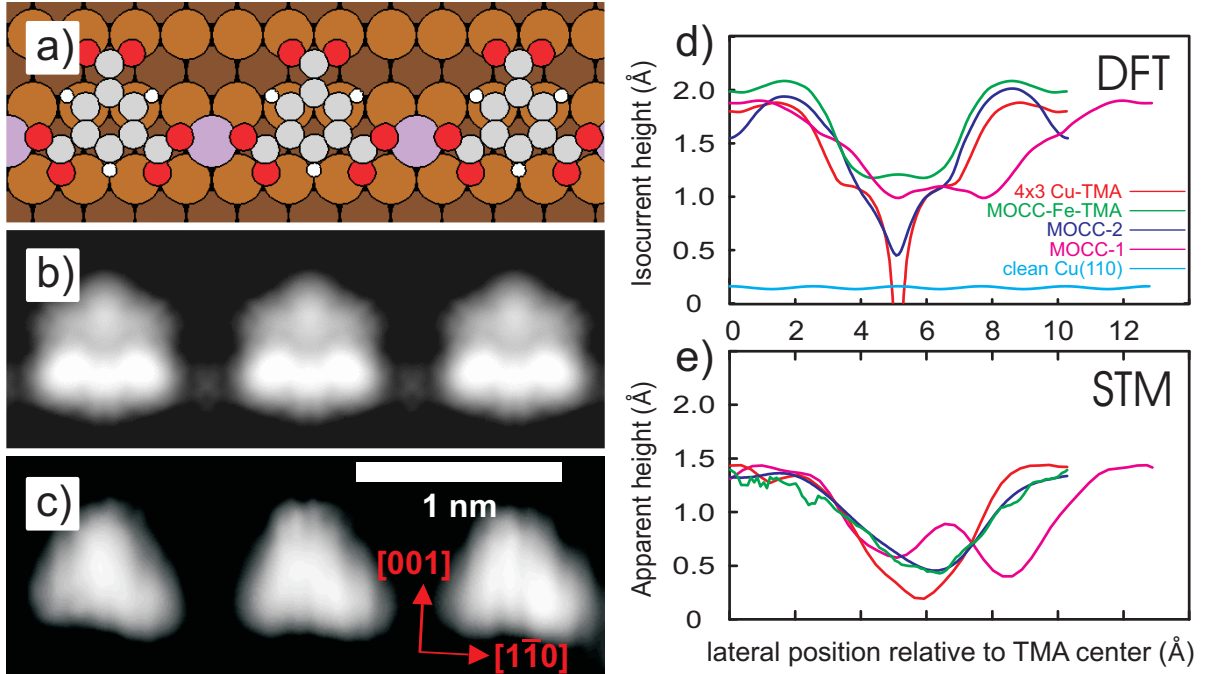


Figure 5.3: Comparison of DFT and STM results for MOCC-Fe. a) Structural model of the fully relaxed adhesion geometry. b) Simulated and c) measured STM image. d) and e) Comparison of lines scans through simulated (d) and experimental (e) STM images along the chain for different $5\times$ and $4\times$ periodic structures.

5.3a. Simulated STM images were again used to compare DFT and STM results (see Figures 5.3b-c).

Although from a first visual inspection the simulated and experimental STM images seem to agree less well than for the case of Cu-TMA, the most important features are reproduced. Both experimental and simulated STM images show only a faint feature in between the TMA molecules which, depending on the contrast, is typically only barely visible in 2D representations. In order to make a quantitative comparison, linescans have been analyzed along the chain direction for MOCC-Fe, MOCC-D, (5×3)-MOCC-S, and (4×3)-MOCC-S structures¹ for both simulated and experimental STM topographs (Figure 5.3d and e respectively). The direct comparison demonstrates a good agreement with the same trend in the relative heights of Cu, Fe adatoms and TMA molecules. It furthermore shows a clear difference between the MOCC-Fe and the (4×3)-MOCC-S impurities of the Cu system both for theory and experiment.

An analysis of the total energies was also performed. It was shown in section 4.3.2 that it is possible for the Cu based MOCC-S structure to compare the energies of the 4× and 5× structures, having 1 and 2 Cu adatoms per unit cell, respectively. This comparison is not trivial, as it involves different numbers of atoms and different sizes of supercells in DFT. While the latter issue can be addressed directly within the framework of DFT, the problem of a different number of atoms can only be solved by knowing or calculating the energy necessary to “create” an extra atom by removing it from a reservoir. For the metal adatoms this is the so-called bulk-cohesive energy which describes the energy of a metal atom attached to the bulk (e. g. in a step). While calculating this energy is possible for Cu, it is a known problem of DFT that the cohesive energy of Fe can only be computed within large error bars [156]. For our system these error bars are almost as large as the calculated energy difference between the two periodicities, making it impossible to unambiguously confirm the energetic superiority of the 4× structure.

¹(4×3) impurities exist in the MOCC-S system in rare cases ($\approx 3\%$ of all chain segments), see section 5.2.1

5.2.3 Magnetic properties

The construction of MOCC-Fe structures demonstrated in the previous section has to be regarded as a proof that the substrate templating effect works also for extrinsic metal-organic coordination chains. However, one of the reasons for exchanging Cu with Fe is, as stated above, the possibility to create structures which might show interesting and uncommon magnetic properties. As a consequence, it is tempting to investigate the magnetic properties of this system.

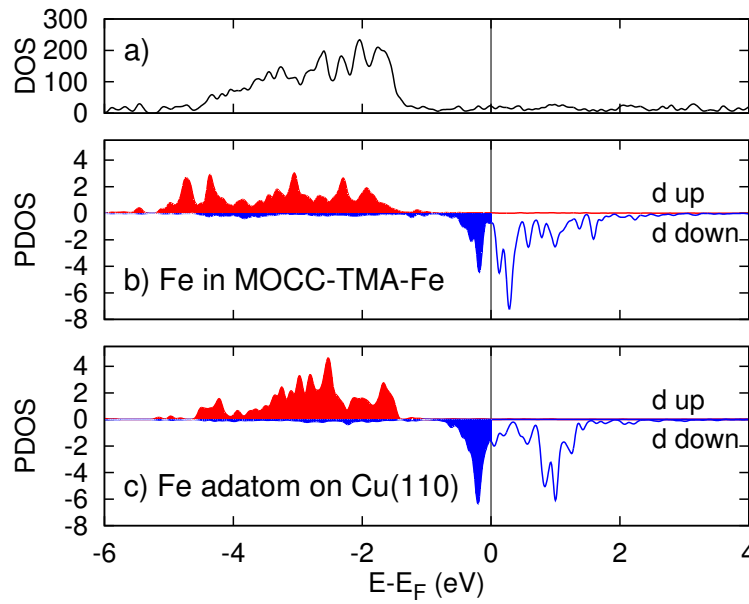


Figure 5.4: Spin-polarized calculation of MOCC-Fe. a) Total DOS of MOCC-Fe. b) Spin-polarized projection of the density of states for the d-states of the Fe center. c) Corresponding calculation for a free Fe atom on the same surface [156].

DFT offers some direct means for such an investigation. An analysis of the electronic structure of the calculated MOCC-Fe structure shows that the molecule-adatom bonding is slightly different than for the case of $(\text{Cu-TMA-Cu})_n$. Relative to a neutral Fe atom, the occupation of the Fe-s-states is reduced by 1.3 electrons, a reduction which is much stronger than that in the case of Cu (0.2 electrons for each Cu adatom in MOCC-S). It should be noted that the atomic configuration of an isolated Fe is $3d^6 4s^2$, thus a partially filled 3d shell and two electrons in a filled 4s shell, whereas Cu has $3d^{10} 4s^1$, thus a filled 3d and only one electron in 4s. One possibility to explain the different behavior of the metal centers and their different coordination is this different atomic configuration which allows Fe to donate more s electrons than Cu. The final occupation

of the $4s$ states in the MOCC is similar for both structures, being 0.7 for Fe and 0.8 for Cu. In the MOCC-Fe, the d states even increase their filling by 0.5 electrons. As the occupation of the d -states is directly relevant for the spin state of the system, the existence of an effective spin moment seems possible.

DFT is able to explicitly calculate the spin contribution to the magnetism, whereas the orbital moment is still more complicated (in principle possible, see e. g. [169]). The results of the spin-polarized calculation of the Fe-TMA system can be seen in Figure 5.4. Figure 5.4a displays the total DOS, while in Figure 5.4b the projected spin-polarized density of the Fe d -states is shown. The majority *spin-up* states are completely filled and well hybridized with the other states of the structure (mainly Cu d -states in the range from -5 to -1 eV). The splitting between the *spin-up* and *spin-down* states is significant and only a part of the *spin-down* states which lie in the energy region of the substrate s -states is filled. This results in a quite strong spin-polarization of $3.3 \mu_B$ per Fe atom. Figure 5.4c shows in comparison the projected DOS of an isolated Fe on the same surface. Its spin polarized DOS is very similar and so is the spin-polarization of $3.2 \mu_B$.

The similarity between the free Fe adatom and the Fe in the MOCC-Fe shows that the spin-splitting of the d -states is not much influenced by the presence of the molecular linkers. The strong bonding and hybridization with the molecular states changes the electronic structure and shifts states in energy especially around the Fermi level, but in comparison to the broad Fe- d -bands which extend from about -5 V to +3 V the changes do only weakly affect the overall spin-polarization.

5.3 Comparison and Discussion

Fe was found here to be able to complexate more TMAs than Cu. This is reflected in the stronger charge transfer per adatom. In comparison to the results on Cu(100) we believe that this is a general trend [106, 107, 109].

The fact that about 25% of all chain segments have a non-standard periodicity is definitely a problem for possible applications. If the observed $5\times$ impurities in the MOCC-Fe are due to Cu-dimers the problem can in principle be solved. Using a substrate which itself does not offer any adatoms (or very few of them) extra co-deposited metal-centers will be free to form their preferred structure. If the impurities are formed by Fe dimers though another surface would probably exhibit the same problem. It is possible that a

fine tuning of the lattice mismatch of the molecular linker can change the probability of such impurities as a larger misfit might favor more adatoms to reduce the strain per bond. On the other hand we do not have any evidence for a significant strain within the structure. Therefore, these impurities so far have to be seen as intrinsic property of the used growth mechanism.

A large magnetic anisotropy [170] was recently found for individual adatoms at low temperatures. These adatoms are not particularly ordered on the surface and the only stabilization of these atoms against diffusion and island formation is the low temperature. The use of MOCNs or MOCCs would allow to order and stabilize those systems. The spin-polarized DFT calculations show that the Fe atoms in the created MOCC-structures are – at least in principle – well capable of keeping at least their spin moment. The strength of the spin response can be expected to be similar to that of free atoms on a metal surface. This is a necessary but not sufficient condition for the existence of magnetic effects in MOCCs. The orbital moment of the Fe has not been tested in this investigation and only with a significant orbital magnetic moment such effects will arise ²

When thinking of collective phenomena such as ferromagnetism in 1D, an interaction mechanism is furthermore necessary. While the distance of neighboring Fe atoms is relatively large for a direct spin-spin interaction, an exchange coupling via the substrate is in principle possible. Exchange interaction has been measured between layers of Ni and Co being separated by a Cu layer, where even for Cu thicknesses of 8 ML exchange correlation has been found [171]. The coupling strength was oscillating and decaying exponentially with distance, having maxima at Cu layer thicknesses of 2.5 ML, 5 ML and 7.5 ML. A theoretical study has extended this concept to adatoms and has shown that magnetic adatoms can have an exchange interaction via the substrate electrons which depends on the distance in an oscillatory manner [172]. To use such an interaction mechanism, it will be necessary to change the molecular linker for optimizing the inter-spin distance with respect to a maximum of the coupling. A change of the substrate element might also help to enhance a potential coupling mechanism.

²Recent calculations have shown, that such a orbital moment exists for pure Co chains on Cu(100) [169].

Chapter 6

Chiral structuring

6.1 Chiral chains of Phe-Phe

6.1.1 Introduction

Methods to synthesize enantiomerically pure compounds are necessary for chemicals and drug synthesis. The approaches range from direct enantioselective biological production to purely technical abiological synthesis [173]. Heterogeneous catalysis uses small amounts of chiral catalysts to catalyze the enantioselective synthesis of large amounts of chiral products from prochiral feeding material. Within the catalysis process the chiral catalyst is often adsorbed on a metal surface [174,175] where it causes a chiral patterning as has been exemplarily shown for tartaric acid on Cu(110) [175–178].

Recently, several studies reported the adsorption of different chiral molecules to specific low index metal surfaces, typically resulting in the formation of extended chiral domains (see [75, 179] and references therein). For technical applications the surfaces can in general be neither expected to be pristine nor of a single and simple surface geometry. An important question to be answered concerns thus the possibility to generalize the obtained results to other surface geometries and topologies. Also to understand the templating role of a substrate, the question how chiral molecular adsorption changes and can be influenced by different surface geometries is strongly relevant. We have exemplarily compared the adhesion of one chiral molecule with several different functional groups on two Cu single crystals with different surface orientation.

A prototype example of chiral molecules are amino acids and their polymerized condensation products, the peptides. Monolayer as well as submonolayer coverages of nearly

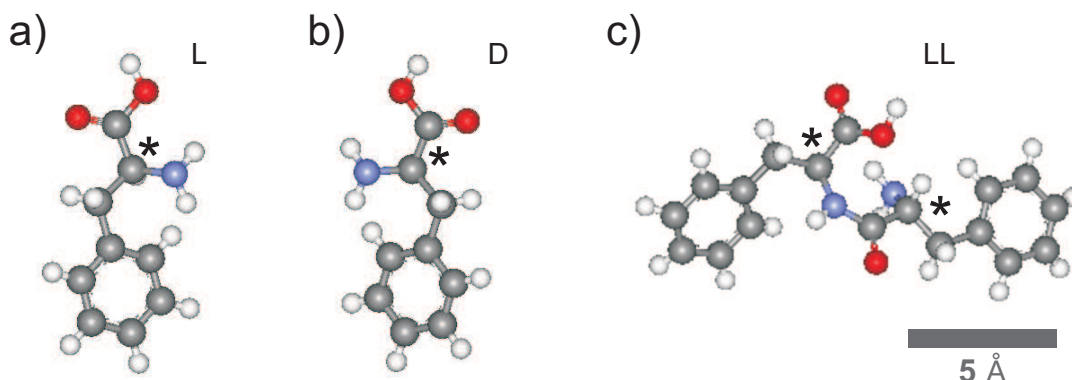


Figure 6.1: Model of a) L-Phe; b) D-Phe; c) L-Phe-L-Phe (C: grey, H: white, O: red, N: blue). The chiral C-atoms have been marked (*). The single Phe are oriented such that the H-atom at the chiral C-atom points to the back.

all natural amino acids have been studied on a wide range of surfaces [75,179]. Generally it was concluded that the single amino acids bind to the surface with more than one of their functional groups. The possible intermolecular interactions are thus limited and can be expected to be influenced by the substrate geometry. One step further to larger biological components with increasing complexity are peptides, which in their simplest form of dipeptides consist of two amino-acids chemically bound under water elimination by a peptide bond. With respect to single amino-acids, dipeptides are limited in the number of functional groups facing the substrate at the same time because of steric hindering. Thus, one can expect that with increasing molecular size more functional groups will be available for inter-molecular interaction. In this sense, dipeptides can provide a first insight into the changes expected to happen on the way to larger biomolecules on surfaces.

Only few small peptides have been investigated so far on Cu surfaces, namely the Ala-Ala [180] and Tri-Leu and Tri-Ala [181] on Cu(110). For Ala-Ala elongated unidirectional chiral islands are obtained. For Tri-Leu and Tri-Ala infrared (IR) adsorption results exist but no STM-data. From the IR data it is concluded that Tri-Leu and Tri-Ala exist on the surface in an anionic form in different local motifs similar to β -sheet arrangements and therefore linearly aligned to each other.

Here we present the Phe-Phe dipeptide on Cu(110) in direct comparison to results obtained by S. Stepanow et al. on Cu(100). The analysis of Phe-Phe on Cu(110) has been

part of a joint work with F. Stadler [82] for the growth and with M. Lingenfelder who has analyzed the atomistic structure and the chiral recognition arising from the intermolecular attraction in collaboration with the theory group of G. Tomba, L. Colombi-Ciacchi, and A. DeVita of the University of Trieste and the Kings's College in London [182]. As a further source for comparison the literature data on Ala-Ala/Cu(110) were used [180].

Figure 6.1a and b shows the single Phe amino acid, which has one chiral C-atom (marked by a star in Figure 6.1a and b) and thus exists in two chiral which allows for two chiral forms (L and D). The dipeptide Phe-Phe thus exists in total in four chiral configurations. Out of these, the enantiomers L-Phe-L-Phe and D-Phe-D-Phe were studied (see Figure 6.1c for a representation of L-Phe-L-Phe). Different UHV-STM systems were used for the experiments on Cu(110) and Cu(100), respectively. Evaporation occurred according to the parameters outlined in section 2.4.3. During deposition, the samples were kept at 300 K and only for the Cu(100) an annealing was performed to 400 K for 5 minutes.

6.1.2 L-Phe-L-Phe and D-Phe-D-Phe on Cu(110)

The deposition of L-Phe-L-Phe on Cu(110) kept at room temperature results in the formation of ordered and highly periodic chains (see Figure 6.2). No specific attachment to terrace steps is observed. With increasing coverage the average chain length increases until for high coverage, chains run all across terraces.

The molecular chains are not oriented along the high symmetry directions of the Cu(110) surface but form an angle of $54^\circ \pm 2^\circ$ with respect to $[1\bar{1}0]$. This orientation is in close agreement with the $[1\bar{1}2]$ direction of the substrate that forms an angle of $54,7^\circ$ with $[1\bar{1}0]$. The mirror symmetric $[112]$ orientation is never observed, thus implying that the chain formation is chiral. Correspondingly, for D-Phe-D-Phe the only observed chain orientation is along the $[112]$ direction.

Within the chains, individual Phe-Phe molecules are imaged as units consisting of two circles connected by a central band. Depending on the tip conditions, the Phe-Phe molecule is either imaged above or below the surface (see Figure 6.2a and b). The periodicity along the L-Phe-L-Phe chain is $(8.5 \pm 0.7) \text{ \AA}$, which closely corresponds to the distance of over-next Cu atoms along the $[1\bar{1}2]$ direction (8.85 \AA). As shown in Figure 6.2, the molecular direction (defined as the line connecting the centers of the two phenylrings) of the L-Phe-L-Phe is tilted by $53^\circ \pm 2^\circ$ counterclockwise out of the chain

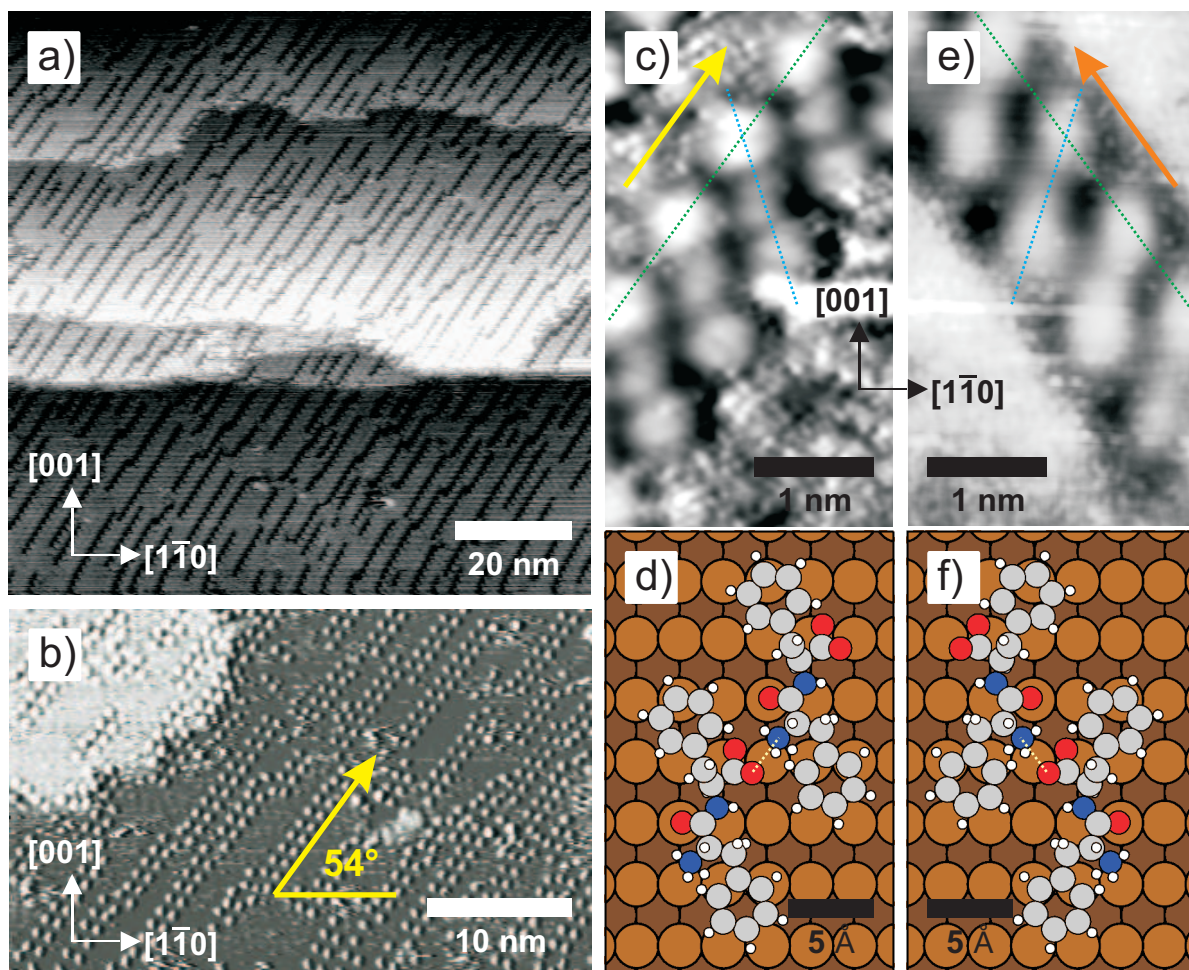


Figure 6.2: Representative STM images of Phe-Phe on Cu(110). a) Overview image of L-Phe-L-Phe in an imaging mode in which Phe-Phe is imaged below the surface. b) Enlarged view in opposite imaging mode. The image has been enhanced by derivative filtering. The molecular chain direction is shown by an arrow, one Phe-Phe molecule is highlighted. c-d) Comparison for L-Phe-L-Phe of c) high resolution STM image and d) adhesion model (C: grey, H: white, O: red, N: blue). e-f) Comparison for D-Phe-D-Phe of e) STM image and f) model [182]. In the high resolution STM images the chain and the molecular directions are highlighted by green and blue dotted lines, respectively. In the model the bond between the NH_3^+ and the COO^- group is marked by a white dotted line.

direction, having thus in total an angle of $108^\circ \pm 2^\circ$ with respect to the $[1\bar{1}0]$ direction [82]. The mirror symmetric direction is observed for D-Phe-D-Phe (see Figure 6.2c and e).

A detailed model for the adhesion of Phe-Phe on Cu(110) based on STM results and density functional theory calculations can be found in [182]. While a different adsorption geometry was found for a single Phe-Phe molecules, it was shown there, that molecules of the same chirality can form dimers in a process of chiral recognition under reorientation to the geometry described above. It was also demonstrated that

Phe-Phe exists on Cu(110) in a zwitterionic form. Bonding occurs through attractive electrostatic interaction of the COO^- -group of one molecule to the NH_3^+ -group of the next molecule [182] (see Figure 6.2d and f), giving rise to pronounced 1D supramolecular arrangements. The molecule binds to the surface with the functional groups which are located at the central backbone of the molecule. The phenyl rings are positioned above the backbone and thus farer from the surface. A considerable amount of freedom exists for phenyl rings to move and they are expected to interact with those of neighboring molecules by means of π - π -interactions. In the STM images the phenyl rings typically appear more pronounced than the central part of the molecule. It should be noted, though, that the position of the phenyl rings does not provide reliable information about the orientation of the molecule and thus the detailed molecular structure can only be extracted from the DFT results [182].

6.1.3 L-Phe-L-Phe and D-Phe-D-Phe on Cu(100)

The deposition of L-Phe-L-Phe or D-Phe-D-Phe on Cu(100) at room temperature was found not to lead to any ordered structure. Instead, the molecules seem to be mostly mobile on the surface as they are normally moved around by the STM tip even at high tunnelling resistances. Only upon annealing to 380 K or higher for 5 minutes, regular and ordered chains are obtained. Obviously, a temperature of 300 K is not enough for Phe-Phe on Cu(100) to activate the chain formation process. For Cu(110) it was found that the chain formation includes a conformational change within the Phe-Phe molecule [182]. Depending on the actual molecular conformation which is of course influenced by the underlying surface geometry, the necessary energy for such a conformational change might vary. Without extensive calculations, which are clearly beyond the scope of the present investigation, this cannot be fully cleared up. On the basis of a detailed analysis of Phe-Phe/Cu(110) and the strong similarities between the two systems, also for Phe-Phe/Cu(100) we attribute the necessary temperature increase on Cu(100) to internal conformation changes of the molecule and not to surface effects such as the availability of adatoms or similar.

The annealing was typically carried out at 400 K for 5 minutes and tests with annealing temperatures up to 450 K showed no significant structural change in comparison to 400 K. This produces highly regular and ordered chains of Phe-Phe (see Figure 6.3). No specific step decoration is observed as on Cu(110) which also signifies that no adatoms

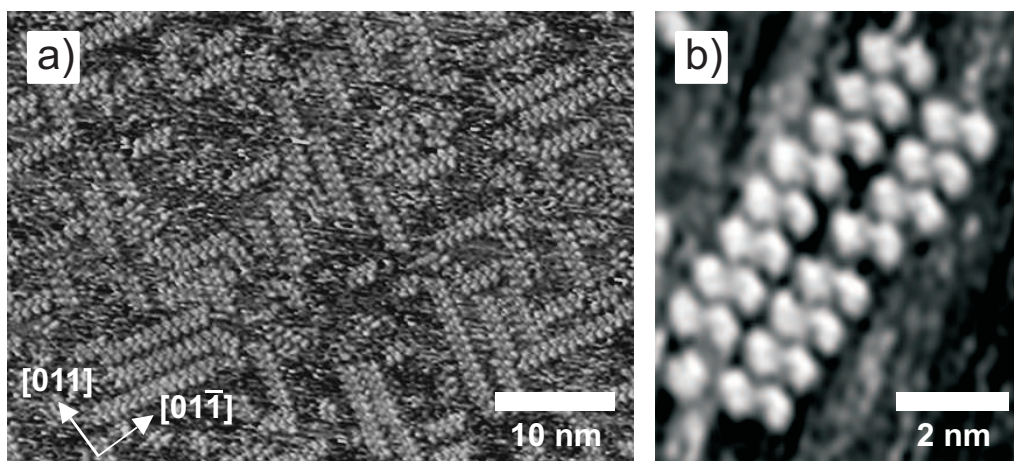


Figure 6.3: Representative STM images of Phe-Phe on Cu(100). a) D-Phe-D-Phe: overview image showing the chain formation. b) L-Phe-L-Phe: enlarged view. Images taken by [165].

are involved in the structure creation. The orientation of the chains is also chiral, L-Phe-L-Phe chains being oriented along $(+19 \pm 2)^\circ$ with respect to the $[0\bar{1}1]$ close-packed surface direction. This orientation is therefore assigned to the $[0\bar{2}1]$ direction forming an angle of $+18.4^\circ$. The periodicity along the chain is $(8.1 \pm 0.2) \text{ \AA}$, in close agreement with the next-neighbor Cu-Cu distance in this direction of 8.08 \AA . Since Cu(100) has a fourfold symmetry, Phe-Phe chains are also found with correspondingly identical probabilities along the symmetric $[02\bar{1}]$. The corresponding mirror directions are observed for D-Phe-D-Phe chains [165].

6.1.4 Chain length

The average length of the Phe-Phe chains on Cu(110) and Cu(100) grows monotonically with the coverage as can be seen from Figure 6.4a. For a given coverage, the average chain length is significantly larger on Cu(110). This difference can be explained by the fact that, due to the higher symmetry, two perpendicular equivalent directions exist for the chains on Cu(100) in comparison to the single chain direction on Cu(110). This results in a distribution of molecules into two instead of one direction “channels”, leading to a lower effective coverage per direction. Furthermore, especially at higher coverage, the orthogonal directions can also cause a steric mutual hindering of chain growth which results in chains meeting and blocking each other. On Cu(110), on the other hand, chains can grow in parallel without hindering interactions.

In Figure 6.4b and 6.4c the distribution of the chain length is plotted for selected

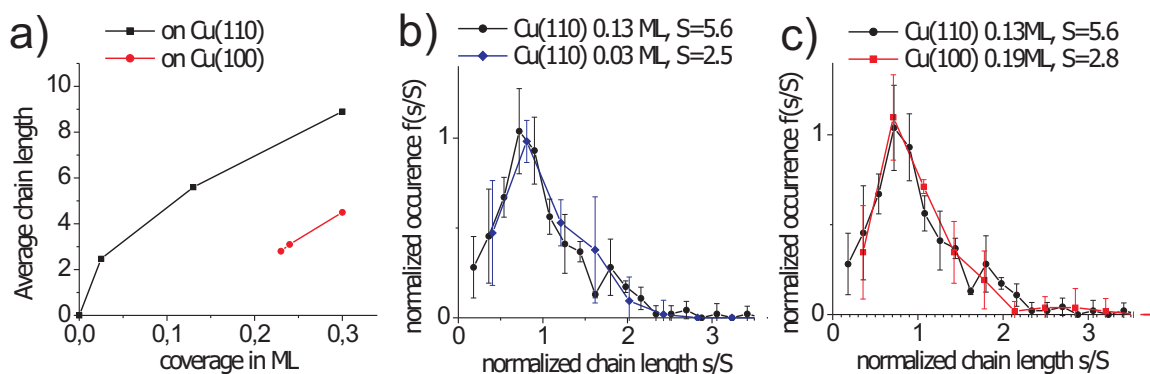


Figure 6.4: a) Increase of average chain length N with coverage for Phe-Phe on Cu(110) and on Cu(100). b) Length distribution of chains of different lengths on Cu(110) and c) of chains on Cu(110) and Cu(100). The relative number of chains of length s are counted and plotted, where the length s has always been normalized by division by the average chain length S . Only selected coverages are plotted for visual clarity.

coverages on Cu(110) and Cu(100). The curves list the normalized occurrence of chains having a length s/S where s is the actual chain length (number of Phe-Phe molecules per chain) and S is the average chain length for a given coverage (see also section 4.2.5). As can be easily seen from Figure 6.4b, the curves for different coverages of Phe-Phe on Cu(110) fall on a general line. The same is true for the Cu(100) substrate (not shown here). Moreover, as can be seen from Figure 6.4c where exemplarily one curve of Phe-Phe on Cu(110) and one on Cu(100) are shown, the two curves are identical within the statistical error bars. The curves are very similar to what was observed for TMA (see discussion in section 4.2.5 on page 47). Also here, the maxima of the curves are not $s/S=1$, so the same contradiction to theory exists as was explained for TMA in section 4.2.5. The most interesting fact here is that the normalized curves for Phe-Phe on Cu(100) and on Cu(110) are the same. From this we conclude that the process of chain formation has to be very similar on both substrate geometries.

6.1.5 Comparison and Discussion

From the surface geometries of Cu(110) and Cu(100) one might have expected to find a chain type structure on the anisotropic Cu(110) and a more 2D-like geometry on the Cu(100). On the other hand, the origin of the chain formation on Cu(110) is not the anisotropy of the substrate but the directionality of the zwitterionic bonding of the

Phe-Phe molecule on Cu(110). From the similar chain length distribution of Phe-Phe on Cu(110) thus a comparable directional bonding can also be anticipated on Cu(100). Nevertheless, this analogy is not enough to fully explain the details of the growth of the observed chains. In addition, when comparing the adsorption of Phe-Phe and Ala-Ala on the same substrate, different chain directions are found. This is surprising, as both dipeptides consist of the same backbone structure including the same functional groups and they differ only in the alkyl rest group. One could thus assume to find the same surface interaction and the same growth direction. As we will show in the following, both of these seemingly unrelated experimental observations can be explained using similar geometrical arguments.

Each molecule that interacts strongly with the substrate will have a preferred adsorption site on the substrate. Due to the periodic structure of the surface these sites are repeated periodically across the surface. If the interaction between molecule and substrate is stronger than the intermolecular interaction, all molecules on the surface will be found on such an equivalent surface site. Their intermolecular distance is thus defined by the periodicity of the substrate. This distance will in general not be the ideal bonding distance favored by the intermolecular interaction. Each intermolecular bond is thus not at its lowest possible energy, which can be described as stress which accumulates when the structure grows. Each new molecule in the structure adds to the overall stress until the overall stress is so high that it is energetically favorable to introduce a dislocation and to relax the stress by slightly relaxing all molecules according to the intermolecular forces. Alternatively, stress can terminate a structure growth at a certain maximum size.

A continuous and defect-free chain growth requires thus a spacing of substrate sites which is as close as possible to the optimal intermolecular bonding distance. On a single crystal surface only specific values of atom-atom distances (and multiples of these) exist. This can be seen very clearly for the case of Cu(110): only two specific directions exist which offer Cu-Cu spacings in the periodicity range of 8 – 10 Å, namely the $[\bar{3}32]$ direction with a Cu-Cu-distance of 8.48 Å and the $[1\bar{1}2]$ direction with a Cu-Cu-distance of 8.85 Å. All other directions on Cu(110) have significantly shorter or longer Cu-Cu distances (see Table 6.1).

In [180] Ala-Ala is proposed to be zwitterionic. Since it has been measured and calculated that this is also true for Phe-Phe and since it is exactly this zwitterionic structure that defines the intermolecular bonding [182], we can assume that the intermolecular interaction is comparable for both dipeptides. The intermolecular spacing, i. e. the dis-

Cu-Cu distance		existing lattice directions	
in a_0	in Å	Cu(110)	Cu(100)
$\sqrt{0.5}$	2.56	$1\bar{1}0$	$011, 01\bar{1}$
$\sqrt{1}$	3.61	001	$010, 001$
$\sqrt{1.5}$	4.43	$1\bar{1}2, \bar{1}12$	
$\sqrt{2}$	5.11	$1\bar{1}0$	$011, 01\bar{1}$
$\sqrt{2.5}$	5.72		$031, 03\bar{1}, 01\bar{3}, 013$
$\sqrt{3}$	6.26	$1\bar{1}1, \bar{1}11$	
$\sqrt{4}$	7.23	001	$010, 001$
$\sqrt{4.5}$	7.67	$1\bar{1}0, 1\bar{1}4, \bar{1}14$	$011, 01\bar{1}$
$\sqrt{5}$	8.08		$021, 02\bar{1}, 01\bar{2}, 012$
$\sqrt{5.5}$	8.48	$3\bar{3}2, \bar{3}32$	
$\sqrt{6}$	8.85	$1\bar{1}2, \bar{1}12$	
$\sqrt{6.5}$	9.22		$051, 05\bar{1}, 01\bar{5}, 015$
$\sqrt{8}$	10.22	$1\bar{1}0$	$011, 01\bar{1}$
$\sqrt{8.5}$	10.54	$3\bar{3}4, \bar{3}34$	$053, 05\bar{3}, 03\bar{5}, 035$
$\sqrt{9}$	10.84	$001, 2\bar{2}1, \bar{2}21$	$010, 001$
$\sqrt{9.5}$	11.14	$1\bar{1}6, \bar{1}16$	
$\sqrt{10}$	11.43		$031, 03\bar{1}, 01\bar{3}, 013$

Table 6.1: Cu-Cu distances on Cu(110) and Cu(100) in the 0 - 11.5 Å range. For the available distances the corresponding lattice directions are listed. In the first column all values are given in terms of the Cu lattice constant $a_0=3.615\text{Å}$.

tance between the interacting functional groups of neighboring molecules should thus be comparable for Phe-Phe and Ala-Ala. As the Ala-Ala molecule is slightly shorter than Phe-Phe, the overall periodicity for Ala-Ala chains, i. e. the molecule center-to-center distance, is expected to be smaller than for Phe-Phe. Indeed the Cu-Cu distance along the $[\bar{3}32]$ direction of Ala-Ala chains is 8.48 Å, whereas it is 8.85 Å in the $[1\bar{1}2]$ direction of Phe-Phe. In this sense, it is not the molecule-substrate interaction which defines a certain direction for the chain growth and thus for the intermolecular distance. In fact, the opposite is true since first the intermolecular interaction “chooses” a certain molecule-molecule distance and then the best matching Cu-Cu-distance is picked from the possible choices offered by the substrate geometry. This then implies a specific growth

direction¹. Of course it may well be that the best possible direction is not accessible as it does not comply with the local adhesion geometry of the molecule. For example, a molecule that binds with two or more groups to the surface could have limited rotation possibilities. The final structure can then be expected to arise from the balance between the energy gain through intermolecular bonding and the energy loss by changing the individual conformation on the surface. This is also the case for Phe-Phe on Cu(110), where conformational changes happen as a prerequisite for chain formation [182].

The same argument is qualitatively extendable to the Cu(100) surface. Assuming that the ideal intermolecular distance is close to the value of 8.85 Å found on the Cu(110) surface, no ideal candidate for a matching periodicity can be found among the possible Cu-Cu-distances on Cu(100) (see Table 6.1). Yet, the $[0\bar{2}1]$ and $[0\bar{5}1]$ directions offer distances at least close to this value (8.08 Å and 9.22 Å, respectively). Although the longer distance of 9.22 Å along the $[0\bar{5}1]$ direction is closer to 8.85 Å, the Phe-Phe molecules are found to form chains along the $[0\bar{2}1]$ direction, which may signify that either the intermolecular interaction is slightly different on both surfaces or that the optimal bonding distance is also not fully met on the Cu(110) surface, being in reality slightly shorter than 8.85 Å.

Overall, both surfaces can be seen as having similar geometrical properties for the Phe-Phe molecule: on both surfaces the molecules choose directions which keep the intermolecular distance within a certain optimal range. Only few distinct directions exist, which offer a matching periodicity, which are then chosen by the intermolecular interaction as direction of chain growth.

With increasing molecular size more directions of matching Cu-Cu lattice constants become available, i. e. the list in Table 6.1 becomes denser at longer distances. On the route to even larger biological molecules one may expect that commensurability is thus on average improved. Moving from smaller molecules to larger ones is therefore in a way similar to going from the Cu(110) to the Cu(100) surface: more directions become available for chain growth. This allows a growth in the preferred geometry, but different growth directions can interfere leading to a smaller overall size of the islands.

¹It should be noted, that this argumentation is valid for each type of intermolecular interactions, the only requirement being that the adsorbed molecule can undergo sufficient conformational changes (mainly rotation as a whole, but e. g. also internal rotations) to be able to adapt to the best possible direction offered by the substrate. For a detailed description of the intermolecular interaction of Phe-Phe please refer to [182].

6.2 Chiral supramolecular MOCNs

6.2.1 The concept

Approaches for structure generation at surfaces mostly concentrate on one specific type of molecule on one specific surface. Already in such a simple two-component system several thermodynamical phases can exist, depending e. g. on the temperature and the adsorbate coverage [75]. On the other hand, synthetical 3D chemistry nowadays routinely creates supramolecular crystals in a process referred to as crystal engineering. A huge knowledge exists on how to design structures using synthons and combining organic molecules with different functions and geometries [12, 13, 96, 98]. Combining molecules with different individual properties creates a multitude of possible structures. This abundance of possibilities is the real strength of the supramolecular approach. Here we will show that it is possible to follow the same route for structure creation also on surfaces. We create a surface-based chiral metal-organic coordination network using TMA as metal-organic linker and Phe-Phe a chiral molecule for the incorporation of chirality into the final structure. Cu(110) is used as a substrate because its low symmetry allows to avoid a complicated phase diagram and its templating effect induces the formation of ordered structures. Self-organization provides a long-range periodicity and high regularity with a self-defined stoichiometry.

Chiral supramolecular structures can be created also with achiral (non-chiral) molecules. So far this has been achieved by using completely achiral [107, 109, 110] or prochiral linker molecules [112]². Both for achiral and prochiral molecules mirror symmetric domains are always found in racemic mixtures across the surface (see also section 2.3.3). The advantage of using a molecule having true chirality already in 3D is thus the possibility to create a full surface in one enantiomerically pure domain. Above, we have shown that Phe-Phe is a chiral dipeptide which creates chiral structures on the Cu(110) surface (see section 6.1). Phe-Phe has only one carboxylate group and can not compete with TMA in acting as a linker between two or more metal centers in order to form metal-organic networks. This is important to retain a structural hierarchy in the pattern formation. Moreover, Phe-Phe exists on Cu(110) only in few different phases on the surface [183] depending only on the annealing temperature. Apart from these

²An example of supramolecular chirality created by the molecular packing inside an island can be found for the low temperature deposition of TMA on Cu(110), as shown in section 4.2.3.

advantages, the choice of Phe-Phe is more or less arbitrary, indicating that, at least in principle, analogous results might be obtained with different chiral molecules. The generality of this approach opens up possibilities for a wide range of structural variations.

The choice of TMA as metal-organic linker is ideally suited for such a combined approach. As we have shown in the preceding chapters, TMA forms metal-organic $(\text{Cu-TMA-Cu})_n$ chains on Cu(110) using two of its three functional groups. This leaves the third functional group open for further interactions on the surface. As this functional group points perpendicular out of the chains, we can expect to get a 2D surface pattern when adding a further molecule like the Phe-Phe. The phase diagram of TMA on Cu(110) is also relatively simple with the development of only one adhesion geometry for temperatures above 300 K and coverages below 0,5 ML.

6.2.2 Structure creation and characterization

The structure formation starts with the deposition of TMA on Cu(110). A short post-annealing to 380 K is used to create ordered and periodic chains (see section 4.2.4). L-Phe-L-Phe is then deposited at room temperature. The Phe-Phe molecules are found to be mobile on the surface at this temperature, which can be seen from frequent strikes in the STM images. Phe-Phe molecules might accidentally get caught between neighboring $(\text{Cu-TMA-Cu})_n$ chains, depending on their distance, but do not stay there permanently. Otherwise no further structure formation is observed (see Figure 6.5a). Upon annealing to 400 K Phe-Phe molecules change their adsorption geometry, similar to what is found for Phe-Phe alone on Cu(110) [183]. Phe-Phe is now found between TMA chains wherever a matching distance between neighboring chains exists and stays there permanently. As matching TMA-chain distances for Phe-Phe inclusion are not generally the case, the overall ordering is poor. Only after a further annealing to 450 K highly regular and compact mixed islands of TMA-Phe-Phe are formed as can be seen from Figure 6.5b. In between, remaining $(\text{Cu-TMA-Cu})_n$ chains are visible.

The mixed islands have a global chiral structure which is represented by the main high symmetry directions of the structure (see Figure 6.5b). As long as only one enantiomer (L-Phe-L-Phe or D-Phe-D-Phe) is used, only one type of domain exists and the islands can grow in size with increasing coverage, being only limited by the edge of the monoatomic substrate terraces. Figure 6.6a shows a magnified view of the islands inner structure revealing that the TMA-Phe-Phe structure consists of unidirectional rows. The

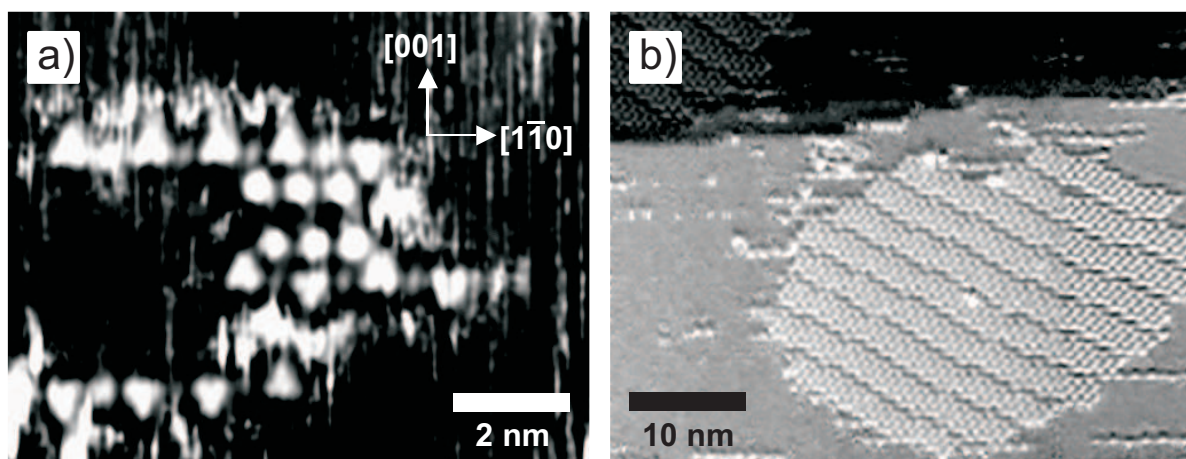


Figure 6.5: Deposition of *L*-Phe-*L*-Phe onto $(\text{Cu-TMA-Cu})_n$ -chains a) after deposition at 300 K, b) after annealing to 450 K.

rows are formed by an equal number of TMA and Phe-Phe molecules (ratio 1:1). It is an important feature of the observed structure that this stoichiometry is retained even under excess of one of its molecular constituents, which greatly facilitates the growth of this 2D compound. Extra molecules of either species are not incorporated into the structure but are found in separate pure domains at other areas of the substrate. Only at a very high total coverage (“under external pressure”) the formation of separate pure domains is spatially limited and non-stoichiometric structures are occasionally found.

The overall chirality of the structure is even more obvious when comparing domains of different chirality. Figure 6.6b shows domains formed upon codeposition of *L*-Phe-*L*-Phe and *D*-Phe-*D*-Phe. Neighboring domains of different chirality are not commensurable and therefore form complicated domain boundaries as shown in Figure 6.6c.

Figure 6.6a also reveals the molecular structure of the TMA-*L*-Phe-*L*-Phe islands in which two Phe-Phe molecules (blue) interlink two TMA molecules (pink). This substructure is then repeated to form a row. TMA molecules at neighboring rows face in opposite directions and interconnect via adatoms (dimers) at a distance of 5 Cu lattice spacings along the $[1\bar{1}0]$ direction. The whole structure can thus likewise be seen as formed by a chiral arrangement of regularly positioned Cu dimer rows for which TMA and Phe-Phe molecules provide the local and the supramolecular structural links, respectively.

The most frequent type of dislocation within the rows is produced by an alignment of three instead of two Phe-Phe molecules. When such a defect forms in a position inside an island it has to form along a line throughout the whole 2D crystal as otherwise

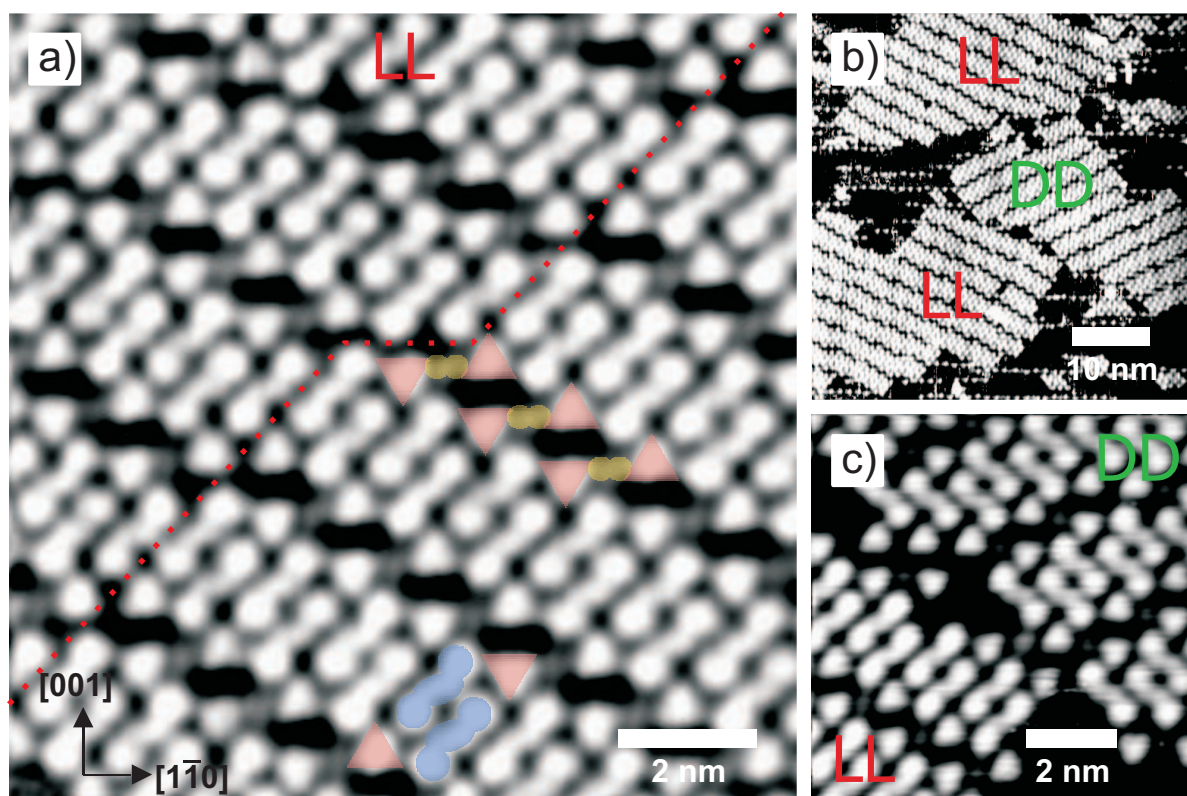


Figure 6.6: a) TMA-Phe-Phe structure. Only L-Phe-L-Phe have been used. The red dotted line indicates a line defect running from upper right to lower left corner. b) TMA-L-Phe-L-Phe and TMA-D-Phe-D-Phe structures with c) domain boundaries between supramolecular islands of opposite chirality.

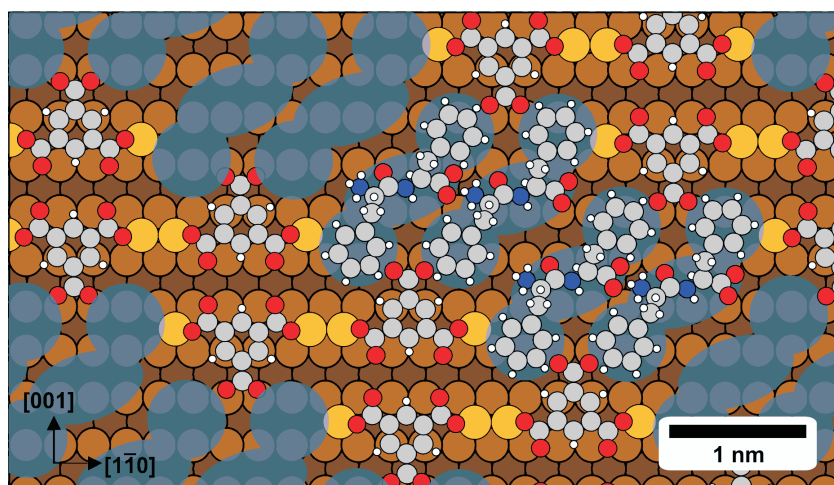


Figure 6.7: Model of the TMA-Phe-Phe-structure. Phe-Phe molecules are shown as grey-blue clouds. Color scheme used: C - grey, O - red, H - white, N - blue, Cu adatoms - yellow, Cu bulk atoms - bright and dark brown for first and second half-layer.

neighboring rows would not be parallel any more. Such a defect thus only occurs in form of a line defect of the whole island. Figure 6.6a shows such a line defect running diagonally through the image from the upper right corner to the lower left corner.

Using highly resolved drift-free STM images such as the one shown in Figure 6.6a a tentative model of the adhesion geometry has been constructed. As especially the Phe-Phe molecule is characterized by various internal degrees of freedom that cannot be resolved by STM alone, the model is to be seen as an approximate solution showing the possible intermolecular interactions rather than providing exact atomic positions. In matrix notation, the overlayer structure takes the form

$$\begin{pmatrix} a_0 \\ b_0 \end{pmatrix} = \begin{pmatrix} 8 & 6 \\ -5 & 2 \end{pmatrix} \cdot \begin{pmatrix} a_{[1\bar{1}0]} \\ b_{[001]} \end{pmatrix},$$

where $a_{[1\bar{1}0]}$ and $b_{[001]}$ are the unit cell vectors along the respective Cu directions and a_0 and b_0 are the unit cell vectors of the supramolecular overlayer structure (see also section 2.2.2). The size of the overlayer unit cell is thus 46 primitive unit cells of the crystal for two TMAs and two Phe-Phe molecules in comparison to 15 unit cells for one TMA in $(\text{Cu-TMA-Cu})_n$ -chains and at least 10 unit cells for a Phe-Phe in a Phe-Phe-chain depending on the chain distance [182]. The complete model is shown in Figure 6.7. The TMA molecules locally retain their chain structure with Cu-dimers through unidentate Cu-carboxylate bonding (see section 4.3.2) and we assume that each metal-organic chain is terminated by a Cu adatom in analogy to the MOCC-S structure (see section 4.2.4), although we do not have direct evidence for this here. The interaction between TMA and Phe-Phe is supposed to happen via hydrogen bonding between the third TMA carboxylate group and the hydrogen atoms of the phenyl-ring of Phe-Phe [84, 85]. The orientation of Phe-Phe is turned here in comparison to its orientation inside the Phe-Phe-chains. We assume that it is the fixed position of the third carboxylate group of TMA that acts as an adhesion point for the Phe-Phe molecules. The Phe-Phe molecules are supposed to interact via electrostatic attraction between a positively charged NH_3^+ group and the COO^- group of the neighboring molecule. This is the same interaction as was recently found by DFT, STM and XPS investigations for the Phe-Phe on Cu(110) [182], only in a rotated geometry. The phenyl-rings of the Phe-Phe molecules are oriented such that additionally mutual π - π -interaction might be possible.

As the structure forms readily upon annealing to 450 K, we can conclude that it indeed forms a lower energy phase than the individual small domains that exist at 400 K

or the unstable structures found at room temperature. An energetic advantage of this compact phase is that each TMA and each Phe-Phe molecule can form more bonds than in separated phases. Also the exact and self-chosen 1:1 stoichiometry is related to maximizing the overall number of bonds as only such a stoichiometric arrangement allows such this dense packing with a high number of bonds.

The employment of different intermolecular interactions (metal-carboxylate between TMAs, H-bonding between TMAs and Phe-Phes, electrostatic interaction among Phe-Phes) allows a good hierarchical separation of the sublattices. The use of the same type of bonding would probably lead to a much more complicated interplay of the molecular species. The detailed investigations of the TMA/Cu(110) and the Phe-Phe/Cu(110) systems have been a prerequisite for this structure analysis. On the other hand, we assume that these results can be generalized to other combinations of molecules with different individual properties. We think that it is thus in general possible to transfer the 3D chemical design methods for multi-component supramolecular structures to surfaces.

In conclusion, we have shown that it is possible to create a hierarchically structured 2D mixed compound using two different molecular linkers to incorporate two functional properties, namely enantio-pure chirality and metal-organic coordination. The resulting 2D patterns show unidirectional ordering which can be traced back to the anisotropic structure of the underlying Cu(110) surface. In spite of having two different molecules and Cu adatoms as constituents, just a rather simple phase was obtained instead of a complicated phase diagram. Apart from line defects, the patterns can grow in large homochiral domains up to full surface coverage. Finally, the observed structures are characterized by a self-chosen stoichiometry which greatly facilitates their growth.

Chapter 7

The Cu-O stripes: a self-organized nanotemplate

7.1 Structure of the Cu-Oxygen stripes

7.1.1 Introduction

The oxidation of Cu is a well known phenomenon in everyday life and is common to all Cu surfaces. The exposure of a Cu(110) surface to oxygen leads to the formation of a Cu-O surface adsorbate in a 1:1 stoichiometry. While it had been known since 1967 from LEED measurements by Ertl [184] that the adhesion structure of this pattern follows a (2×1) geometry, the final structure was only explained in 1990 [145] as being formed by alternating Cu and oxygen atoms which build rows along the $[001]$ direction (“added row structure”). As only every second lattice site along the $[\bar{1}\bar{1}0]$ direction is occupied, the effective lattice constant of the structure along the $[\bar{1}\bar{1}0]$ direction is $2 \cdot a_{[\bar{1}\bar{1}0]} = \sqrt{2}a_0 = 0.511$ nm. The structure of the (2×1) adhesion geometry can be seen from Figure 7.1a. A full surface coverage is reached for a nominal oxygen coverage of atomic oxygen Θ of just $\Theta = 0.5$. Such a coverage can be obtained by exposing the Cu(110) surface to about 10 Langmuirs (10 L) of molecular oxygen ¹ which splits into atomic oxygen for the Cu-O formation [185]. In our experiments significantly lower exposure times were only necessary for the structure formation. If oxygen is dosed for much longer exposures, a second phase with (6×2) superstructure is formed [145, 186].

In 1991, it was shown that the Cu-O structure was furthermore able to form a meso-

¹1 L is reached if the surface is exposed for a time t to an oxygen pressure p with $t \cdot p = 10^{-6}$ torr \cdot s.

scopic ordering if the oxygen surface coverage was lower than $\Theta = 0.5$. Using He-scattering and STM, it was found by Kern et al. [52] that the Cu-O rows group together to form Cu-O stripes, leaving in between areas of the bare Cu surface, see Figure 7.1b and c. This structure is formed for temperatures higher than 450 K either during growth or by post-annealing above this temperature. The growth can also be monitored in-situ e. g. by He-scattering [52] or by STM [187,188]. The annealing step was found to destroy the history of the surface preparation: the structure formed after annealing to 650 K or higher depends only on the oxygen coverage [185]. Similar 1D-structures were later reported also on other fcc (110) surfaces such as Ag(110) and Ni(110) [189–192].

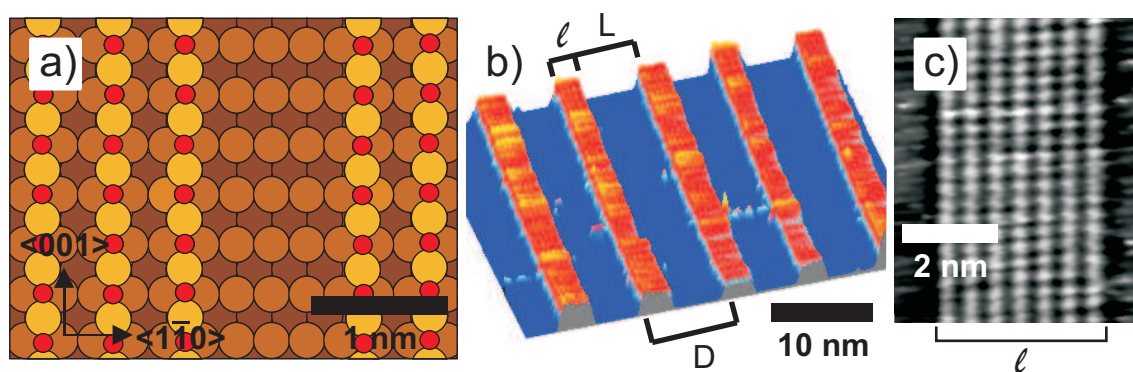


Figure 7.1: a) Schematic atomic structure of the Cu-O striped phase. On the left and on the right side of this image the Cu-O(2×1) phase is depicted. b) 3D STM image with enlarged z-scale of the Cu-O stripes (red) with definition of the stripe size l , the width L of the free Cu-surface area (blue) and the overall periodicity $D = l + L$. c) Atomically resolved Cu-O stripe.

7.1.2 The striped phase

More than 200 publications have been published since 1991 on these striped structures, several of them with the goal of explaining the origin of the structure. Nevertheless, it is possible to fully understand the structure formation using the initially proposed model [185,193] together with a new analysis in a full thermodynamic description [194].

The origin of the structure is based in the competition of two energies. First, there is the energy of forming a boundary between a (2×1) covered and a bare Cu substrate area. To minimize this boundary energy across the surface, large areas of Cu-O and Cu are preferred over small structures with more boundaries. The second energy arises from elastic strain that builds up in the Cu layers below the surface upon the formation of

the Cu-O rows on top of the surface. A slight mismatch of the Cu-O lattice with respect to the Cu(110) surface leads to atomic displacements in the bulk which create volumes of tensile and compressive stress. This stress extends deep into the substrate leading to atomic displacements well below the 20th atomic layer [194]. To lower the elastic energy, this strain has to be relaxed which is most efficiently achieved by alternating small Cu-O and bare substrate areas. The overall energy minimization balances both effects and thus creates the alternating 1D pattern. Its periodicity is large in comparison to the lattice constant, which allows to effectively describe the striped phase by a continuum model [185, 193]. There has been a long discussion on whether electrostatic forces that build up from atomic displacements could have a stronger effect than the strain itself [194]. In fact, the same continuum model would have been applicable also if electrostatic dipolar interactions had been the mechanism favoring small alternating domains, as these interactions have the same decay properties as the elastic forces. It was just recently shown that the effect of the electrostatic interaction is about one order of magnitude smaller than that of the elastic one [194].

Using the 1D continuum model of Zeppenfeld et al. [185, 193] basing on the work of Marchenko and Vanderbilt [195, 196] the equilibrium values for the periodicity D and the stripe width l can be deduced from the sole oxygen adsorbate coverage Θ [185, 193]:

$$l(\Theta) = \frac{\kappa\Theta}{\sin(\pi\Theta)} , \quad D(\Theta) \equiv l(\Theta) + L(\Theta) = \frac{\kappa}{\sin(\pi\Theta)} , \quad (7.1)$$

with $\kappa = 2\pi a_c \exp(1 + C_1/C_2)$ depending on the elastic material constants C_1 and C_2 and on a cutoff length a_c . In the original work κ was determined by fitting the theory to the experimental data with a fit resulting into $\kappa = 6.3$ nm. In a recent combined experimental and theoretical analysis [194], the values of C_1 and C_2 were independently calculated and a value of $a_c = 0.35 a_{[1\bar{1}0]}$ for a_c was determined from comparing X-Ray measurements and Quantum Monte Carlo calculations. This together results in $\kappa = 6.1$ nm.

In Figure 7.2a and b we show the dependence of the stripe periodicity and stripe width on the oxygen coverage as obtained from (7.1) for the more recent value of $\kappa = 6.1$ nm (the difference for these curves when using the original value is only marginal). Although this theory has been long published and has repeatedly been verified, still confusion exists about possible stripe size dependencies. For instance Otero et al. reported last year that “(...) increasing the temperature while keeping the exposure constant leads to an increase in the distance between the stripes, which also become broader, whereas increasing the exposure at the same temperature leads to narrower stripes.” [54]. The

experimental data points plotted in Figure 7.2 represent our own STM measurements of the stripe periodicity and stripe width. As STM is intrinsically a local technique the values for the periodicities and coverage have been determined locally, typically averaging over areas of about 50-200 nm. We plot data acquired for stripes with oxygen deposition at room temperature and post annealing to about 500 K (blue data points) and stripes grown directly at 650 K (orange data points), both of which fall on the same theoretical curve. Our experiments showed that the surface temperature has an influence on the oxygen surface coverage for a given exposure. This can be attributed to an effective sticking coefficient which we found to be higher by a factor of about 3 at 650 K in respect to room temperature. This increase can be explained by an activation energy necessary to split the molecular oxygen into atomic oxygen or by a higher mobility of the Cu adatoms at this temperature (see section 4.1.3) or by a combination of both. On the other hand, this influences only the exposure time necessary to reach a certain coverage. For each coverage value, the pattern as predicted by the theory is observed. Likewise, the dependence of the coverage on the oxygen partial pressure is not linear, which also can be described by a pressure dependent sticking coefficient only influencing the obtained coverage but not the pattern itself. Finally, it should be noted that upon higher annealing fewer deviations of the individual stripe width from the average value are found, as the obtained structures are closer to thermal equilibrium. For lower annealing temperatures this means that stripes and bare substrate areas with significant deviations from the average values are more often encountered. This reflects in the larger error bars as can be seen in blue data points in Figure 7.2.

One important result of the theory is that l and D are not independent. Instead, for each stripe size l (or for each bare Cu area of size L) only one corresponding D exists. The relative dependence of l and D is plotted in Figure 7.2c. From there it is also possible to see, that $\kappa = 6.1$ nm indeed gives a slightly better fit to our STM data points than $\kappa = 6.3$ nm, which further confirms the newest results [194]. When thinking of using the Cu-O stripes as a nanotemplate, this direct dependence of l and D can be seen as a drawback, as the parameters cannot be chosen independently. If a certain l - D combination is just needed locally at one position (e. g. for a test measurement) it is thus possible to form the stripes at lower temperatures ($450 \text{ K} < T < 650 \text{ K}$) to locally create larger variations of the individual stripe size and distance. A second possibility to slightly influence l without changing D is the following: as the chains are typically more kinked when grown at lower temperatures [197], a further exposure to some more oxygen

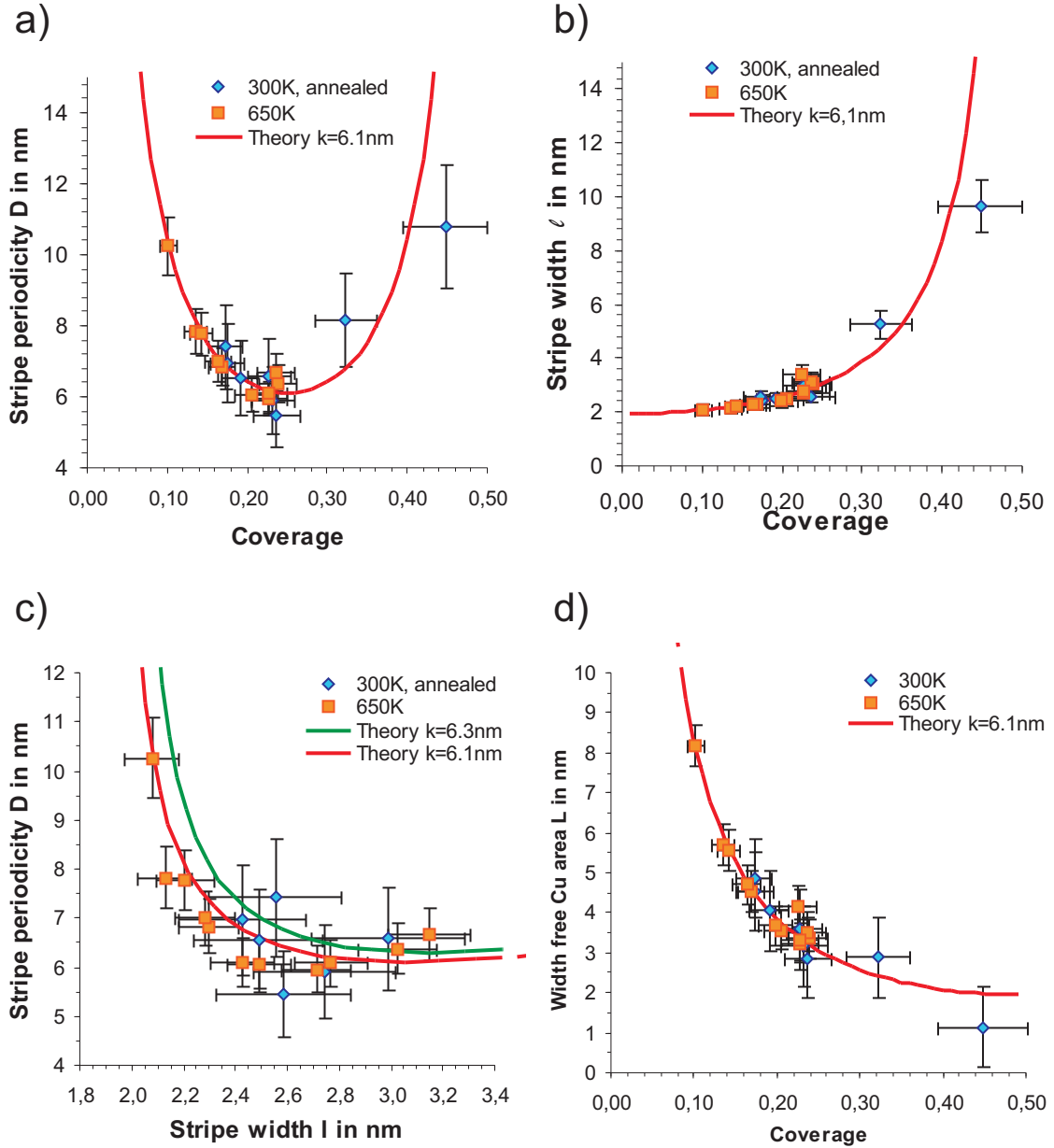


Figure 7.2: STM data of the structural properties of Cu-O stripes grown at 650 K (orange) and grown at 300 K (blue) with post-annealing to about 500 K. a) overall periodicity D ; b) stripe width l ; c) D and l in relation to each other, and d) width of the bare Cu-surface areas L . The plots a) and b) agree well with data-plots obtained by He-scattering [185]. Theoretical curves for $\kappa = 6.1$ nm (and $\kappa = 6.3$ nm in c) have been included in all graphs [193].

at lower temperatures after annealing can lead to a preferential attachment at the kink sites which locally can slightly widen the stripes while not changing their separation. A too heavy post-annealing exposure to oxygen at low temperatures will on the other hand also lead to the formation of new Cu-O islands in between the stripes and also strongly increase the number of kinks at the stripe edges.

For being able to use the Cu-O stripes as a nanotemplate the most important parameter is the size $L = D - l$ of the bare Cu areas since most molecular adhesion happens in between the stripes, as we will show in the following. In Figure 7.2d we thus plot the dependence of L on the coverage Θ . Ideally, one would like to have an L matching to the molecular adsorbate and between a not too large l . As can be seen from comparing Figure 7.2b and d, the Cu-O stripes are most effective for molecular sizes above 2 nm as shorter sizes of L can only be reached at relatively high oxygen coverages ($\Theta = 0.5$ corresponds to full surface coverage) and correspondingly large stripe sizes l .

7.2 The Cu-O stripes as nanotemplate

The possibility to use the Cu-O striped phase as nanotemplate has been tested before for C_{60} [53] and for the so called “Lander” molecules ($C_{90}H_{98}$) [54] which were both found to adsorb only on the bare Cu surface areas. It was thus concluded that the Cu-O striped phase can act as a template or a nanograting. As both molecules lack strongly interacting functional groups, the study of other types of molecules is necessary in order to extend these results to a larger class of possible adsorbates.

7.2.1 TMA on the Cu-O striped phase

After creating the Cu-O stripes on the Cu(110) surface, we have mainly found in the bare Cu substrate regions. Nevertheless, a small fraction of the TMA molecules is also found on top of the Cu-O stripes. Some TMA molecules are also within Cu-O stripes at places where Cu and oxygen atoms have been removed.

A mild annealing of a few 10 K above the deposition temperature is enough to remove all TMA molecules from the top of the Cu-O stripes. The ordering of the TMA molecules in between the stripes is improved and chains are formed along the $[1\bar{1}0]$ direction similar to what was observed on the pristine Cu(110) surface (see Figure 7.3a). The difference is that the $(\text{Cu-TMA-Cu})_n$ -chains have now a fixed maximum length defined by the width

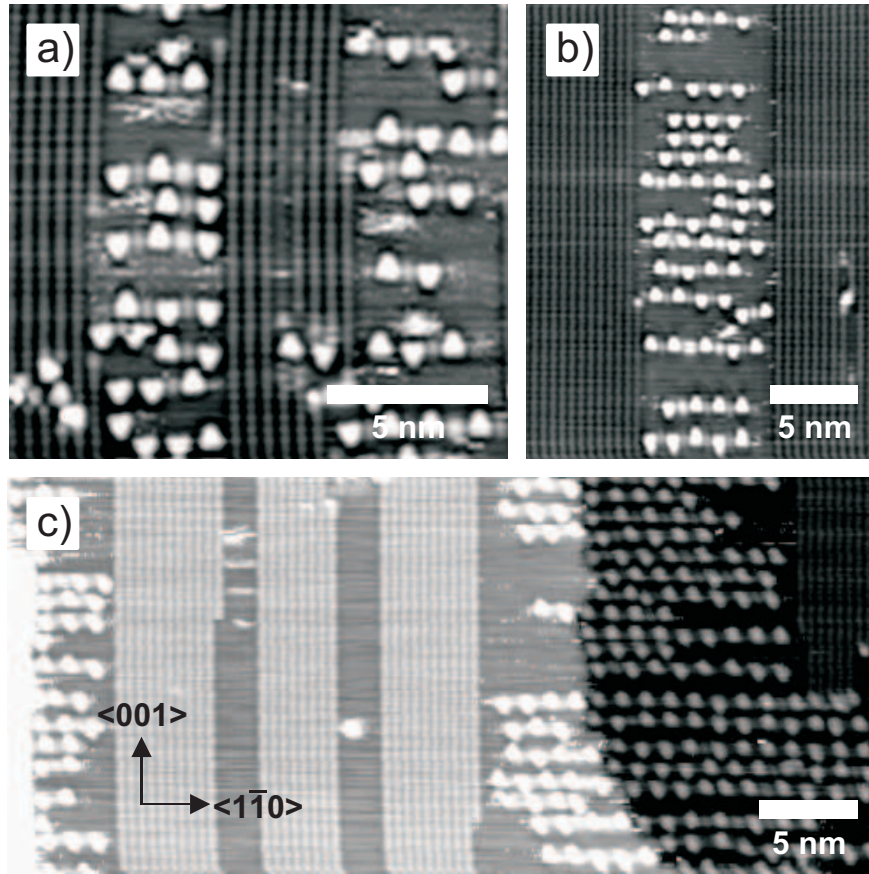


Figure 7.3: a) TMA deposited on the Cu-O striped phase. b)-c) The same surface after annealing to 560 K .

L of the bare Cu surface areas and that this length can be varied according to (7.1) as shown in Figure 7.2).

It should be noted that the periodicity of the TMA chains within the striped phase differs more often from the ideal value of 5 Cu lattice spacings than on the pristine surface. Especially chains of periodicity 6 and 4 are often observed (each about 15-20% of all segments). The reason for this non-stoichiometric behavior is probably that both the Cu adatoms and the TMA molecules can only explore a small fraction of the surface. The “communication” between TMA and Cu is thus limited. As a consequence, not always the ideally matching bonding partner is available and self-correction is less efficient.

Both for the as-deposited as well as for the slightly annealed phase a considerable number of TMA molecules is also found within the stripes at positions where the usual Cu-O structure has been locally removed (see Figure 7.3a). We have performed measure-

ments of TMA on a fully covered Cu(110)-(2×1)O surface to further test this behavior. No ordered structure of the TMA was observed there. Poor scanning conditions were observed on the full covered Cu(110)-(2×1)O testifying movable or even mobile TMA molecules. Nevertheless, at room temperature some structures are observed which are identified as TMA molecules which have moved to the substrate surface under displacement of Cu-O segments. By annealing the full covered Cu(110)-(2×1)O to 380 K and 430 K an increasing number of these structures is found and at 480 K all TMA molecules are found in the first layer which furthermore seem to form closed-packed islands within the Cu-O. A similar effect was also observed for C₆₀ [53]. These results show the potential of the TMA to change the Cu-O structure.

For the striped phase, it is likewise often observed that (Cu-TMA-Cu)_n-chains interrupt rows of Cu-O. In extreme cases TMA chains seem to consume parts of stripes or whole stripes. We have also performed corresponding measurements for TPA on the striped phase where we find that the tendency to destroy the stripe pattern is even higher.

These results suggest that there is a competition between the metal-organic coordination chains and the Cu-O structures. A strong annealing of TMA on the striped phase was used to further clarify the influences of this competition. Figure 7.3b shows a structure which has been annealed to 560 K. The phase boundaries are clearer (less kinks in the Cu-O stripes) and inclusions of TMA molecules within stripes are less frequent. Areas like these are nice examples of local ordering. However, large areas of Cu-O stripes without molecules as well as regions where only (Cu-TMA-Cu)_n-chains exist are observed on the same sample, indicating that a partial phase separation is occurring for this annealing temperature. We notice that, as the Cu-O stripes are formed at 450 K or higher, it is not surprising that the even higher temperature of 560 K is enough to introduce a surface reordering. This also demonstrates that it is not possible to first form the stripes, then deposit the TMA molecules and then strongly anneal the whole structure in order to create a more regular pattern.

One reason for the phase separation at high temperatures could be represented by stress. In principle it is possible that the stress release created by the Cu-O stripes is less effective on a surface area which – instead of being bare – is covered by (Cu-TMA-Cu)_n-chains. Also the chains themselves can introduce extra stress to the substrate. Anyway, as we have no specific indication for a significant influence of stress, we believe that another effect is more important: both structures – Cu-O stripes and metal-organic

networks – need Cu adatoms to form. One of the structures can thus grow by taking adatoms from the other. Furthermore, as the preferential growth direction is orthogonal for the two structures, they can penetrate into and even destroy each other. At room temperature, this can be seen as the reason for the inclusions of TMA in the Cu-O stripes. This consumption of stripe parts will depend on the energy balance and on the kinetics, i. e. finally on the surface temperature. For TPA, the activation may be slightly lower as for TMA since, also on the bare substrate, TPA is found to form perfectly ordered structures at lower temperatures than TMA. As the Cu-O stripes have been grown first, it is natural to observe mainly metal-organic chains destroying Cu-O stripes and not vice versa. At high temperatures, one can expect that this process of consumption can happen mutually (Cu-O stripes destroying MOCCs and vice versa). Due to the perpendicular growth directions, chains and stripes will strongly interfere. In order to minimize costly and complicated phase boundaries, the most stable situation is one in which the two phases are separated.

7.2.2 Phe-Phe on the Cu-O striped phase

As a further test molecule, we have used the L-Phe-L-Phe dipeptide, introduced in chapter 6. The L-Phe-L-Phe molecule was deposited onto the striped phase at room temperature. As can be seen from Figure 7.4, Phe-Phe can form chains which are oriented along the Cu-O stripes. The individual molecular orientation as well as the chain direction is significantly different from what was observed for the L-Phe-L-Phe on the pristine Cu(110) surface or upon co-deposition with TMA (see section 6.2). The chain direction is indeed oriented along the [001] direction, parallel to the Cu-O stripes. One side of the molecular chain is in close contact with the Cu-O stripes, signifying that a significant interaction between the stripes and the molecular chains exists.

From the STM measurements we can neither determine the detailed adhesion geometry nor the interaction mechanisms along the molecular chain and with the Cu-O stripes. Nevertheless, the STM images provide strong indications on where the electron-rich phenyl rings and the functional backbone are located. From the well-known structure of the Cu-O stripes which indicate the substrate sites, we can build a tentative model displayed in Figure 7.4b.

For the intermolecular interaction we can exclude electrostatic interactions between amino and carboxylate groups as were found for Phe-Phe on pristine Cu(110) (see chap-

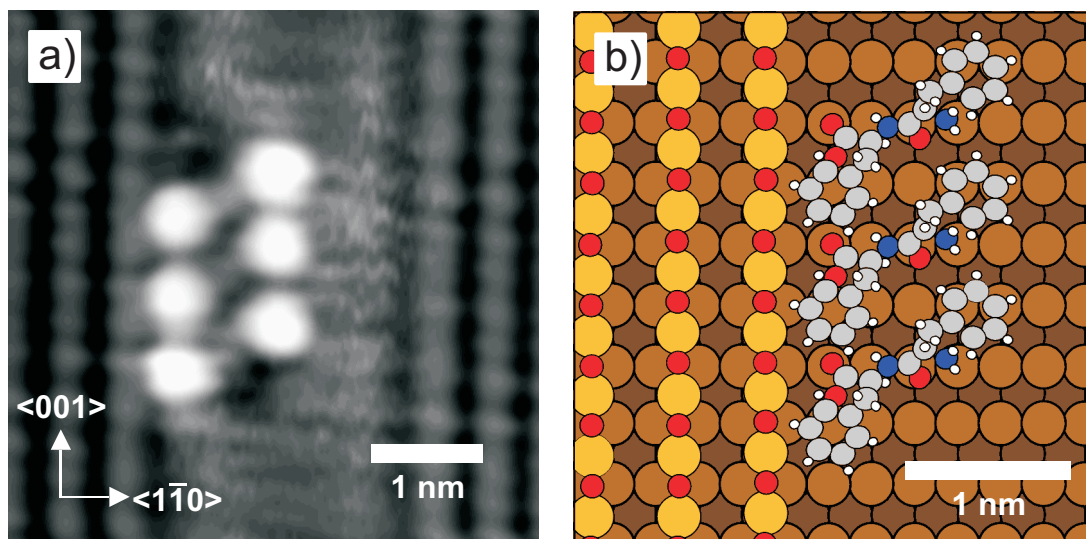


Figure 7.4: *L-Phe-L-Phe* molecules at *Cu-O* stripes. a) STM image and b) proposed atomic model.

ter 6). On the other hand, the molecules group such that a π - π -interaction between the phenyl groups of neighboring molecules is possible. This interaction is then probably responsible for the chain formation. We expect the individual Phe-Phe molecule to bind to the substrate mainly with the carboxylate group and possibly also with the amino and the carbonyl group. For the interaction between the molecules and the *Cu-O* rows, we assume attractive electrostatic interactions between the positively polarized hydrogen atoms of the phenyl group and the negatively polarized oxygens within the *Cu-O* rows, similarly to what was introduced in chapter 6 for the TMA-Phe-Phe structures. It is also possible that extra adatoms are present close to the *Cu*-carboxylate group, further increasing the bonding to the substrate or indirectly to the *Cu-O* stripe. Nevertheless, this assumption cannot be finally tested on the basis of the sole STM measurements. As can be seen from Figure 7.5a, single *Cu-O* rows can occasionally be found also on the other side of the *L-Phe-L-Phe* molecule, showing the attractive interaction between the rows and the Phe-Phe.

If the coverage of *L-Phe-L-Phe* is increased, *L-Phe-L-Phe* chains in their “normal” $[1\bar{1}2]$ orientation are also found on the bare *Cu* surface areas, provided that these areas are large enough. If the coverage exceeds the limit up to which bare *Cu* surface areas can be filled, the growth of a second layer starts. This second layer nearly exclusively forms on top of the first Phe-Phe layer, i. e. only in regions corresponding to the former bare

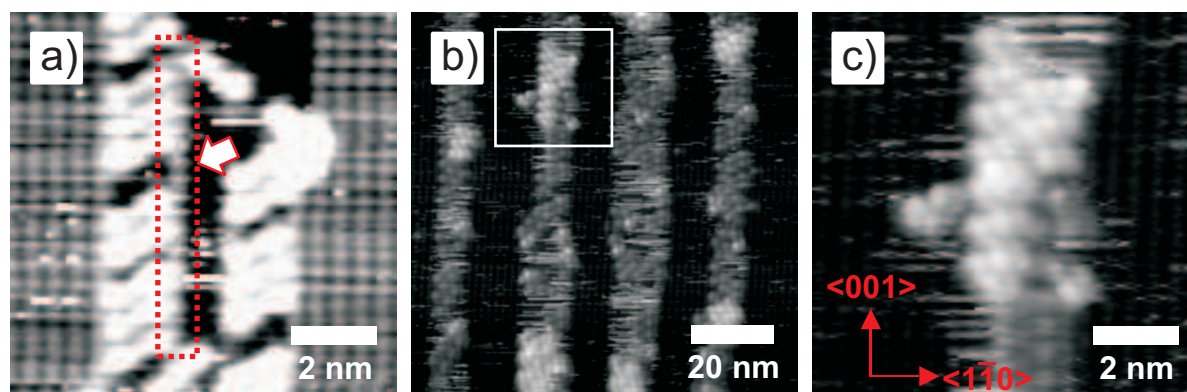


Figure 7.5: a) *L-Phe-L-Phe* molecules in between *Cu-O* stripes. An extra single *Cu-O* row is visible at the arrow. b) Coverage of *Phe-Phe* exceeding the free area between the *Cu-O* stripes. A second layer is only found on top of the first layer of *Phe-Phe*. c) Enlarged view of b). Also the second layer is partially ordered.

Cu surface areas. As can be seen from Figure 7.5b and c the second layer also has some partial ordering which again leads to the formation of chains of *Phe-Phe* molecules. This demonstrates that the *Cu-O* pattern is indeed able to structure the adhesion of *Phe-Phe* not only within the first but also within the second layer.

7.2.3 Discussion of the templation efficiency

By comparing the results obtained here for the supramolecular self-organization of TMA and *L-Phe-L-Phe* with the work reported before on C_{60} and the Lander molecule [53,54], we can conclude that the *Cu-O* stripes represent a good nanotemplate as long as no strong competition for adatoms or surface areas exists.

The *Cu-O* stripes can be used to template the growth of limited chain length for TMA but a much better ordering is observed for *Phe-Phe* and the Lander molecules. Both TMA and oxygen interact with the surface in a very similar way, as both bind to the substrate (partially) via Cu adatoms. This similar interaction scheme results in a competitive situation, a “race” for adatoms. This competition is most probably the origin for the poor ordering at high temperatures. The situation can be compared to the case in which Cu atoms deposited onto existing Ag-O-strips on Ag(110) replace Ag atoms in the stripes and form *Cu-O* stripes on Ag(110) [191,192].

For *Phe-Phe* and the Lander molecules different interactions constitute the supramolecular structures. There, the ordering was found to work efficiently. A first

rule of thumb could thus be, not to mix such entities of similar properties as nanotemplate and adsorbate. On the other hand, C_{60} was occasionally found to “dig” itself into existing stripes [53] as we found it for TMA showing that the situation is in general more complex.

As we have shown in Figure 7.2d, the bare Cu-surface areas provided by the Cu-O stripes range from slightly below 2 nm easily up to 20 nm or more in size. The adsorbate molecules used here are thus in principle too small to exploit the full potential of the Cu-O stripes. The ideal adsorbate for the Cu-O stripes nanotemplate is larger and interacts only slightly with the surface. In this sense, Cu-O stripes are ideal candidates for ordering the adsorption of larger macro- or bio-molecules. So far, however, it is not possible to investigate such large molecules on this surface as on the one hand the molecules cannot be evaporated in UHV and on the other hand the Cu(110) surface cannot be exposed to oxygen pressures even far below those of ambient conditions without being fully oxidized. With the availability of new deposition mechanisms under UHV conditions such as the electrospray-ionization system which is under construction and close to first application in our neighboring laboratory, this problem could be solved. We thus expect that the Cu-O striped phase will provide a useful and flexible nanotemplate for a new class of adsorbate molecules in the near future. The analysis of the smaller molecules within this nanotemplate as presented here may thus be seen as a first step towards a further use of this nanotemplate for the study of larger biological molecules. The efficient ordering of Phe-Phe molecules by the Cu-O stripes allows to hope that other biologically relevant molecules may behave similarly on this nanotemplate.

Chapter 8

Conclusions and Perspectives

In the present work the ordering of organic molecules by means of surface templation has been investigated. The growth of metal-organic coordination networks has been steered to yield 1D metal-organic coordination chains (MOCCs). This method has been shown to work both for intrinsic and extrinsic MOCCs. The structure of these chains has been analyzed using a variety of experimental and theoretical methods to understand the intermolecular and molecule-surface interaction. The bonding structure was resolved for the first time for surface metal-organic coordination networks (MOCNs) in detail from a combined experimental and theoretical viewpoint. One of the results is the explanation of the different supramolecular structures for extrinsic Fe- and intrinsic Cu-TMA chains in terms of the underlying electronic structure. The stronger depletion of the *s*-states of Fe leads to a higher coordination of the Fe inside the chains in respect to the Cu. This preferential *s*-depletion of Fe can not only be used to explain the different observed structures, it also retains and even slightly increases the partial filling of the *d*-states of Fe. This allows to predict a non-quenched spin moment for the Fe atoms. The results are a first step towards a potential use of magnetic MOCCs in the study of 1D magnetic effects.

In order to investigate the ordering of larger organic molecules, an analysis of Phe-Phe has been carried out on Cu(110) and has been compared to results on Cu(100). Also here, chains are found, but they originate from an intrinsic bonding preference in the intermolecular interaction rather than from the surface anisotropy. From the comparison it was shown that the substrate decides on the growth direction and the number of equivalent chain directions and thus can support the chain formation but can not dictate it. The commensurability of the substrate periodicity and adsorbate was

identified as the critical parameter governing the direction of the chain growth.

Self-organized Cu-O stripes have been investigated as an example of a larger and adjustable nanotemplate. It was shown that it is indeed possible to structure the adsorption of Phe-Phe using this nanotemplate. For TMA a double templating effect was observed. The anisotropy of Cu(110) is still translated to a monodisperse chain growth. Furthermore, chains were created only on the bare Cu surface areas which permits to control the length of the MOCCs. The ordering by the Cu-O stripes was limited due to a competition for adatoms resulting in a phase separation of $(\text{Cu-TMA-Cu})_n$ and Cu-O upon annealing. On the other hand, the templation of Phe-Phe using the Cu-O nanotemplate was found to work in a reliable and effective way, and no competition was observed here.

Finally, the combined adhesion of TMA and Phe-Phe on Cu(110) has allowed to create MOCNs in single chiral form. A hierarchical structure formation was observed which in connection with the anisotropic Cu(110) surface led to a simple phase diagram and a highly ordered 2D structure. This result exemplarily shows that it is possible to incorporate two different properties, namely chirality and metal-organic coordination by using two specialized molecules, each of which is responsible for one of the two properties.

From the comparison of these individual results with each other and with literature data [24, 40, 43, 45, 53, 54, 126] one can conclude that the ordering ability of a surface strongly depends on the size of the adsorbate. When using anisotropic surfaces for templation, the size dependence is best expressed in the form of commensurability of adsorbate and substrate. For atoms as adsorbate, this commensurability can straightforwardly be expressed e. g. in terms of lattice mismatch. For molecules, the situation is more complex, as molecules have an internal structure and can change their commensurability by rotation but also by internal conformational changes, as happens in the case of Phe-Phe [182]. TMA fits extremely well to the Cu(110) surface periodicity along $[1\bar{1}0]$ while it does not fit at all along the $[001]$ direction. This difference explains, why the growth mode is 1D and not 2D. The fact that the commensurability along $[1\bar{1}0]$ is so good that the MOCC-S structure is practically stress-free, further explains why these chains can grow without detectable size limitations. For Phe-Phe, on the other hand, the driving mechanism for 1D growth is the intrinsically linear intermolecular interaction and not the surface structure. A specific ideal intermolecular distance thus already exists and its commensurability to the atomic distances of the substrate dictates the actual chain growth. The substrate acts as a supplier of bonding sites and by its symmetry defines

the number of equivalent growth directions. Its ordering here is thus only a second order templating effect.

Another important parameter is the relative strength of the intermolecular and the molecule-substrate interaction. For the Phe-Phe the single surface bond is in competition with the intermolecular bond. The Cu-O rows show an additional interaction with the Phe-Phe molecules which overall allow an effective ordering along the [001]-stripe side. On the other hand, a too strong interaction is also unfavorable, as can clearly be seen from the case of TMA and C₆₀ [53] on Cu-O stripes. When moving to larger molecules, we expect the Cu-O-stripes to be in general a good template both in terms of length scales and bonding strength to the substrate as well as possible interaction with the adsorbate.

It should be noted also that the stability of nanotemplates is limited. Nanotemplates which rely on bare surface structures such as (110), higher index surfaces, or vicinal surfaces [40] are of a more robust type than self-organized nanotemplates as the Cu-O striped phase. On the other hand, those more robust surfaces lack the possibility to tune the structural sizes by self-organization. Furthermore, also bare surfaces can undergo processes of reconstruction, faceting or step bunching.

In the TMA-Phe-Phe/Cu(110) system the interaction of a first adsorbate (TMA) can strongly influence that of a second one (Phe-Phe) but this is not a templated adhesion as a fully mixed adsorbate layer is formed. It is thus possible to span a spectrum from the case of robust systems (bare surfaces as e. g. Cu(110)) over the case of firmly attached adsorbates which can act as tunable nanotemplates (e. g. the Cu-O stripes) to more weakly attached adsorbates which then intermix with other later deposited adsorbates.

Focussing on the MOCCs, we expect, that the method introduced here to create 1D metal-organic chains is not limited to the Cu(110) surface but can at least be generalized to other (110) surfaces. Of course, it is necessary to secure the adatom supply e. g. by codeposition [124]. The advantage of changing the surface is that the lattice constant and the electronic properties of the substrate can be actively varied. This is important, especially for possible magnetic properties. If it will turn out, that also a net orbital moment also exists in the metal-organic coordination chains, collective phenomena can be expected only if an interspin coupling e. g. via the substrate *d*-states is achieved. As discussed in chapter 5 an exchange mechanism might depend on the substrate material and on the distance of the spin centers. It would be thus necessary to be able to vary both the electronic structure of the substrate and the size of the organic linker molecules. A

huge range of different carboxylic acids exists, which could be used as linkers of different size, including e. g. oxalic and fumaric acid. Due to the need for commensurability, though, changing the organic linker would possibly also require to change the substrate to maintain an ordered growth.

Furthermore, in order to conserve also the 1D geometry and avoid the formation of compact islands as in the case of TPA/Cu(110), growth in the direction perpendicular to the chain has to be prevented. This may be achieved by incorporating a spacer group to the organic linker molecule as it was provided by the third carboxylate group of TMA. On the other hand, when using organic linkers smaller than TMA such a design is probably not a realistic option. Alternatively, a tuning of the surface periodicity in the direction perpendicular to the chain growth might prevent interaction and growth in this direction. While the size relations on an unmodified fcc (110) surface are fixed, the employment of a reconstructed (110) surface might allow to sufficiently separate the metal-organic coordination chains.

A further potential application for MOCCs is the investigation of catalysis. It has been shown that low-coordinated metal atoms can be particularly catalytically active [198–201]. The metal centers in MOCCs constitute low coordinated metal atoms that, unlike adatoms, are fixed in position and thus constitute well defined and individually addressable study objects. Furthermore, the intermetallic spacings and the electronic filling level can be changed by means of the organic linker molecules. The possibility to incorporate chirality into the MOCNs by adding molecules of selectable chiral configuration may allow the analysis of enantioselective catalytic processes.

Finally, we would like to note two side-results of this work, which while not being of central importance for the scope of this work might also have further implications. Firstly, both TMA and Phe-Phe have been found to exhibit similar chain length distributions in terms of elastic growth theory. These results are consistent to each other but the obtained curves for the chain length distributions are in disagreement with theory especially concerning the maximum of the distribution. We assume, that some phenomena within the growth are not yet well reflected in the corresponding theory. It is still an open question, how this discrepancy will be solved. We hope that further theoretical simulations will allow a better understanding of this point.

Secondly, the result that single Cu adatoms are not visible both in simulated and measured STM images when attached to a TMA-molecule might have a strong impact also on other structures, particularly when carboxyl- or nitro-groups are involved. We

assume that more molecular structures exist (especially those for which the adhesion geometry has never been explained in a satisfying way) where extra adatoms play a significant role in the structure formation. As the adatom density is closely linked to the surface chemistry and geometry this argumentation should not be easily generalized beyond Cu surfaces. Nevertheless, a potential reason, why so many studies have been successful in creating extended structures on Cu(110) [75] could be linked to the high availability of adatoms on Cu(110) for deprotonation but also for complexation.

Abbreviations and Common Symbols

Abbreviations

0D, 1D, 2D, 3D	Zero-, One-, Two-, Three-Dimensional
DFT	Density Functional Theory
GGA	Generalized Gradient Approximation
HOMO	Highest Occupied Molecular Orbital
HOPG	Highly Oriented Pyrolytic Graphite
IR	Infra Red
LEED	Low Energy Electron Diffraction
LUMO	Lowest Unoccupied Molecular Orbital
MBE	Molecular Beam Epitaxy
MF	Mean-Field
ML	Monolayer
MOCC	Metal-organic coordination chain
MOCC-S	TMA-Cu single chain
MOCC-D	TMA-Cu double chain
MOCC-T	TMA-Cu chains in transition phase
MOCC-Fe	TMA-Fe single chains
MOCN	Metal-organic coordination network
NEXAFS	Near Edge Photoelectron Absorption Fine-Structure
OMBE	Organic Molecular Beam Epitaxy
QMC	Quantum Monte-Carlo
RAIRS	Reflection Absorption Infrared Spectroscopy
RAS	Reflection Anisotropy Spectroscopy
RE	Rate Equations
STM	Scanning Tunneling Microscopy
STS	Scanning Tunneling Spectroscopy
TMA	1,3,5 Benzenetricarboxylic acid, trimesic acid
TMLA	1,2,4 Benzenetricarboxylic acid, trimellitic acid
TPA	1,4 Benzenedicarboxylic acid, terephthalic acid
UHV	Ultra-High Vacuum
XPS	X-ray Photoelectron Spectroscopy

Common Symbols

a_0	lattice constant of Cu, $a_0=3,615\text{\AA}$
D	periodicity of Cu-O stripes
dI/dV	differential conductance
E	energy with respect to the Fermi energy
e	electronic charge, $e = -1.6 \cdot 10^{-19} \text{ C}$
E_F	equilibrium Fermi energy
$f(E, T)$	equilibrium Fermi function
h	hollow site
k_B	Boltzmann constant, $k_B = 0.0862 \text{ meV/K} = 1 \text{ eV}/11604 \text{ K}$
L	width of bare Cu surface areas between Cu-O stripes
l	stripe width for Cu-O stripes
lb	long-bridge site
m_e	free electron mass, $m_e = 9.1 \cdot 10^{-31} \text{ kg}$
m^*	effective electron mass
n	electron density
s	tip-sample distance
sb	short-bridge site
T	temperature
t	top site
U	external potential energy
V	electric potential of sample with respect to tip
W	work function
z	tip height

Non-SI-units

L	(Langmuir) unit of exposure, $1 \text{ L} = 10^{-6} \text{ torr} \cdot \text{s}$
torr	pressure unit (mm Hg), $1 \text{ torr} = 133,322 \text{ Pa} = 1,33322 \text{ mbar}$

List of Figures

2.1	STM Tunneling scheme	8
2.2	Principle of RAIRS	11
2.3	STM-Setup	17
3.1	New sample holder	25
3.2	Performance of the new sample holder, TMA/Ag(100)	28
4.1	Synthons and 3D MOCN	30
4.2	2D MOCN on Cu(100)	32
4.3	Cu(110) surface and TMA	34
4.4	TMA/Ag(100)	35
4.5	TMA/Cu(110) deposited at 130 K	36
4.6	RAIRS of TMA/Cu(110) at 85 K	38
4.7	TMA/Cu(110) deposited at 250 K	40
4.8	Ir spectra as deposited at 250 K plus annealing	42
4.9	TMA/Cu(110) created around room temperature	44
4.10	Increasing Coverage of TMA/Cu(110)	45
4.11	RAIRS TMA/Cu(110) at 300 K	46
4.12	Chain length distribution for TMA	48
4.13	Submonolayer Growth Model	49
4.14	MOCN-1: (Cu-TMA-Cu) _n -chains	51
4.15	LEED MOCC-S	52
4.16	High symmetry sites on Cu(110)	54
4.17	Low-Temperature Manipulation	56
4.18	DFT: Atom positions and simulated STM of MOCC-S	59
4.19	STS of TMA/Cu(110)	61
4.20	Density of States of MOCC-S	62

4.21	STM and LEED of (4×4)	66
4.22	Intermediate TMA coverage regime	67
4.23	IR measurement of TMA adsorbed at 470 K	69
4.24	Energy scheme in phase transition	71
4.25	TPA on Cu(110)	73
5.1	MOCC-Fe chains on Cu(110).	79
5.2	Number of Fe chains	80
5.3	Comparison of DFT and STM of MOCC-Fe	81
5.4	Spin-polarized calculation of MOCC-Fe	83
6.1	Phe-Phe-Molecule	88
6.2	Phe-Phe on Cu(110)	90
6.3	Phe-Phe on Cu(100)	92
6.4	Length distribution of Phe-Phe chains	93
6.5	Growth of TMA-Phe-Phe islands	99
6.6	TMA-Phe-Phe structure	100
6.7	Model TMA-Phe-Phe	100
7.1	Structure of the Cu-O stripes	104
7.2	Periodicities and sizes of the Cu-O stripe phase	107
7.3	TMA on the Cu-O striped phase	109
7.4	L-Phe-L-Phe molecules at Cu-O stripes	112
7.5	Phe-Phe Multilayer in between of Cu-O stripes	113

List of Tables

2.1	STS Parameter	20
2.2	OMBE Parameter	21
4.1	IR Modes	39
4.2	Orientation of neighboring TMAs	53
6.1	Cu-Cu-spacings on Cu(110)	95

Bibliography

- [1] M. Jeong *et al.*, Science **306**, 2057 (2004).
- [2] D. A. Thomson and B. J. S., IBM J. Res. Dev. **3**, 311 (2000).
- [3] U. Landman, <http://www.physorg.com/news3087.html>.
- [4] D. Normile, Science **293**, 787 (2003).
- [5] N. Mathur, Nature **419**, 573 (2002).
- [6] C. Vieu *et al.*, Appl. Surf. Sci. **164**, 111 (2000).
- [7] M. F. Crommie, C. P. Lutz, and D. M. Eigler, Science **262**, 218 (1993).
- [8] T. Ito and S. Okazaki, Nature **406**, 1027 (2000).
- [9] J. V. Barth, G. Costantini, and K. Kern, Nature **437**, 671 (2005).
- [10] F. Rosei *et al.*, Progr. Surf. Sci. **71**, 95 (2003).
- [11] J. V. Barth, Surf. Sci. Rep. **40**, 75 (2000).
- [12] G. F. Swiegers and T. J. Malefetse, Chem. Rev. **100**, 3483 (2000).
- [13] O. M. Yaghi *et al.*, Nature **423**, 705 (2003).
- [14] S. Kitagawa, R. Kitaura, and S. Noro, Angew. Chem. Int. Ed. **43**, 2334 (2004).
- [15] M. Ruben, Angew. Chem. Int. Ed. **44**, 1594 (2005).
- [16] J.-M. Lehn, in *Supramolecular chemistry* (VCH, Weinheim, 1995), Chap. 9, p. 200.
- [17] J.-M. Lehn, PNAS **99**, 4763 (2002).
- [18] M. Ruben *et al.*, Angew. Chem. Int. Ed. **43**, 3644 (2004).

- [19] T. Yokoyama *et al.*, Nature **413**, 619 (2001).
- [20] B. Dwir *et al.*, Microel. Eng. **35**, 269 (1997).
- [21] H. Heidemeyer, U. Denker, C. Müller, and O. G. Schmidt, Phys. Rev. Lett. **91**, 196103 (2003).
- [22] H. Röder *et al.*, Nature **366**, 141 (1993).
- [23] Y. Li *et al.*, Phys. Rev. B **56**, 12539 (1997).
- [24] L. P. Nielsen *et al.*, Phys. Rev. Lett. **71**, 754 (1993).
- [25] C. Polop *et al.*, Phys. Rev. B **63**, 115414 (2001).
- [26] N. W. E. Kampshoff and K. Kern, Surf. Sci. **406**, 103 (1998).
- [27] S. Lukas, G. Witte, and C. Wöll, Phys. Rev. Lett. **88**, 028301 (2002).
- [28] G. P. Lopinski, D. D. M. Wayner, and R. A. Wolkow, Nature **406**, 48 (2000).
- [29] J. Weckesser *et al.*, J. Chem. Phys. **115**, 9001 (2001).
- [30] G. Koller, S. Surney, F. P. Netzer, and M. G. Ramsey, Surf. Sci. **504**, 11 (2002).
- [31] P. W. Murray, I. M. Brookes, S. A. Haycock, and G. Thornton, Phys. Rev. Lett. **80**, 988 (1998).
- [32] A. Kühnle *et al.*, Phys. Rev. Lett. **93**, 086101 (2004).
- [33] J. Jia *et al.*, Appl. Phys. Lett. **80**, 3186 (2002).
- [34] J. L. McChesney, J. N. Crain, F. J. Himpsel, and R. Bennewitz, Phys. Rev. B **72**, 035446 (2005).
- [35] J. V. Barth, H. Brune, G. Ertl, and R. J. Behm, Phys. Rev. B **42**, 9307 (1990).
- [36] M. Böhrringer *et al.*, Phys. Rev. Lett. **83**, 324 (1999).
- [37] M. Böhrringer, K. Morgenstern, W. D. Schneider, and R. Berndt, J. Phys. Condens. Mat. **11**, 9871 (1999).
- [38] S. Clair *et al.* (unpublished).

- [39] S. Clair *et al.*, J. Phys. Chem. B **108**, 14585 (2004).
- [40] P. Gambardella *et al.*, Nature **416**, 301 (2002).
- [41] P. Gambardella *et al.*, Phys. Rev. B **61**, 2254 (2000).
- [42] P. Gambardella *et al.*, Phys. Rev. Lett. **93**, 077203 (2004).
- [43] A. Kirakosian *et al.*, Appl. Phys. Lett. **79**, 1608 (2001).
- [44] J. N. Crain *et al.*, Phys. Rev. B **69**, 125401 (2004).
- [45] V. Repain, G. Baudot, H. Ellmer, and S. Rousset, Europhys. Lett. **58**, 730 (2002).
- [46] V. Repain, J. M. Berroir, S. Rousset, and J. Lecoer, Europhys. Lett. **47**, 435 (1999).
- [47] S. Rousset *et al.*, Surf. Sci. **422**, 33 (1999).
- [48] H. Brune, M. Giovannini, K. Bromann, and K. Kern, Nature **384**, 451 (1998).
- [49] H. Brune, Surf. Sci. Rep. **31**, 121 (1998).
- [50] S. Rusponi *et al.*, Nature Mater. **2**, 546 (2003).
- [51] M. Corso *et al.*, Science **303**, 217 (2004).
- [52] K. Kern *et al.*, Phys. Rev. Lett. **67**, 855 (1991).
- [53] M. Pedersen *et al.*, Surf. Sci. **389**, 300 (1997).
- [54] R. Otero *et al.*, Angew. Chem. Int. Ed. **43**, 2091 (2004).
- [55] F. M. Leibsle, C. F. J. Flipse, and W. A. Robinson, Phys. Rev. B **47**, 15865 (1993).
- [56] H. Ellmer *et al.*, Surf. Sci. **476**, 95 (2001).
- [57] G. Binnig and Rohrer, Rev. Mod. Phys. **59**, 615 (1987).
- [58] J. Tersoff and N. D. Lang, in *Theory of scanning tunneling microscopy* (Academic Press, Boston, 1993), p. 1.
- [59] J. Tersoff and D. R. Hamann, Phys. Rev. Lett. **50**, 1998 (1983).
- [60] J. Bardeen, Phys. Rev. Lett **6**, 57 (1961).

- [61] N. D. Lang, Phys. Rev. B **34**, 5947 (1986).
- [62] C. J. Chen, Phys. Rev. Lett. **69**, 1656 (1992).
- [63] C. J. Chen, J. Vac. Sci. Technol. B **12**, 2193 (1994).
- [64] J. V. Barth, H. Brune, and G. Ertl, Phys. Rev. B **42**, 9307 (1990).
- [65] W. Ho, J. Chem. Phys. **117**, 11033 (2002).
- [66] J. Nieminen, S. Lahti, S. Paavilainen, and K. Morgenstern, Phys. Rev. B **66**, 165421 (2002).
- [67] P. Wahl, private communication, 2005.
- [68] P. Wahl, Ph.D. thesis, Universität Konstanz, 2005.
- [69] V. A. Ukraintsev, Phys. Rev. B **53**, 11176 (1996).
- [70] H. Haken and H. C. Wolf, *Molecular Physics and Elements of Quantum Chemistry* (Springer, Berlin, 2004).
- [71] V. G. Bordo and H.-G. Rubahn, *Optics and Spectroscopy at Surfaces and Interfaces* (Wiley, New York, 2005).
- [72] S. Haq, private communication, 2005.
- [73] K. W. Kolasinsky, *Surface Science: foundation of catalysis and nanoscience* (Wiley, New York, 2002).
- [74] *International Tables for Crystallography*, edited by J. S. Kasper and K. Lonsdale (Kynoch Press, Birmingham, 1959).
- [75] S. M. Barlow and R. Raval, Surf. Sci. Rep. **50**, 201 (2003).
- [76] H. Hellmann, *Einführung in die Quantenchemie* (Deuticke, Leipzig, 1937).
- [77] R. P. Feynman, Phys. Rev. **56**, 340 (1939).
- [78] W. Kohn and L. J. Sham, Phys. Rev. **A 140**, 1133 (1965).
- [79] P. Hohenberg and W. Kohn, Phys. Rev. **B 136**, 864 (1964).

- [80] R. M. Dreizler and E. K. U. Gross, *Density functional theory* (Springer, Berlin, 1990).
- [81] B. Kasemo, *Surf. Sci.* **500**, 656 (2002).
- [82] F. Stadler, Ph.D. thesis, Universität Konstanz, 2004.
- [83] S. Rauschenbach *et al.*, submitted (unpublished).
- [84] G. R. Desiraju, *Acc. Chem. Res.* **29**, 441 (1996).
- [85] T. Steiner, *Angew. Chem. Int. Ed.* **41**, 48 (2002).
- [86] E. Breitmaier and G. Jung, *Organische Chemie* (Thieme, Stuttgart, 1994), Vol. 1.
- [87] R. S. Cahn, C. K. Ingold, and V. Prelog, *Angew. Chem. Int. Ed.* **5**, 385 (1996).
- [88] E. Fischer, *Ber. Dtsch. Chem. Ges.* **24**, 2683 (1891).
- [89] L. Bürgi, Ph.D. thesis, EPF Lausanne, 1999.
- [90] M. Stachel, The Advanced Physics Online Lab, <http://www.lockin.de>, 2004.
- [91] O. Gürlü, Ph.D. thesis, University of Twente, 2004.
- [92] M. A. Schneider, private communication, 2005.
- [93] AMENTEK Advanced Measurement Technology Inc., Model 5210, Dual Phase Lock-In Amplifier, Instruction Manual, 2002.
- [94] Omicron Nanotechnology GmbH, The VT Beam Deflection AFM User's Guide and Service Manual, 2001.
- [95] Goodfellow-GmbH, Katalog Metalle und Materialien, 2002.
- [96] G. R. Desiraju, *Angew. Chem. Int. Ed.* **34**, 2311 (1995).
- [97] S. S.-Y. Chui *et al.*, *Science* **283**, 1148 (1999).
- [98] B. J. Holliday and C. A. Mirkin, *Angew. Chem. Int. Ed.* **40**, 2022 (2001).
- [99] H. K. Chae *et al.*, *Nature* **427**, 523 (2004).

- [100] H. Srikanth, R. Hajndl, B. Moulton, and M. J. Zaworotko, *J. Appl. Phys.* **93**, 7089 (2003).
- [101] D. Maspoch *et al.*, *Nat. Mater.* **2**, 190 (2003).
- [102] A. Semenov *et al.*, *Angew. Chem. Int. Ed.* **38**, 2547 (1999).
- [103] U. Ziener, J.-M. Lehn, A. Mourran, and M. Möller, *Chem. Eur. J.* **8**, 951 (2002).
- [104] I. Weissbuch *et al.*, *Chem. Eur. J.* **6**, 725 (2000).
- [105] A. Dmitriev *et al.*, *J. Phys. Chem. B* **106**, 6907 (2002).
- [106] N. Lin *et al.*, *Angew. Chem. Int. Ed.* **41**, 4779 (2002).
- [107] P. Messina *et al.*, *J. Am. Chem. Soc.* **124**, 14000 (2002).
- [108] A. Dmitriev *et al.*, *Angew. Chem. Int. Ed.* **42**, 2670 (2003).
- [109] H. Spillmann *et al.*, *J. Am. Chem. Soc.* **125**, 10725 (2003).
- [110] M. A. Lingenfelder *et al.*, *Chem. Eur. J* **10**, 1913 (2004).
- [111] S. Stepanow *et al.*, *Nat. Mater.* **3**, 229 (2004).
- [112] A. Dmitriev *et al.*, *Langmuir* **20**, 4799 (2004).
- [113] D. G. Kurth, N. Severin, and J. P. Rabe, *Angew. Chem. Int. Ed.* **41**, 3681 (2002).
- [114] S. D. Feyter *et al.*, *Chem. Eur. J.* **10**, 1124 (2004).
- [115] S. Stepanow *et al.*, *NanoLetters* **5**, 901 (2005).
- [116] N. Lin *et al.*, *Chem. Comm.* **2005**, 1681 (2005).
- [117] F. Vidal *et al.*, *J. Am. Chem. Soc.* **127**, 10101 (2005).
- [118] B. G. Frederick, M. R. Ashton, and N. V. Richardson, *Surf. Sci* **292**, 33 (1993).
- [119] C. C. Perry, S. Haq, B. G. Frederick, and N. V. Richardson, *Surf. Sci* **409**, 512 (1998).
- [120] Q. Chen *et al.*, *Surf. Sci.* **446**, 63 (2000).
- [121] D. S. Martin, R. J. Cole, and S. Haq, *Surf. Sci* **539**, 171 (2003).

- [122] D. S. Martin, R. J. Cole, and S. Haq, Phys. Rev. B **66**, 155427 (2002).
- [123] S. Stepanow *et al.*, J. Phys. Chem. B **108**, 19392 (2004).
- [124] N. Lin *et al.*, Angew. Chem. Int. Ed. **44**, 1488 (2005).
- [125] F. Montalenti and R. Ferrando, Phys. Rev. B **59**, 5881 (1999).
- [126] B. Croset *et al.*, Phys. Rev. Lett. **88**, 056103 (2002).
- [127] H. Niehus, Appl. Phys. A **53**, 388 (1991).
- [128] D. Duchamp and R. E. Marsh, Acta. Cryst. B **25**, 5 (1969).
- [129] D. Cheng, M. A. Khan, and R. P. Houser, Inorg. Chem. **40**, 6858 (2001).
- [130] S. Griessl *et al.*, Single Mol. **3**, 25 (2002).
- [131] G.-J. Su *et al.*, J. Phys. Chem. B **108**, 1931 (2004).
- [132] Y. Ishikawa *et al.*, Chem. Commun. **22**, 2652 (2002).
- [133] G. Sheerin and A. A. Cafolla, Surf. Sci. **577**, 211 (2005).
- [134] Q.-L. Wang *et al.*, Z. Anorg. Allg. Chem. **630**, 613 (2004).
- [135] S. Konar *et al.*, Inorganica Chimica Acta **358**, 29 (2005).
- [136] F. Gonz  les-S  nchez, Spectrochimica Acta **12**, 17 (1958).
- [137] B. Han, Z. Li, S. Pronkin, and T. Wandlowski, Can. J. Chem. **82**, 1481 (2004).
- [138] J. A. Blackman and P. A. Mulheran, Phys. Rev. B **54**, 11681 (1996).
- [139] J. G. Amar, M. N. Popescu, and F. Family, Surf. Sci. **491**, 239 (2001).
- [140] J. G. Amar, M. N. Popescu, and F. Family, private communication, 2005.
- [141] J. G. Amar and F. Family, Phys. Rev. Lett. **74**, 2066 (1995).
- [142] K. Morgenstern, E. L  gsgaard, I. Stensgaard, and F. Besenbacher, Phys. Rev. Lett. **83**, 1613 (1999).
- [143] W. Ostwald, Z. Phys. Chem. **34**, 495 (1900).

- [144] S. Fölsch, P. Hyldgaard, R. Koch, and K. H. Ploog, Phys. Rev. Lett. **92**, 056803 (2004).
- [145] D. J. Coulman, J. Wintterlin, R. J. Behm, and G. Ertl, Phys. Rev. Lett. **64**, 1761 (1990).
- [146] <http://webbook.nist.gov/cgi/cbook.cgi?Name=trimesic+acid&Units=SI>.
- [147] A. Doyle *et al.*, Polyhedron **19**, 2621 (2000).
- [148] J. Perdew, K. Burke, and M. Ernzerhof, Phys. Rev. Lett. **77**, 3865 (1996).
- [149] D. Vanderbilt, Phys. Rev. B **41**, 7892 (1990).
- [150] S. Baroni, A. D. Corso, S. de Gironcoli, and P. Giannozzi, <http://www.pwscf.org>.
- [151] J. Tersoff and D. R. Hamann, Phys. Rev. Lett. **50**, 1998 (1983).
- [152] M. Vogelgesang *et al.* (unpublished).
- [153] S. Schintke and W. D. Schneider, J. Phys. Cond. Mat. **16**, R49 (2004).
- [154] T. Asada *et al.*, J. Phys. Cond. Mat. **11**, 9347 (1999).
- [155] H. J. Lee, W. Ho, and M. Persson, Phys. Rev. Lett. **92**, 186802 (2004).
- [156] T. Classen *et al.* (unpublished).
- [157] N. Berman, C. H. Ruof, and H. C. Howard, Anal. Chem. **23**, 1882 (1951).
- [158] J. R. Hahn and W. Ho, Phys. Rev. Lett. **87**, 196102 (2001).
- [159] L. Bartels, G. Meyer, and K.-H. Rieder, Surf. Sci. Lett. **432**, L621 (1999).
- [160] L. Bartels, G. Meyer, and K.-H. Rieder, Appl. Phys. Lett. **71**, 213 (1997).
- [161] B. J. McIntyre *et al.*, J. Vac. Sci. Tech. B **12**, 1994 (1993).
- [162] J. Pasán *et al.*, Polyhedron **22**, 2143 (2003).
- [163] B. Moulton *et al.*, Angew. Chem. Int. Ed. **114**, 2945 (2002).
- [164] H. Srikantha, R. Hajndl, B. Moulton, and M. J. Zaworotko, J. Appl. Phys. **93**, 7089 (2003).

- [165] S. Stepanow *et al.* (unpublished).
- [166] A. Dallmeyer *et al.*, Phys. Rev. B **61**, 5133 (2000).
- [167] C. Pfitsch, R. David, L. K. Verheij, and R. Franchy, Surf Sci. **468**, 137 (2000).
- [168] T. Classen *et al.*, Angew. Chem. Int. Ed. **44**, 6142 (2005).
- [169] A. B. Klautau and S. Frota-Pessôa, Phys. Rev. B **70**, 193407 (2004).
- [170] P. Gambardella *et al.*, Science **300**, 1130 (2003).
- [171] J. Lindner and K. Baberschke, J. Phys. Condens. Mat. **15**, S465 (2003).
- [172] V. S. Stepanyuk, A. N. Baranov, W. Hergert, and P. Bruno, Phys. Rev. B **68**, 205422 (2003).
- [173] R. A. Sheldon, *Chirotechnology* (Marcel Dekker, New York, 1993).
- [174] A. Baiker and H. U. Blaser, in *Enantioselective Catalysts and Reactions* (VCH, Weinheim, 1997), Vol. 5, p. 2422.
- [175] M. O. Lorenzo, C. J. Baddeley, C. Muryn, and R. Raval, Nature **404**, 376 (2000).
- [176] R. Fasel *et al.*, Angew. Chem. Int. Ed. **43**, 2853 (2004).
- [177] R. Raval, J. Phys. Cond. Mat **14**, 4119 (2002).
- [178] B. Behzadi, S. Romer, R. Fasel, and K.-H. Ernst, J. Am. Chem. Soc. **126**, 9176 (2004).
- [179] V. Humblot, S. M. Barlow, and R. Raval, Progr. Surf. Sci. **76**, 1 (2004).
- [180] I. Stensgaard, Surf. Sci. Lett. **545**, L747 (2003).
- [181] S. M. Barlow, S. Haq, and R. Raval, Langmuir **17**, 3292 (2001).
- [182] M. Lingenfelder *et al.*, submitted (unpublished).
- [183] M. Lingenfelder *et al.* (unpublished).
- [184] G. Ertl, Surf. Sci. **6**, 208 (1967).

- [185] P. Zeppenfeld, *Nanostrukturen auf Oberflächen: Formen, Muster und Stabilität* (Habilitation, Universität Bonn, 1994).
- [186] P. Stone *et al.*, Surf. Sci. **418**, 71 (1998).
- [187] N. Hartmann and R. J. Madix, Surf. Sci. **488**, 107 (2001).
- [188] X. C. Guo and R. J. Madix, Acc. Chem. Res. **36**, 471 (2003).
- [189] W. W. Pai, N. C. Bartelt, M. R. Peng, and J. E. Reutt-Robey, Surf. Sci. Letters **330**, L679 (1995).
- [190] F. Besenbacher and J. K. Nørskov, Progr. in. Surf. Sci. **44**, 5 (1993).
- [191] Y. Matsumoto and K. Tanaka, Surf. Sci. Lett. **350**, L227 (1996).
- [192] Y. Matsumoto and K. Tanaka, J. Vac. Sci. Technol. B **14**, 1114 (1996).
- [193] P. Zeppenfeld *et al.*, Phys. Rev. Lett. **72**, 2737 (1994).
- [194] G. Prévot *et al.*, Surf. Sci. **549**, 52 (2004).
- [195] V. I. Marchenko, Sov. Phys. JETP **54**, 605 (1982).
- [196] D. Vanderbilt, Surf. Sci. Lett. **268**, L300 (1992).
- [197] H. J. W. Zandvliet, private communication, 2002.
- [198] T. Zambelli, J. Wintterlin, J. Trost, and G. Ertl, Science **273**, 1688 (1996).
- [199] Z.-P. Liu and P. Hu, J. Am. Chem. Soc. **125**, 1958 (2003).
- [200] J. K. Nørskov *et al.*, J. Catal. **209**, 275 (2002).
- [201] R. T. Vang *et al.*, Nature Materials **4**, 160 (2005).

Publications

- T. Classen, G. Fratesi, G. Costantini, S. Fabris, F. L. Stadler, C. Kim, S. de Gironcoli, S. Baroni and K. Kern, “*Templated Growth of Metal-Organic Coordination Chains at Surfaces*”, Angew. Chem. Int. Ed. **44**, 6142 (2005).
- T. Classen, S. Stepanow, M. Lingenfelder, G. Costantini, N. Lin and K. Kern, “*Chiral Chains of Phe-Phe on Cu(110) and Cu(100)*”, in preparation.
- T. Classen, G. Fratesi, G. Costantini, S. Fabris, S. Haq, M. Lingenfelder, S. de Gironcoli, S. Baroni and K. Kern, “*Trimesic Acid on Cu(110): a combined STM, IR and DFT approach*”, in preparation.
- T. Classen, G. Costantini, M. Lingenfelder, Y. Wang and K. Kern, “*Bestowing Chirality to Metal-Organic Coordination Networks on Surfaces*”, in preparation.

Acknowledgements

I would like to thank the following people without whom this work would not have been possible:

- Prof. Klaus Kern for the opportunity to work on this exciting project and to be a member in his research group as well as for the friendly guidance throughout all the time.
- Prof. G. Meylan as president of the jury and Prof. K. Morgenstern, Prof. D. Pavuna, and Dr. R. Fasel for judging this thesis.
- Giovanni Costantini for being my direct supervisor for this thesis, for always being available for help and discussion, for many ideas, for a good working atmosphere, and a far-sighted organization.
- Cheolkyu Kim for introducing me to the world of UHV and STM and for persistent help and good teaching.
- Guido Fratesi, Stefano Fabris, Prof. S. de Gironcoli, and Prof. S. Baroni for the analysis using DFT calculations, for excellent and always fast communication including long telephone conferences and many fruitful discussions.
- Sam Haq and Prof. Rasmita Raval for the possibility to measure the TMA system with IR, LEED and TPD and for the very professional and friendly help on all related aspects.
- Prof. C. Elsässer for introducing me to the field of density functional theory and creating an enduring enthusiasm for this method.
- Michail Popescu for extensive discussions about chains, chain lengths, chain length distributions and chain length distribution differences.

- Oguzhan Gürlü, Peter Wahl, Lucia Vitali and Alexander Schneider for help with the spectroscopy and all related aspects.
- Wolfgang Stiepany, Wolfgang Heinz, Peter Andler, Andreas Koch, Mr. Siemers, Mr. Chaikovitch, and Mr. Plenert for fast and reliable technical support.
- Hannes Spillmann and Nian Lin for a lot of information on dipeptides and MOCNs and for interesting discussions.
- Frank Stadler for help wherever it was possible and for good company.
- Maggie Lingenfelder for a good working atmosphere and for being a reliable source for chemistry information.
- Sebastian Stepanow for the collaboration using the Phe-Phe on Cu(100) and for many nice discussions.
- Yeliang Wang for his enthusiasm in continuing the work.
- Georgios Katsaros, Stephan Rauschenbach and Thomas Weitz for a their humor and fresh spirit, for unconventional ideas, and for a great time in 4B8.
- Paola Acosta-Diaz, Michael Vogelgesang, Dominik Hoffmann, Gero Wittich, Nicola Malinowski, Carlos Manzano, Kannan Balasubramanian, Eugenio Lunedei, and Diego Repetto for being reliable friends and colleagues.
- Florian Kolb, Heiko Pittner, David Grellscheid, Martin Strauss, and all the other friends and colleagues from the years of study.
- My parents for all the support throughout the time, and just simply for everything.
- Mirjam Beuttler for encouraging, enduring, helping, and for always being there.

Curriculum vitae

Personal

Name:	Thomas R. Classen
Date of Birth:	January 6, 1976
Nationality:	German

Education

1986–1995	Middle and High School at the Leibniz-Gymnasium Stuttgart, Germany
1995–2001	Diploma studies in Physics at the University of Stuttgart, Germany
1998–1999	Graduate studies and Master of Science, Georgia Institute of Technology, Atlanta, GA, USA
2000–2001	Diploma thesis in the group of Prof. C. Elsässer at the Max-Planck-Institute for Metal Research in Stuttgart, Germany (department “Gefüge und Grenzflächen”, Prof. Rühle): “Mikroskopische Struktur und Energetik von kohärenten Übergangsmetall-SrTiO ₃ -Grenzflächen”
2002–2005	Research assistant in the group of Prof. K. Kern in the department of Nanoscale Science at the Max-Planck-Institute for Solid State Research in Stuttgart, Germany
December 2005	PhD thesis: “Self-organized growth of ordered functional nanostructures on templates”

